Universidade do Minho

Diagnosis of Rheumatic Heart Disease Based on Echocardiography Videos

Malik Saad Sultan

Tese de Doutoramento apresentada à
Faculdade de Ciências da Universidade do Porto, Universidade do Aveiro e Universidade do Minho
Informática

2018

Diagnosis of Rheumatic Heart Disease Based on Echocardiography Videos

Malik Saad Sultan
Programa Doutoral em Informática das Universidades do Minho, Aveiro e Porto
Departamento de Ciência de Computadores
2018

Orientador
Miguel Tavares Coimbra
Assistant Professor, Department of Computer Science
Faculty of Sciences of the University of Porto, Portugal

Coorientador
Manuel João Ferreira, PhD
Neadvance - Machine Vision, S.A, Braga, Portugal

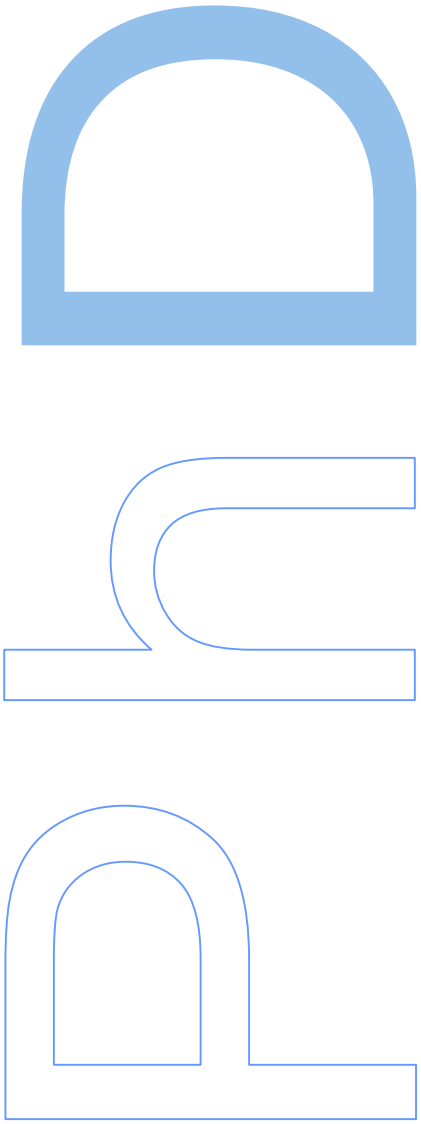

Declaration of Authorship

I, Malik Saad Sultan , declare that this PhD Thesis titled, 'Diagnosis of Rheumatic Heart Disease Based on Echocardiography Videos' and the work presented in it are my own. I confirm that:

- This work was done wholly or mainly while in candidature for a research degree at this University.
- Where any part of this thesis has previously been submitted for a degree or any other qualification at this University or any other institution, this has been clearly stated.
- Where I have consulted the published work of others, this is always clearly attributed.
- Where I have quoted from the work of others, the source is always given. With the exception of such quotations, this thesis is entirely my own work.
- I have acknowledged all main sources of help.
- Where the thesis is based on work done by myself jointly with others, I have made clear exactly what was done by others and what I have contributed myself.

Signed: Malik Saad Sultan

Date: July 03, 2018

Abstract

Rheumatic heart disease is the leading cause of heart valve damage, typically leading to heart failure, and is responsible for significant morbidity and mortality numbers in the developing world. Rheumatic heart disease is the serious consequences of repeated episodes of acute rheumatic fever and is initiated by the infection with the Group A streptococcus. Echocardiography screening can play a vital role to detect early manifestations of the rheumatic heart disease that are visible in the form of valve thickening, hockey shape leaflet, and mobility patterns. Early detection helps to define the disease burden and to control the disease progression.

To measure and quantify the early manifestations of rheumatic heart disease, the first step is to segment and track the mitral valve throughout the cardiac cycle. The segmentation and tracking in echocardiography videos are challenging due to low image quality, speckle noise, signal dropout, non-rigid and fast deformation. We have contributed to this problem by proposing several modifications in the highly adaptable classical snake model. The internal energy was modified by using the free boundary condition (open-ended contour), and the Harris cornerness measure and optical flow parameters were integrated in the external energy of the snake model. A near real-time approach was proposed that uses mathematical morphological operators to obtain the initial boundary, refined by the localized active contour. All these contributions require a manual initialization and fail in large frame to frame displacement and irregular motion of the anterior mitral leaflet.

To overcome the above limitations, a new image space was proposed, referred to as the virtual M-mode. A virtual M-mode space is obtained by sampling the echocardiography videos by an estimated scanning line over time. The virtual M-mode space proved to be more adequate to identify and track the anterior mitral leaflet. After identifying the anterior mitral leaflet, localized active contours were used to segment the whole region in each frame. The limitation of this work is the low robustness against the problem of under segmentation and over-segmentation. To overcome the problem of under-segmentation, an extended approach was proposed that uses multiple scanning lines to sample the whole image over time, aiming not only to identify the anterior mitral leaflet but the complete region segmentation in the virtual M-mode space. Finally, shape constraints were introduced in the snake model to avoid over-segmentation.

Acknowledgements

I, Malik Saad Sultan , would like to thank Prof. Miguel Coimbra and Dr. Manuel Ferreira as my main supporters on this work. Without your help this thesis would not have been made possible. Thank you for sharing your time, expertise, and skills. I am honored to be part of your research team. I am very thankful to Nelson Martins and Eva Costa for your critical reviews and support. To Luiz Pires and Diana Veiga for their help as friends and work partners. To Dr Sandra Mattos many thanks, their medical experience was very important.

At last but not the least, I would like to thank my family, specially my parents, Malik Mehmood Sultan and Yasmeen Bibi, for their patience, prayers and moral support throughout my PhD studies and my life in general. I would take this opportunity to appreciate my wife, Sidra Tul Islam, and thank her from the bottom of my heart for standing besides me to overcome every single situation, in particular, her incredible support for my PhD studies and specially during the final stage of my thesis writing.

I would like to thank and acknowledge the funders of my research: this thesis is a result of the project (NORTE-01-0247-FEDER-003507-RHDecho), co-funded by Norte Portugal Regional Operational Programme (NORTE 2020), under the PORTUGAL 2020 Partnership Agreement, through the European Regional Development Fund (ERDF). This work also had the collaboration of the Fundação para a Ciência a e Tecnologia (FCT) grant no: PD/BD/105761/2014 and has contributions from the project NanoSTIMA, NORTE-01-0145-FEDER-000016, supported by Norte Portugal Regional Operational Programme (NORTE 2020), through Portugal 2020 and the European Regional Development Fund (ERDF).

Contents

Declaration of Authorship i

Abstract ii

Acknowledgements iii

Contents iv

List of Figures vii

List of Tables x

Abbreviations xi

1 Introduction 1
- 1.1 Motivation . . . 1
- 1.2 Why do we need a CAD system for RHD? . . . 2
- 1.3 State of the Art in Mitral Valve Segmentation . . . 2
  - 1.3.1 AML Segmentation in 2D Echocardiography . . . 3
  - 1.3.2 AML Segmentation in 3D Echocardiography . . . 7
- 1.4 Objective . . . 15
- 1.5 Main Contributions . . . 15
- 1.6 Resulting Publication . . . 17
  - 1.6.1 Journal Publications . . . 17
  - 1.6.2 Book Chapter . . . 17
  - 1.6.3 Conference Publications . . . 18
  - 1.6.4 Other Contributions . . . 18
- 1.7 Thesis Structure . . . 19

2 Medical background 20
- 2.1 Anatomy and Function of the Heart . . . 20
- 2.2 Anatomy and Dynamics of the Mitral Valve . . . 22
- 2.3 Pathologies of the Heart Valve . . . 25
- 2.4 Rheumatic Heart Disease . . . 26
  - 2.4.1 Pathogenesis of Rheumatic Heart Disease . . . 26

2.4.2 Global Burden of Rheumatic Heart Disease . . . 27
2.4.3 Clinical Manifestations of Rheumatic Heart Disease . . . 28
2.4.4 Cost of Rheumatic Heart Disease . . . 29
2.4.5 Pattern of Valvular Involvement . . . 29
2.5 Role of Echocardiography Screening . . . 30
2.5.1 WHF Criteria for Echocardiographic Diagnosis of RHD . . . 30

3 Active Contours for Echocardiography Image Segmentation 33
3.1 Active Contours . . . 34
3.1.1 Snake Model – PAC . . . 34
3.1.2 Balloon Force Model – PAC . . . 36
3.1.3 Gradient Vector Flow Model – PAC . . . 38
3.1.4 Geometric Active Contour – Level sets . . . 40
3.1.5 Geodesic Active Contour – Level sets . . . 42
3.1.6 Chan-Vese Model – Level sets . . . 43
3.1.7 Localized Active Contour Model – Level sets . . . 46
3.2 Echocardiography Image Segmentation . . . 48

4 Tracking of the Anterior Mitral Leaflet using Active Contours in Echocardiography Videos 51
4.1 Incorporating Harris Energy in an Active Contour Framework . . . 52
4.1.1 Internal Energy . . . 53
4.1.2 External Energy . . . 53
4.1.3 Materials . . . 57
4.1.4 Experimental Methodology . . . 57
4.1.5 Tracking results . . . 58
4.1.6 Discussion . . . 59
4.2 Incorporating Optical Flow Energy in an Active Contour Framework . . . 59
4.2.1 Internal energy . . . 59
4.2.2 External Energy . . . 60
4.2.3 Materials . . . 63
4.2.4 Experimental Methodology . . . 63
4.2.5 Tracking Results . . . 64
4.2.6 Discussion . . . 65

5 Real-Time Anterior Mitral Leaflet Tracking using Morphological Operators and Active Contours 67
5.1 Thin Region Extractor . . . 68
5.2 Displaced Region . . . 69
5.3 Candidate Image . . . 70
5.4 Region Classification . . . 72
5.5 Refining Using Active Contours . . . 73
5.5.1 Automatic Initialization . . . 74
5.5.2 Localized Active Contours . . . 74
5.6 AML Analysis . . . 75
5.6.1 Skeletonization . . . 75
5.6.2 Motion Patterns . . . 76

5.6.3 Shape . . . 77
5.6.4 Extended Modified Hausdorff Distance . . . 79
5.7 Materials . . . 79
5.8 Experimental Methodology . . . 80
5.9 Tracking Results . . . 81
5.10 Discussion . . . 83

6 Virtual M-Mode Space for the Anterior Mitral Leaflet Segmentation in Echocardiography Videos 85
6.1 Virtual M-mode Space . . . 86
6.2 Identify the AML in Each Frame using the VM-mode . . . 90
6.2.1 Estimating Motion Patterns from the VM-Mode . . . 91
6.2.2 AML Segmentation . . . 94
6.2.3 Materials . . . 96
6.2.4 Experimental Methodology . . . 97
6.2.5 Segmentation Results . . . 98
6.2.6 Discussion . . . 101
6.3 Segment the Whole AML in Each Frame using the VM-mode . . . 102
6.3.1 VM-mode Space . . . 103
6.3.2 Junction Point Estimation . . . 105
6.3.3 AML Segmentation in the VM-mode Space . . . 106
6.3.4 Refining Using LAC . . . 107
6.3.5 Materials . . . 107
6.3.6 Experimental Methodology . . . 108
6.3.7 Segmentation Results . . . 108
6.3.8 Discussion . . . 109

7 Conclusion 110
7.1 Research Collaborations . . . 111

List of Figures

1.1 A) Contour points and thickness constraint d B) Optical flow (y-component) C) Optical flow after interpolation. . . . 4
1.2 Two active contours and junction point. . . . 5
1.3 Manually selected regions and matrix spectral analysis 7
1.4 A) Original image B) Mitral valve segmentation using region competition based active contour. . . . 9
1.5 2D slice from 3D TEE. A) automatic segmentation, B) after user modification. . . . 10
1.6 A) Search arc B) Atrial view of open valve C) Intensity image with trimming contour 11
1.7 User initialization step: A) Identify region of interest in long axis view B) Series of points on annulus in atrial view C) Series of point on the AML in atrial view. . . . 12
1.8 Medial geometry, R is the radius, $B+$ and $B-$ are the object boundaries, Red: medial surface m, Thickness measured as chord length. . . . 13
1.9 Pipeline of the mitral valve segmentation using multi-atlas framework . . 13
1.10 A) Select slice by navigating 3D volume with valve closed and insert 3 points B) 2 points selected from cut-plane orthogonal to that containing the A and P C) 4 points on four cut plane. . . . 14
1.11 Left: Medial axis of the mitral leaflet between a pair of annular points, Right: Estimated thickness. . . . 14

2.1 Human heart, showing four chambers, veins, arteries and valves 21
2.2 Cardiac events: systole and diastole, opening and closing pattern of Mitral, aortic valve Vs aortic, atrial and ventricular pressure 22
2.3 Mitral valve components. . . . 23
2.4 Anatomy of the mitral valve 24
2.5 Regurgitation and stenosis. . . . 25
2.6 Repeated episodes of ARF and the mitral valve damage. . . . 27
2.7 The global burden of RHD.: from 1990 to 2013. . . . 28
2.8 A) pattern of valve involvement B) Affected valves with pathologies. MR: mitral regurgitation, MS: mitral stenosis, AR: aortic regurgitation, AS: aortic stenosis, MV: mixed mitral valve diseases, AV: mixed aortic valve diseases. . . . 30
2.9 Clinical versus echocardiography based screening in school children at Africa. . . . 31

3.1 Snake model 37
3.2 Balloon force model 38

3.3 Gradient vector flow . . . 40
3.4 All possible condition of the curve . . . 44
3.5 Localized active contour model . . . 48

4.1 Parasternal long axis view of a normal mitral valve in diastole. . . . 52
4.2 Surf plots: DoG of AML region of grayscale image. Positive valued pixels (intensity map), negative valued pixels (edge map). . . . 54
4.3 Harris Cornerness measure (E_{Harris}), shows corners in Red and edges in Blue . . . 56
4.4 Lucas-Kanade optical flow with pyramids (Coarse-to-fine) . . . 61
4.5 Motion vectors of the optical flow (Lucas-Kanade). Last frame: Green, Present frame: Magenta . . . 62
4.6 Tracking of the AML. Red: Ground truth, Green: Ref. approach, Blue: Our approach, Green arrows: Motion vectors . . . 65

5.1 AML tracking pipeline . . . 68
5.2 A) Grayscale image B) Morphological opening C) Top-hat transform . . . 69
5.3 Parasternal long axis view (A): showing Mitral valve (MV), Anterior Mitral Leaflet (AML), Posterior Mitral Leaflet (PML) and other structures. (B): Shows the MV in Diastole/Systole phase, the thickened and hockey shape leaflet. . . . 70
5.4 Regions with high displacement at four different times (frames) . . . 71
5.5 Candidate image for final AML classification . . . 72
5.6 Classification scheme . . . 73
5.7 Synthetic image with heterogeneous intensity A) Initial contour. B) Region-based segmentation. (c) Edge-based segmentation. . . . 74
5.8 Segmented region of AML: A) Obtained skeleton B) Obtained skeleton after removing minor branches . . . 76
5.9 Motion patterns generated by AML . . . 77
5.10 Curvature approximation using Area and crossover angle θ_c . . . 78
5.11 Motion and curvature pattern of AML, red: motion pattern, green: curvature pattern . . . 79
5.12 Region classification . . . 80
5.13 Extended modified Hausdorff distance error, 67 cases. . . . 81
5.14 Number of failure in each video, 67 cases. . . . 82
5.15 Segmentation results, red: doctor's annotation, green: proposed method . 83

6.1 Initialization point (P_{Ref}) at the posterior wall of the aorta (PWA) with a default 90° angle and the scanning line intersecting with the anterior wall of the aorta (AWA) and the posterior wall of the left atrium (PWLA). 88
6.2 VM-mode obtained from 5 videos. X-axis shows the number of frames and Y-axis showing the distance from the transducer. Visible structures are the anterior wall of the aorta (AWA), posterior wall of the aorta (PWA) and posterior wall of the left atrium (PWLA) . . . 89
6.3 The pipeline of the method to segment AML in echocardiography videos. 90
6.4 Model details: Internal, external and total energy. Movement of points on the scanning line to segment pattern of the posterior wall of the aorta (PWA) in VM-mode. UL and LL are respectively, the upper and lower limits. . . . 92

6.5 Segmented motion patterns of the VM-mode in 5 videos. Green: Anterior wall of the aorta (AWA), Red: Posterior wall of the aorta (PWA), Blue: Posterior wall of the left atrium (PWLA). 95
6.6 Segmentation result, row 1: good segmentation, row 2: segmentation with outliers, row 3: segmentation with missing parts. 96
6.7 Evaluation of segmentation with MHD error (mm) obtained against the ground truth for our approach, Ref.1 and Ref.2 using 67 videos. 99
6.8 Failure after an average number of frames for our approach, Ref.1 and Ref.2 using 67 videos. 100
6.9 Segmentation result, A, B) Normal, C) Thickened D) Hockey shape leaflet. 101
6.10 Pipeline of the AML segmentation in echocardiographic videos. 102
6.11 A) Parasternal long axis (PLAX) view (AML - Anterior Mitral Leaflet, PWA - Posterior Wall of the Aorta, P_{Start}- starting point of the ultrasound); B) PLAX view of the ultrasound image, origin point P_{Start} with respective angles and scanning lines. 103
6.12 Row-1: Images in the VM-mode space obtained from the N scanning lines. Row-2: Segmented AML region in the VM-mode space. 104
6.13 A) Reconstructed image from the N number of images in the VM-mode space. Showing the left atrium (LA), the reference point (P_{REF}) and the junction point (P_{JNC}). B) Showing the left and right limits with their respective scanning lines. 106

List of Tables

1.1 Literature review (2D echocardiography). A = Automatic, SA = Semi-automatic 8

4.1 Tracking error (Pixel) 58
4.2 Tracking results (in pixels) 64

6.1 Comparison of Precision and Recall (67 videos) 100
6.2 Comparison matrix, (Median / STD) 108

Abbreviations

RHD	**R**heumatic **H**eart **D**isease
ARF	**A**cute **R**heumatic **F**ever
WHO	**W**orld **H**ealth **O**rganization
NIH	**N**ational **I**nstitutes of **H**ealth
PM	**P**apillary **M**uscles
TEE	**T**rans**e**sophageal **E**chocardiography
AML	**A**nterior **M**itral **L**eaflet
PML	**P**osterior **M**itral **L**eaflet
RMSE	**R**oot **M**ean **S**quare **E**rror
STD	**St**andard **D**eviation
GAC	**G**eometric **A**ctive **C**ontour
PAC	**P**arametric **A**ctive **C**ontour
CAD	**C**omputer **A**ided **D**iagnosis

This work is dedicated to my children, Malik Abdullah Sultan and Malik Mikaeel Sultan

Chapter 1

Introduction

1.1 Motivation

Rheumatic Heart Disease (RHD) is an inflammatory disease that results from repeated episodes of Acute Rheumatic Fever (ARF) [1, 2]. The disease begins in childhood at age 5 to 15 years and it slowly damages the heart valves, reducing valve efficiency and eventually leading to cardiac failure [3, 4]. RHD remains a leading cause of morbidity and mortality in the developing countries. Following the recent study [5], it was estimated that the RHD affects approximately 33.4 million people globally, with about 10.5 million cases in advance stage requiring surgery that is unavailable, expensive and highly risky, and is responsible for about 319,400 deaths per year. The average surgery cost is much higher (US$ 25,000) than primary prevention or secondary prophylaxis to reduce recurrence of ARF using penicillin (US$ 50 per person) [6].

The disease is apparently controlled in developed countries, due to the availability of health-care services, vaccines and improved hygiene conditions [7]. However in developing countries, the improvement in detection tools has utmost importance to early case identification, to control the disease progression and to minimize death rates due to RHD.

In RHD, the mitral valve damage is dominant with or without the involvement of the other heart valves [8]. The pathological conditions as a result of RHD are regurgitation, stenosis, and prolapse [9]. These conditions can be measured and quantified by discriminant morphological features such as thickness, shape, and mobility (restricted

/ excessive leaflet motion) [10]. Echocardiography screening has proved its sensitivity and specificity to detect early morphological changes and it is able to detect sub-clinical RHD cases (no murmur and ARF history) [11–15].

Further details are given in chapter 2, on Medical background.

1.2 Why do we need a CAD system for RHD?

Based on the fact that RHD doesn't occur after the very first attack of ARF. An early detection is considered vital to define the disease burden in fewest resource regions and to control the disease progression by assisting the health authorities to take appropriate measures. Our research line aims to design a Computer Aided Diagnosis (CAD) system that will assist cardiologists for the early detection of RHD cases from echocardiography videos. The cardiologists will consider the output of CAD system as a "second opinion" to make a final diagnostic decision. The CAD system will be able to provide the quantitative and objective evaluation of the mitral valve, based on the morphological features such as thickness, shape and mobility.

The CAD system is expected to be robust while diagnosis RHD. Robustness refers to the consistent performance of the CAD system over time and in different clinical situations. The pipeline of designing the CAD system can be divided into four main stages: preprocessing, segmentation, feature extraction and classification. This thesis work makes a contribution to the segmentation stage. It is the most important stage of the CAD systems that directly affect the decision and thus demanding a high sensitivity and specificity.

1.3 State of the Art in Mitral Valve Segmentation

Manual segmentation of the AML in each frame of the echocardiographic sequences is slow, tedious and requires expert knowledge and vary among different observers. However, robust, accurate and fully automatic segmentation and tracking of the AML in echocardiographic images is an open problem. The low signal to noise ratio, the presence of speckle noise and artifacts, lack of reliable features, probe orientation, fast and irregular motion are some of the challenges that need to be addressed. In the literature,

several researchers have attempted to address the segmentation and tracking problem in 2D, 3D, and 4D echocardiography. The active contour framework has been widely used for the segmentation of the AML in echocardiographic images. The tracking of the structures such as AML is achieved by using the segmentation result from the previous frame (at time t-1) as an initial boundary for the present frame (at time t).

1.3.1 AML Segmentation in 2D Echocardiography

Mikic et. al. [16] in 1998, proposed a semi-automatic AML segmentation and tracking method that uses the active contour framework with a multiscale version of Singh's algorithm (optical flow) [17], in 2D echocardiography. The optical flow was computed in successive frames (at time t-1 and t) providing a force to push the curve towards the expected position of the AML. The average velocity of the object was used as an initial velocity of the curve. The objective of adding the optical flow was to handle the large motion of the AML in consecutive frames. Finally, the contour at a new position (estimated by the optical flow) was evolved under the image force to get the true boundaries. The author had discussed the limitation of using optical flow for the tracking of the AML. The optical flow fails in situations when the mitral valve first opens and when the leaflet shows large displacement in successive frames. In ultrasound images, the tip of the mitral leaflets look merged in the closed valve due to the availability of only the intensity feature and starts moving in the opposite direction when the valve opens. In this situation, optical flow fails to compute the correct velocity of the tip of the mitral leaflets (see Figure 1.1B). Since the problem happens only at the tip region, the author interpolated the values based on other points (see Figure 1.1C). The elastic energy was used to preserve the length of the contour in the active contour framework. However, it results in failure of the active contour in situations when the AML shows a sudden change in length. To overcome this, the author proposed integration of the shape constraint in the active contour framework. The author used the AML thickness as the shape feature, since it appears to be preserved throughout the cardiac cycle (see Figure 1.1A). The thickness computed from the manual annotation (1^{st} frame of the sequence) was considered as optimal. The thickness constraint provides an external force to prevent the opposite sides of the contour to collapse. It happens due to the large AML displacement in successive frames, creating a situation in which opposite side of the contour attracts towards the same side of the AML. The proposed method

was evaluated against the manual annotation obtained by expert physicians, on eight 2D echocardiographic sequences. The mean absolute distance was measured between the automatic segmentation and the ground truth. The proposed method has successfully segmented the AML in all eight sequences. To summarize the limitations of his method, it requires manual initialization close to the object boundary in the first frame, failed to handle large frame to frame displacement (larger than the leaflet thickness) due to the unreliability of the optical flow and was computationally expensive (20 min/sequence).

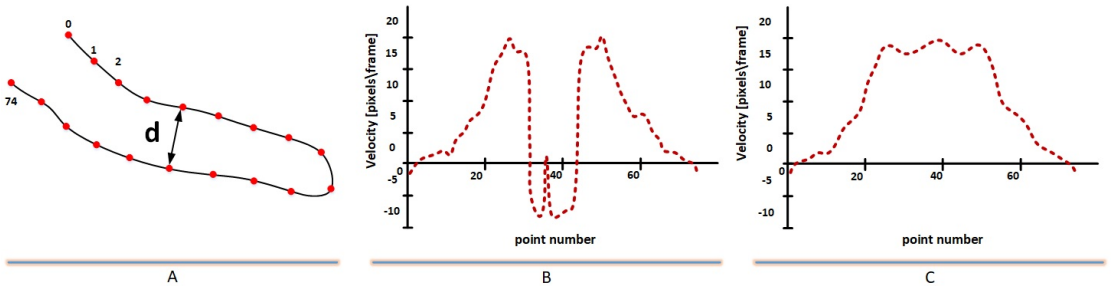

FIGURE 1.1: A) Contour points and thickness constraint d B) Optical flow (y-component) C) Optical flow after interpolation (adapted from [16])

Martin et. al [18, 19] in 2006, proposed a semi-automatic AML segmentation method that uses a curve fitting algorithm (transformation fitting) to get the rough boundary refined by the two connected active contours, in 2D echocardiography. The objective of his work was to achieve real-time performance of the algorithm. The proposed method can be realized in two steps: the rough estimation, and the refining by active contours. Both steps were based on his observation of the difference of motion of the muscle and the AML (see Figure 1.2). The muscle shows the rigid motion and thus the rigid transformation was estimated for the muscle curve. Whereas, the motion of the AML was close to non-rigid rotational motion around the junction point (muscle-leaflet), and thus based on that the curve was transformed around the new estimated junction point. Again, based on the assumption that the motion of muscle and AML are different, two connected active contours were used to improve the tracking capabilities. For the external energy of the active contour, the author proposed using the highest principal curvature of the image. The Hessian matrix [20] of the intensity map of the image was computed to obtain the principal curvature map. The intensity profile of the AML shows the local maximum in the direction of the largest curvature. Next, the author used the Canny edge detector to obtain the edge map. Following the fact that the motion of the muscle is not large, the author defined search area of 8x8 around each contour point. The dynamic programming [21] to minimize the total energy of the active contour

framework. The feature points (edges) were searched normal to the muscle and AML curve. The proposed method for the segmentation of the muscle and AML was tested on three sequences and was visually assessed by an expert. The method has performed well in the tracking of the AML and was successful in separating the muscle tissues from the AML. The limitations of the algorithm are: it requires manual segmentation for the muscle and the AML, a single point junction initialization, parameter tuning, the principal curvature is sensitive to noise, failed in a large frame to frame displacement.

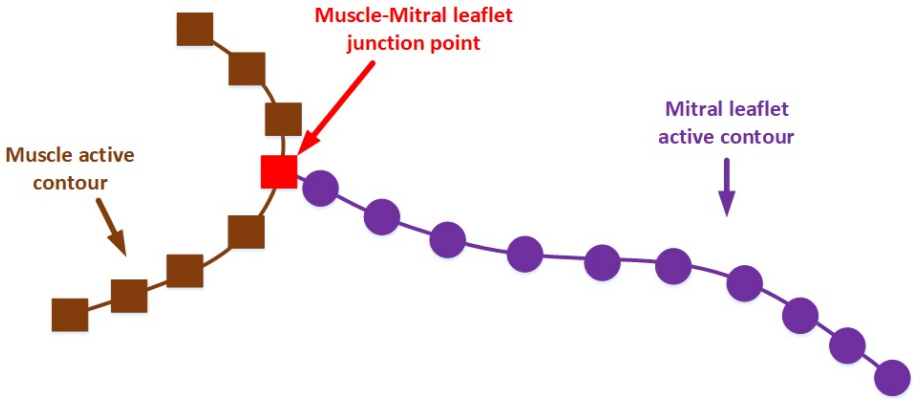

FIGURE 1.2: Two active contours and junction point (adapted from [18, 19])

Sheng et. al. [22] in 2006, proposed a segmentation method that uses a shape based active contour model integrated with the generalized Hough transform [23], in 2D echocardiography. The framework was designed based on the assumption that the shape and location of the structures doesn't change a lot in successive frames. In other words, the boundary of structures in successive frames are correlated to some degree. Therefore, segmentation results obtained in the previous frame (at time t-1) can be used as a shape template in the present frame (at time t). To incorporate this information in the active contour model [24], the author added the constraint energy computed from the template matching. The author basically measures the degree of similarity between the shape templates obtained from the segmentation results of the previous frame and the active contour. Based on the template matching concept, the author proposed the constraint energy that consists of two terms. The first term was the curvature dependent shape descriptor. The selection of curvature was based on the fact that it is invariant to rotation and translation. Whereas, the second term was the smoothness term. The external energy was based on the texture information of the image, instead of the image gradient (edges) because the edges are sensitive to the speckle noise. The generalized Hough transform was used to estimate the rough estimation of the initial boundary at

time t, and was computed by transforming the segmentation results of the previous frame (at time t-1) as a shape prior. The roughly estimated initial boundary was refined by his modified active contour model. The algorithm was tested on 22 echocardiographic videos of the mitral valve. To evaluate the method, the mean absolute distance was computed between the automatic segmentation and the ground truth obtained from the expert annotation. This model has successfully handled the complex motion of structures, like the AML and approved the principle idea of the model. However, the model has some limitations such as: it was difficult to obtain the optimal parameters that are robust for each video (parameter adjustment), requires manual segmentation in the first frame (shape prior), fails in large frame to frame displacement and was computationally expensive due to the generalized Hough transform (6min /sequence).

Zhou et. al. in 2012 [25] and Liu et. al. in 2014 [26], proposed a fully automatic approach for the tracking of the AML as an outlier using low-rank matrix, in 2D and 3D echocardiography. The motion of the AML and other structures like the cardiac walls in a low-rank matrix was analyzed (see Figure 1.3). The author's found that the fast moving structure with large deformation was not visible in a low-rank matrix. Based on this observation, a framework that considers a problem of segmentation and tracking simply as contiguous outlier detection in a low-rank matrix using the set of eigenvalues of the matrix, a process called as matrix spectral analysis. The author's found that more bases (eigenvalues) are needed to present the AML compared to cardiac walls. In other words, more principal components are required to describe the intensity changes of the fast moving and deformable structure of the AML. This was the key concept used in their work. The low-rank matrix was iteratively computed using the SOFT-IMPUTE algorithm [27]. To remove the unwanted region from the segmentation results (binary mask) due to the fast motion of other tissues like the papillary muscles. Zhou et. al. [25] used the morphological operators to extract the largest region from segmentation results, whereas, Liu et. al. [26] used region based active contours to refine the shape of the detected AML. To avoid segmenting the unwanted regions, the author's proposed a region scalable mask to efficiently compute the interior and exterior energy for the region based active contour framework. To evaluate the proposed methods. Zhou et. al. [25] computed the mean absolute distance between the automatic segmentation and the ground truth (manual annotation), whereas, Liu et. al. [26] not only computed the mean absolute distance but also provided the comparison study with the Zhou et.

al. [25] method. Liu et. al. [26] results outperform the results of Zhou et. al. [25]. Both methods worked reasonably well. However, they had some limitations such as the rank was very sensitive to noise and thus requires a parameter tuning to get the optimal results. Zhou et. al.'s [25] method required the cropping of unwanted regions whereas, Liu et. al.'s [26] method was sensitive to region scalable mask. The Table 1.1 summarizes the literature on AML segmentation in 2D echocardiography.

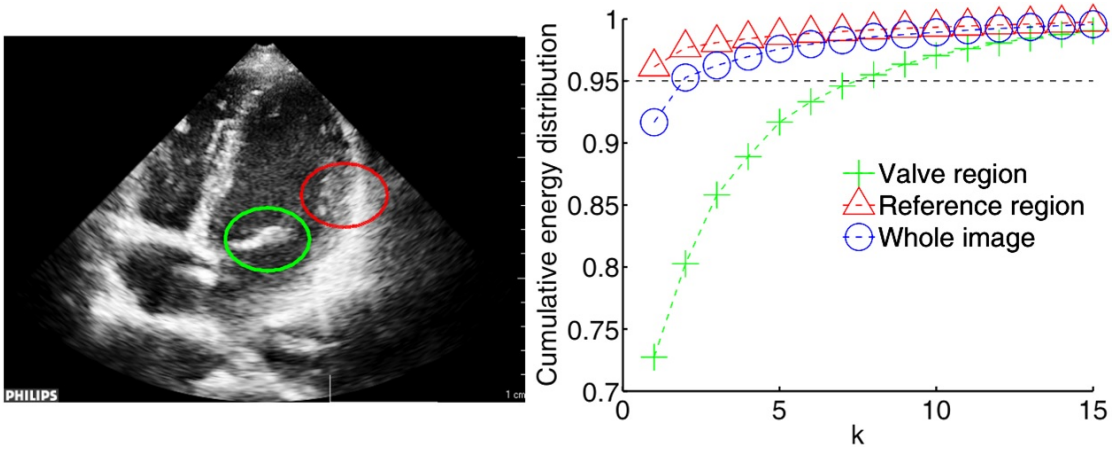

FIGURE 1.3: Manually selected regions and matrix spectral analysis (adapted from [25, 26])

1.3.2 AML Segmentation in 3D Echocardiography

The work discussed earlier, mainly focuses on the segmentation and tracking of structure in 2D echocardiography. It provides the 2D cut of the 3D structure and their motion on a single plane. Besides the fact that the shape and motion of the structures are better visible in 3D echocardiography, the 2D echocardiography still stands out, as the standard in most countries. The focus of this thesis is the segmentation and tracking of the AML in 2D echocardiography. However, to get the broader understanding of the problem in hand, we provide a quick overview of the literature that focuses on patient-specific heart modeling by segmenting structures in 3D space.

Shang et. al. [28] in 2008, proposed a region competition based active contour model for the segmentation of structures, in 3D CTA, MRA and echocardiography. The basic concept was originally proposed by Zhu et. al. [29] that uses the generalized Bayes and minimum description length in the classical active contour framework. His model was incapable of changing the topology of the curve. Following this limitation, a region based on probabilistic energy in a level set framework was proposed to segment the 3D

TABLE 1.1: Literature review (2D echocardiography). A = Automatic, SA = Semi-automatic

Methods	**A / SA**	**Methodology**	**Limitations**
I. Mikic [16], 1988	SA	• Active contours and Optical flow • Two step method • Used thickness as shape feature (External energy)	• Optical flow failure at leaflet tip • Elastic energy failure in sudden length change • Failure in large frame to frame leaflet displacement, greater than leaflet thickness • Requires manual initialization • Computationally expensive
S. Martin [18, 19], 2006	SA	• Transform fitting and two connected active contours • Two step method • Used principal curvature map (External energy)	• Requires manual initialization (Muscle, AML, Junction) • Parameter tuning • Sensitivity of principal curvature to noise • Failure in large frame to frame leaflet displacement
C. Sheng [22], 2006	SA	• Shape based active contour and Generalized Hough transform • Two step method • Used texture information of image instead of image gradient	• Parameter tuning • Requires manual initialization • Failure in large frame to frame leaflet displacement • Computationally expensive due to Hough transform
X. Zhou [25], 2012 **X. Liu [26], 2014**	A	• Low-rank matrix and Active contour / Morphological operators	• Sensitive to rank • Parameter tuning • Requires to crop the region of interest • Sensitive region scalable mask

structures in medical images and was capable of naturally dealing with the topology changes (see Figure 1.4). A speed controlling term was integrated in the model to achieve better convergence speed at both strong and weak edges (object boundaries). In the original region competition based snake model, a large number of contours were initialized that evolve and compete with neighbor regions and start merging when the regions are homogeneous. In a similar way, the level set function naturally deals with the splitting and merging depending on the prior known distribution of the background and the object. The prior known probabilistic distribution helps in the robust segmentation of the objects. To evaluate the method, the author compared the segmentation results with geodesic active contour [30] and region-based active contour [31].

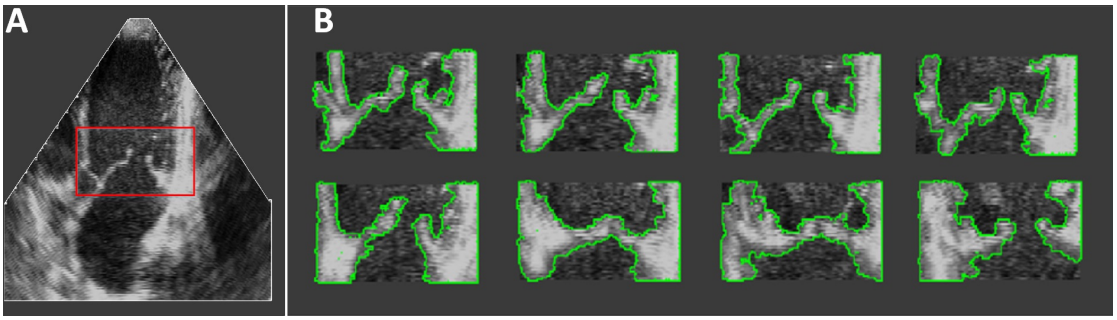

FIGURE 1.4: A) Original image B) Mitral valve segmentation using region competition based active contour (adapted from [28])

Burlina et. al. [32, 33] in 2010 and 2013, proposed a patient specific modeling, analysis and closure predication of the mitral valve, in 3D echocardiography. The objective of his work was to recover the structure and to analyze the competency of the mitral valve after a surgery. The segmentation module in his work serves to recover the 3D structures of the mitral valve from 3D echocardiography, later used for mechanical modeling. For the mitral leaflet detection, he implemented two methods. The first was a thin tissue detector model [34] that extracts thin regions based on the disparities of the eigenvalues, computed by the Hessian matrix of a Gaussian smoothed intensity image. The second used of basic mathematical morphological operators to extract the thin tissues. The author used geometric active contours [30] in the level set framework to segment the intraventricular cavities and inner heart wall boundaries of the atrial. The author's combined the thin tissue detector method and level set method to achieve better segmentation performance (see Figure 1.5). Next, an expert verifies if the segmentation was accurate. If not, then the user can interact manually to refine the particular part of the segmented region. The 3D mesh was created using the segmentation results of the mitral valve in an open state. The 3D mesh was later used as the initial configuration to predict the configuration of the valve in the closed position.

Schneider et. al. [35] in 2011, proposed a patient specific modeling of the mitral valve leaflet, in 3D echocardiography. The segmentation of the mitral valve leaflet in 3D echocardiography provides the geometry of the valve and was used to automatically initialize the mechanical models to predict the closure state of the valve. The segmentation method requires the location of the mitral annulus as an input, which was computed by previously developed semi-automatic segmentation method (single point initialization) [36]. To segment the mitral annulus, a thin tissue detector, and a max-flow algorithm were used to draw a surface near the user specified point. The location of the annulus

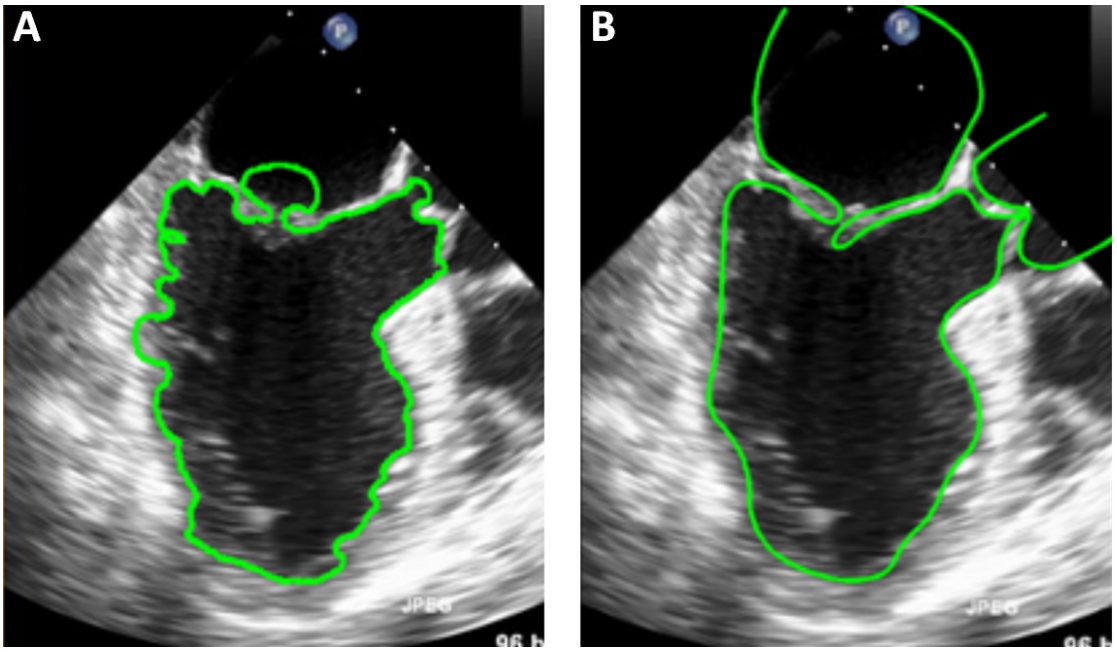

FIGURE 1.5: 2D slice from 3D TEE. A) automatic segmentation, B) after user modification (adapted from [32])

was then obtained by searching for the point where the thin mitral leaflet connects with the thicker heart wall region. The mitral leaflet segmentation method comprises of five steps, defining the search space, refining the search space, estimating the leaflet surface, refining the leaflet surface, and trimming the extended leaflet surface. This was based on the fact that the mitral leaflets show rotational motion around the mitral annulus and are connected. A search space was defined using the arch system centered at the mitral annulus and was based on the assumption that the mitral leaflet will intersect the arch at least at a single point (see Figure 1.6A,B). The orientation of the mitral leaflet (axis) was initially defined by the least variance of the estimated annulus computed by principal component analysis. The mitral leaflet location was finally computed using the graph-cut method and later used to redefine the axis that passes exactly from the center of the mitral leaflets. The extended leaflet surface was computed by redefining the graph (product of the original image and thin tissue) and the weights, by using the min-cut graph method (see Figure 1.6C). A small part of the blood pool region usually merged in the segmented mitral leaflet that needs to be filtered out. To do this, first they reduced the intensity of the image and then used the level set based region competition active contours [28] to separate the leaflet from the blood pool. The mesh was generated using the segmentation results, showing the patient specific geometry of the mitral leaflet. The mesh was the fundamental building block and was used as an

input for the mechanical modeling. In another work [37], the authors proposed a mitral valve segmentation during valve closure, in 4D (3D + T) echocardiography. The method requires the user to manually select two frames, one before the valve begins to close and other when it closed, from the 4D echocardiographic video. The user also needs to insert a single point near the center of the mitral leaflet (in a closed valve). These initialization help to segment the mitral annulus and then are tracked using Lucas Kanade optical flow [38]. The mitral leaflet was finally segmented using the segmented annulus by his previously proposed algorithm [37]. The mesh was created by using the obtained mitral valve segmentation and evolved frame by frame as an active surface.

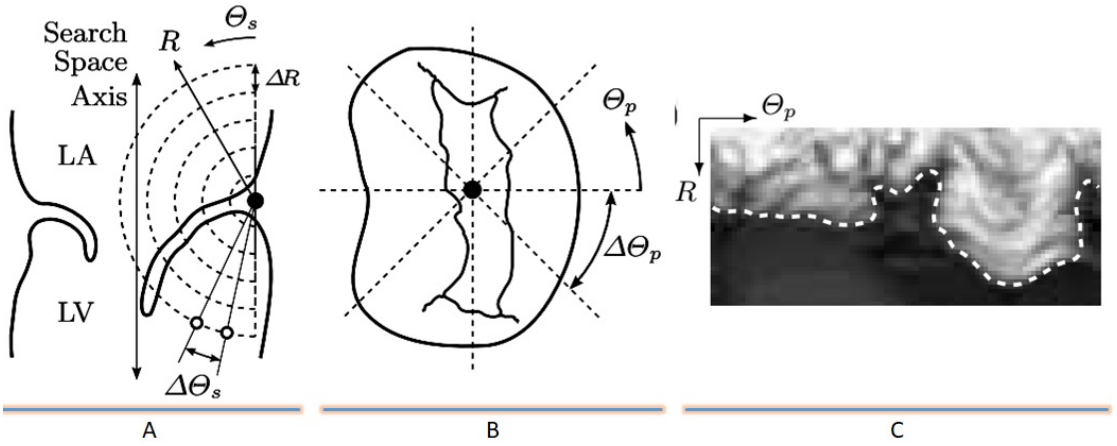

FIGURE 1.6: A) Search arc B) Atrial view of open valve C) Intensity image with trimming contour (adapted from [35])

Pouch et. al. [39] in 2012 proposed a semi-automatic method for the mitral valve modeling and valve morphometry, in 3D echocardiography. The method consists of three main parts, user initialized segmentation (see Figure 1.7), deformable medial modeling (see Figure 1.8), and extraction of the morphological features. The user initialization part consists of three steps. First, inserting two points above and below the mitral leaflet in the region of the left atrium and the left ventricle, respectively. Second, initializing the number of contour points (15-20) on the mitral annulus. Third, initializing the number of contour points (15-20) on the anterior mitral leaflet. The 3D binary mask was created using the obtained manual initialization and was refined by using a 3D active contour framework [28]. At this stage, the 3D segmentation describes the anterior and posterior mitral leaflet geometry. Deformable medial modeling [40] was used to show the compact shape representation (local bending/curvature) and to obtain the localized thickness. Later in 2014 [41], the authors proposed a fully automatic segmentation approach for the mitral leaflet segmentation that uses the multi-atlas joint label fusion

and deformable medial modeling, in 3D echocardiography (see Figure 1.9). A set of 3D mitral valve atlases were generated once (a set of images and their labels) and was repeatedly used for the segmentation of the target image (input). The first step was the image based registration process, in which the candidate segmentation were obtained by registering the atlases to the target image and between the set of reference atlases. The author used the FSL FLIRT tool [42] and ANTS symmetric normalization algorithm [43] to implement the registration step. Next, the joint label fusion provides the probabilistic segmentation of the target object (candidate labels). It was the important step because each atlas produces different segmentation results and thus a fusion strategy was required that uses majority or weighted voting to produce a probabilistic segmentation. Finally, based on the obtained segmentation of the target object, a 3D deformable medial modeling (a single non-branching cm-rep [44, 45]) was constructed to show the shape and geometry of the object using the medial axis.

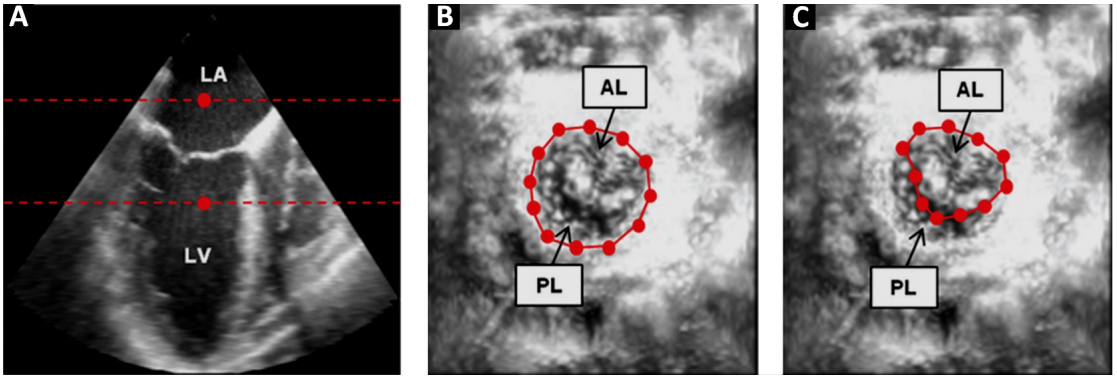

FIGURE 1.7: User initialization step: A) Identify region of interest in long axis view B) Series of points on annulus in atrial view C) Series of point on the AML in atrial view (adapted from [41])

Sotaquira et. al. [46] in 2015, proposed a semi-automatic segmentation method followed by quantifying the relevant morphological features of the mitral valve apparatus in a closed configuration (systolic phase), in 3D echocardiography. The first step was the initialization step, in which the user selects the frame at the end of the systole (closed valve), and initializes the location of the anterior and posterior annulus and the left atrium (3 points) (see Figure 1.10). The center of the annulus structure defines the origin of the coordinate system and was used to ensure that the manual initialization of the left atrium was correctly aligned with the mitral leaflet structure. Subsequently, manually locating the antero-lateral and postero-medial structure, orthogonal to the previously initialized plane (2 points) and finally locating four points on the anterior location of

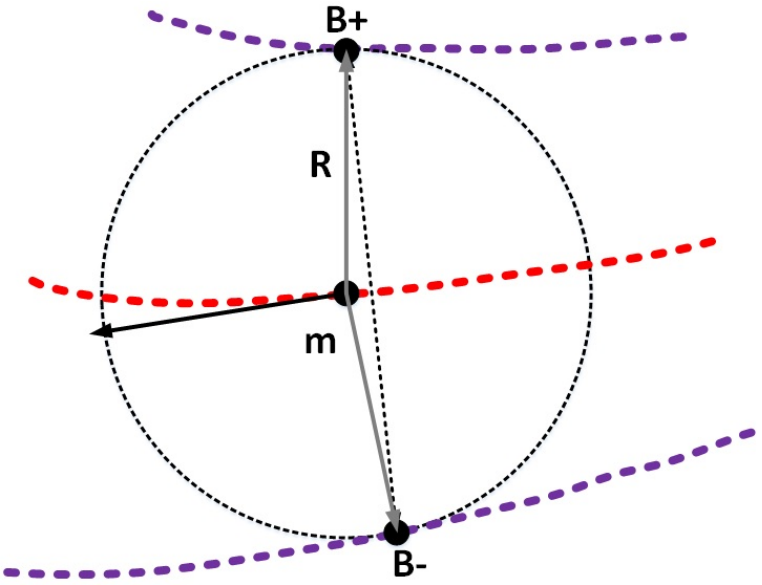

FIGURE 1.8: Medial geometry, R is the radius, $B+$ and $B-$ are the object boundaries, Red: medial surface m, Thickness measured as chord length (adapted from [39])

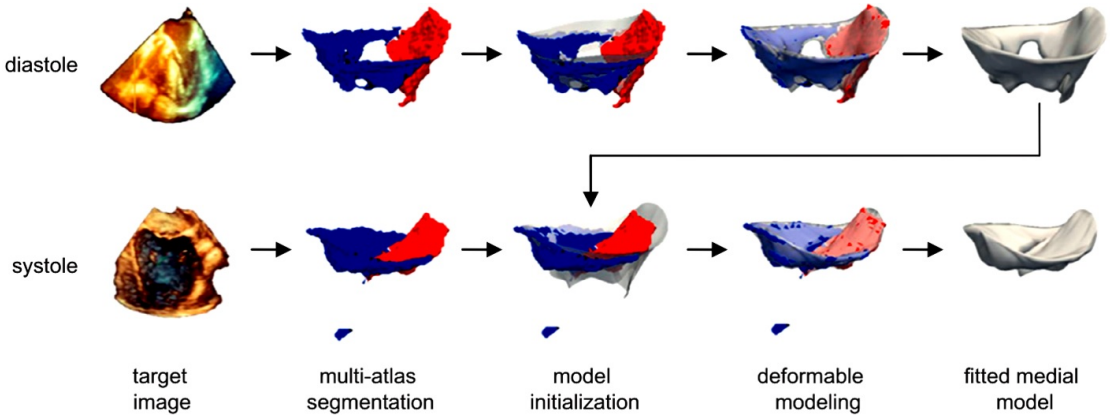

FIGURE 1.9: Pipeline of the mitral valve segmentation using multi-atlas framework (adapted from [40])

the mitral annulus, in four cut plane. The region of interest and the region of the search was defined based on the manual initialization, and then a weighted normalized cross-correlation [47] was computed between them. The junction point in the region of the search was defined by locating the point where the thin mitral leaflet tissue connects with the thicker ventricular walls, in a 2D cut plane. The region of the leaflet was automatically extracted by using the manual initialization. The medial axis and the binary mask of the mitral leaflet are then computed. The thickness of the leaflet (binary mask) was obtained by computing the Euclidean distance along the medial axis. Morphological operators such as the opening was used to obtain the junction enhanced image (mitral annulus). A cost image was obtained by averaging the weighted

normalized cross-correlation image and the junction enhanced image. Annulus location in other planes was estimated using the Dijkstra algorithm [48]. Finally, the mitral leaflet was segmented by using the prior computed 3D annular locations (see Figure 1.11). The negative of the cut plane was computed to assign the lowest intensity values to the center part of the leaflet. The corresponding intensity values were used as weights to construct a weighted graph and the minimum cost path was computed between the previously computed annular points using Dijkstra algorithm. Resulting in the segmentation of mitral leaflet as a medial axis.

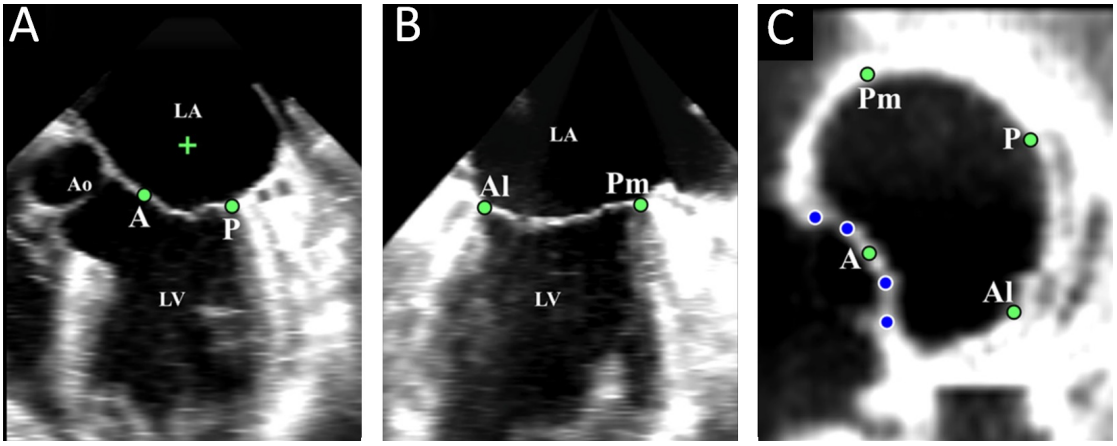

FIGURE 1.10: A) Select slice by navigating 3D volume with valve closed and insert 3 points B) 2 points selected from cut-plane orthogonal to that containing the A and P C) 4 points on four cut plane (adapted from [46])

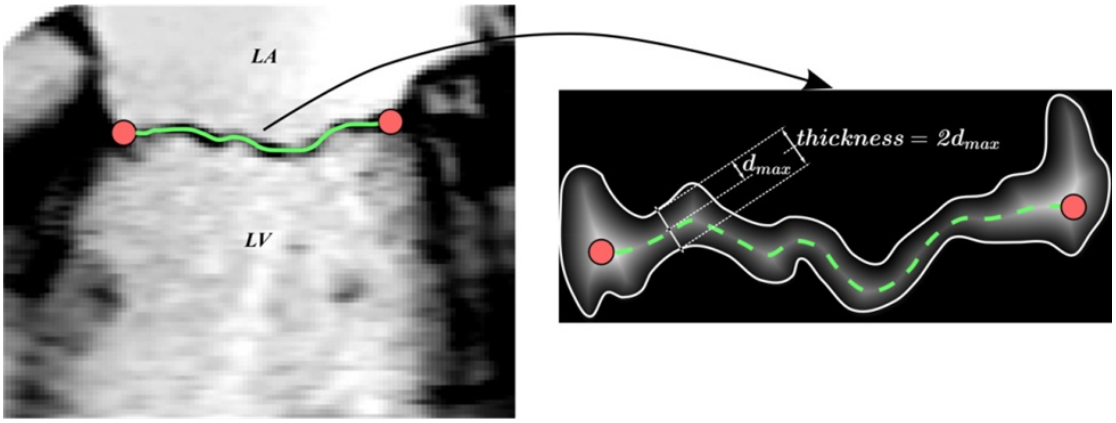

FIGURE 1.11: Left: Medial axis of the mitral leaflet between a pair of annular points, Right: Estimated thickness (adapted from [46])

1.4 Objective

The main objective of this PhD work is to segment the AML and track it throughout the cardiac cycle in 2D echocardiography videos. This is the first step towards a fully automatic diagnosis system for RHD. The conducted literature review (section 1.3) of the current state of the art methods in AML segmentation in echocardiography has revealed the following aspects:

- The AML and its neighbor regions such as the myocardium, papillary muscles, septum etc. share approximately the same intensity and texture, resulting in no discriminant features to distinguish one structure from the other.
- The AML shows fast motion, along with large and irregular deformations, making it a challenging problem for the existing methods to precisely predict its location over time.
- Existing algorithms require extensive user interaction, excessive parameter adjustment, suffer from over and under segmentation of the AML and are incapable of recovering from failure.

Given this, the main research questions that will be addressed in this PhD work are the following:

1. Is it possible to achieve high sensitivity and specificity of the AML segmentation and tracking (minimizing over and under segmentation) with high robustness?
2. Is it possible to minimize the number of failures, and/or provide the capability to the method to automatically recover from failure?
3. Is it possible to minimize the user interaction (fully automatic approach)?
4. Is it possible to achieve real-time performance?

1.5 Main Contributions

Throughout the PhD work, several contributions were proposed to the problem of AML segmentation and tracking in 2D echocardiography. Below is the brief summary of each:

1. The classical snake model was modified to achieve the better tracking performance. In the internal energy, a free boundary condition was used to obtain the open-ended contour that tracks the thin leaflet in a more natural way. In the external energy, instead of using the intensity and edge information of the image, we used the difference of Gaussians that were well localized with the increase in the capture range. The Harris cornerness measure was incorporated in the external energy to encourage the endpoint of the contour to stay at the tip of the AML, resulting in superior tracking performance. The algorithm fails in a large frame to frame displacement of AML.

2. We extended our previous approach, aiming to minimize the tracking failure in situations with large AML displacement. We proposed the integration of optical flow in the external energy of the classical snake model. The Lucus-Kanade optical flow with pyramid was used to quantify the displacement of structures, providing a displacement force that encourages the contour points towards the true boundary. The tracking ability was improved, but the algorithm still undergoes tracking failure and was computationally expensive.

3. The objective of this work was to achieve real-time performance and to minimize the tracking failure. We proposed a novel use of the combination of the morphological operators to obtain the best match of the AML in successive frames (rough AML estimation), further refined by the localized active contour. The tracking ability was further improved, but the algorithm still undergoes tracking failure and was slow to reach a real-time performance for the used hardware.

4. It is not certain how the active contour framework can address these limitations, providing the motivation to research a new approach. We proposed transforming the image space to the new space referred as the VM-mode. The VM-mode space is more adequate to robustly identify the AML throughout the cardiac cycle, providing a seed point per video frame. The seed point was later used to automatically initialize the localized active contour to segment the region of AML in each frame. The proposed method outperforms our previous contributions (no tracking failure). The limitation of this work was the problem of under-segmentation (missing the tip of AML).

5. To overcome the problem of under-segmentation. We proposed a method to reconstruct the whole AML from the VM-mode space, instead of reconstructing a single seed point identifying the AML. The method has successfully overcome the limitation of under-segmentation, but fails to avoid segmenting the unwanted regions and results into over-segmentation.

As a forthcoming contribution, we are integrating the shape constraints (PCA model) in the classical snake model. Aiming to minimize the problem of over-segmentation.

1.6 Resulting Publication

This Ph.D. work has contributed to the problem of segmentation and tracking in echocardiography videos, resulting in the following scientific publication

1.6.1 Journal Publications

- **M.S. Sultan**, N. Martins, E. Costa, D. Veiga, M.J. Ferreira, S. Mattos, M. Coimbra, "Virtual M-Mode for Echocardiography: A New Approach for the Segmentation of the Anterior Mitral Leaflet", (early access publication) in IEEE Journal of Biomedical and Health Informatics (DOI: 10.1109/JBHI.2018.2799738)

1.6.2 Book Chapter

- **M.S. Sultan**, N. Martins, E. Costa, D. Veiga, M.J. Ferreira, S. Mattos, M. Coimbra, "Tracking Anterior Mitral Leaflet in Echocardiographic videos using Morphological Operators and Active Contours", Communications in Computer and Information Science, Biomedical Engineering Systems and Technologies, 881, Chapter 9, (DOI:10.1007/978-3-319-94806-5_9).

1.6.3 Conference Publications

- **M.S. Sultan**, N. Martins, E. Costa, D. Veiga, M.J. Ferreira, S. Mattos and M.T. Coimbra, "A New Method for the Anterior Mitral Leaflet Segmentation in Echocardiography Videos using the Virtual M-mode Space", in Proc. IEEE EMBC, Honolulu, Hawaii, Jul 2018 (Accepted)

- **M.S. Sultan**, N. Martins, E. Costa, D. Veiga, M. Ferreira, S. Mattos, and M. Coimbra, "Tracking Large Anterior Mitral Leaflet Displacements by Incorporating Optical Flow in an Active Contours Framework", in Proc. IEEE EMBC, Jeju Island, South Korea, Jul 2017, (DOI: 10.1109/EMBC.2017.8037548)

- **M.S. Sultan**, N. Martins, E. Costa, D. Veiga, M. Ferreira, S. Mattos, and M. Coimbra, "Real-time Anterior Mitral Leaflet Tracking using Morphological Operators and Active Contours", in Proc. Int. Joint Conf. on Biomedical Engineering Systems and Technologies, BIOSTEC, Porto, Portugal, Feb 2017, (DOI: 10.5220/0006244700390046)

- **M.S. Sultan**, N. Martins, D. Veiga, M.J. Ferreira, and M. Coimbra, "Tracking of the Anterior Mitral Leaflet in Echocardiographic Sequences using Active Contours", in Proc. IEEE EMBC, Orlando, USA, Aug 2016, (DOI: 10.1109/EMBC.2016.7590889)

1.6.4 Other Contributions

- **M.S. Sultan**, N. Martins, D. Veiga, M. Ferreira, M. Coimbra, "Automatic segmentation of extensor tendon of the MCP joint in ultrasound images", in Proc. Int. Joint Conf. on Biomedical Engineering Systems and Technologies, BIOSTEC, Rome, Italy, Feb 2016, (DOI: 10.5220/0005692500710076)

- **M.S. Sultan**, N. Martins, D. Veiga, M. Ferreira, M. Coimbra, "Segmentation of Bones and MCP Joint Region of the Hand from Ultrasound Images", in Proc. IEEE EMBC, Milan, Italy, Aug 2015, (DOI: 10.1109/EMBC.2015.7319023)

1.7 Thesis Structure

The PhD thesis is organized as follows,

- Chapter 2 is dedicated to the medical background. It provides the basic understanding of the functioning of the heart, more particularly the rheumatic heart disease, its global burden, treatment cost and role of early identification of the disease by echocardiography screening.
- Chapter 3 is devoted to different kinds and variations of active contour frameworks and their applications for the segmentation of structures in echocardiography.
- Chapter 4 provides our contribution to the active contour framework for the tracking of the AML.
- Chapter 5 provides the details of our contribution to achieve the real-time AML tracking performance that uses the novel combination of basic mathematical morphological operators to estimate the initial boundary of the AML, further refined by fewer iterations of the active contour framework.
- Chapter 6 describes the novel approach to address the problem of segmentation, by proposing new image space called as the Virtual M-mode.
- Chapter 7 summarizes our contributions and concludes the thesis with the discussion.

Chapter 2

Medical background

In this chapter, we will present the medical background to better understand the disease and its consequences on the heart valves. Starting with the functioning and autonomy of the heart and it's valves. A broad view of the rheumatic heart disease is presented to understand the pathogenesis, the global burden, the cost the clinical manifestations, role of echocardiography and the WHF screening criteria.

2.1 Anatomy and Function of the Heart

The heart is a specialized muscular organ, which pumps blood throughout the circulatory system. The continuous and regular sequences of muscular contractions results as a powerful pump. The heart provides oxygen and nutrients to the whole body and removes carbon dioxide and other wastes via the circulatory system. The heart is roughly the size of a fist and weights about 280 to 340 grams in men and 230 to 280 grams in women [49]. The human heart consists of four chambers: left atrium, left ventricle, right atrium and right ventricle (See Figure 2.1).

Atriums are the chambers with smaller dimensions and less muscular walls. These chambers are known as blood-receiving chambers, that receive the deoxygenated blood through the vena cava and oxygenated blood through the pulmonary vein. The capacity of the left atrium is approximately 45ml and the right atrium is approximately 63ml. The ventricles are known to be stronger blood pumping chambers with high dimensionality and thicker muscular walls. They pump the blood to the lungs through the pulmonary

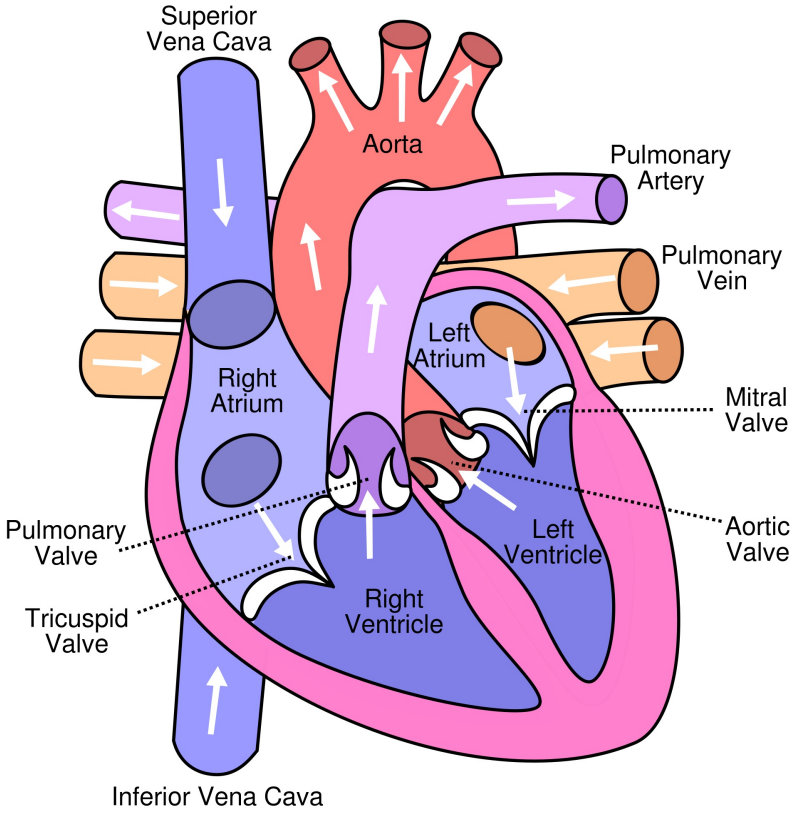

FIGURE 2.1: Human heart, showing four chambers, veins, arteries and valves (adapted from [50])

artery and to the whole body via the aorta. The capacity of the left ventricle is about 100 ml, whereas the right ventricle can hold up to 130ml of blood. The two sides (right and left) of the heart are separated by the septum, and each side consists of the atrium and ventricle. These chambers can be found in a state of systole (contraction) or diastole (relaxation). The heart has four valves that ensure the unidirectional flow of blood. The tricuspid valve consists of three leaflets connected with supporting structures as chordae tendineae and is located between the right atrium and the right ventricle. The mitral valve is also known as the bicuspid valve (two leaflets), is connected with chordae tendineae and is located between the left atrium and left ventricular (see Figure 2.4 & 2.3). The pulmonary and aortic valve have three leaflets without any connection with papillary muscles, and are located at the base of the pulmonary artery and the base of the aorta, respectively [51].

The heart rate for an adult varies from 60 to 100 beats/minute, with an average frequency of 1.2Hz. Each cardiac cycle consists of two major phases; the diastole, and the systole. During the diastole phase, the chambers fill up with the blood with an approximate

velocity of 0.7m/sec, the phase when a heart muscle relaxes. The ventricles continue to relax until the atrial pressure drops from a certain threshold, which results in the opening of the mitral and tricuspid valves. An electric signal that starts from the sinoatrial node (pacemaker of the heart) activates the bundle of His and the Purkinje fibers at the beginning of the systole phase. This electric activity causes the ventricular chambers to start contracting, which significantly increases the pressure of the right ventricle and left ventricle, hence the mitral and tricuspid valves close (see Figure 2.2). The pulmonary and the aortic valve open as the ventricular pressure exceeds the arterial pressure. The blood flows to the lungs and the body through the pulmonary artery and the aorta, respectively. After ejecting blood from the ventricles, the pressure drops resulting in closure of the pulmonary and aortic valves, while the mitral and tricuspid valves open [52].

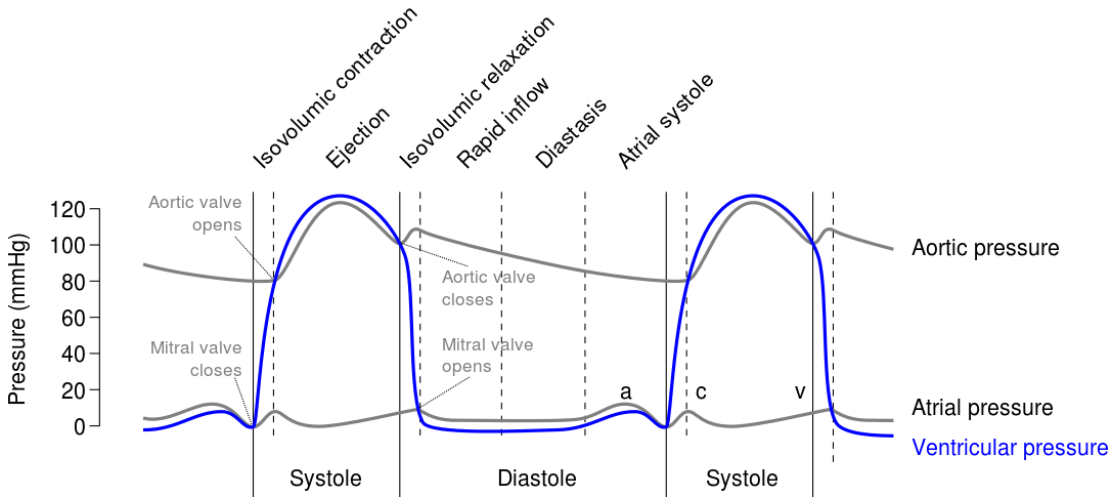

FIGURE 2.2: Cardiac events: systole and diastole, opening and closing pattern of Mitral, aortic valve Vs aortic, atrial and ventricular pressure (adapted from [53])

2.2 Anatomy and Dynamics of the Mitral Valve

The mitral heart valve is a structure that lies between the left ventricle and the left atrium, and typically covers an area of $4-6\ cm^2$. The anatomical structure of the mitral valve is fairly complex and consists of two leaflets, annulus, Papillary Muscles (PM) and tendineae (see Figure 2.3). The PM are the finger-like projections originated from the left ventricular myocardium, from both anterolateral and posteromedial sections. The tips of the PM are connected with inelastic chordae tendineae which support the mitral valve leaflets and are arranged to form a ring. The bottom of the mitral valve leaflets is

connected with the posterior and anterior annulus. The combined structure of leaflets and annulus constitutes the anatomical junction connecting the left atrium and the left ventricle [54, 55]. The normal valve function is to prevent regurgitation during systole (act as one-way inlets) and allows the flow of blood to move from the left atrium to the left ventricle. The mitral valve functionality may be affected by the age and the cardiovascular diseases, such as the RHD.

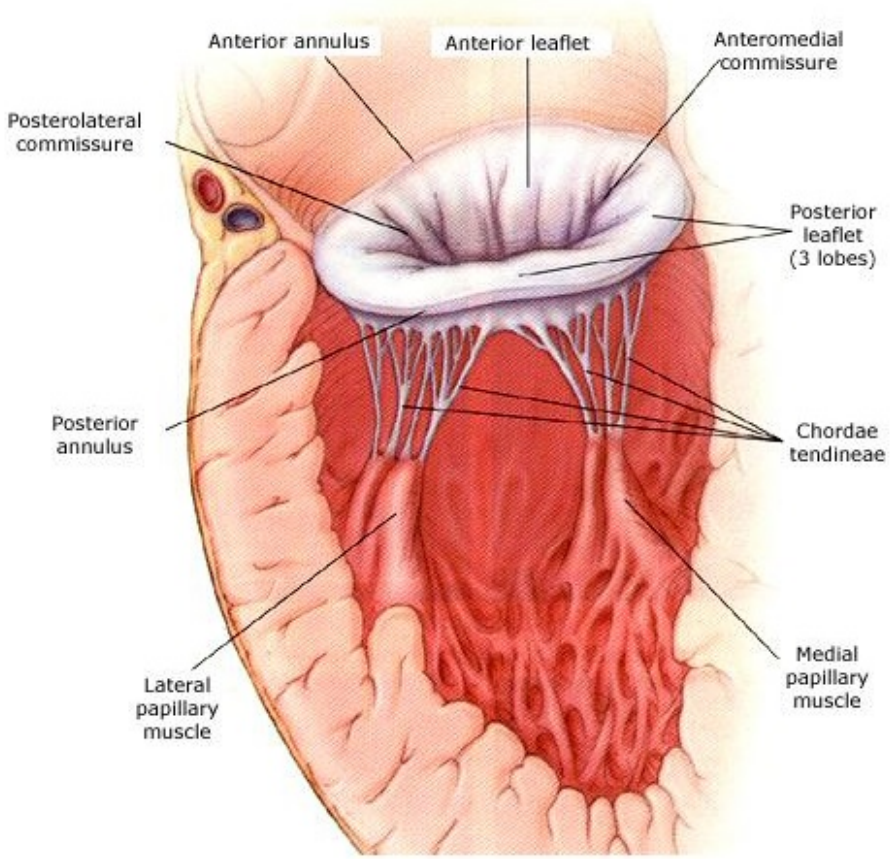

FIGURE 2.3: Mitral valve components (adapted from [56])

The **mitral valve leaflets** in humans usually have the similar eyelid-like appearance that guards the opening between the left ventricle and left atrium. However, the anatomy may vary from person to person. The mitral valve consists of two thin leaflets which noticeably differ in structure (see Figure 2.4); the one with semi-circular shape and the long leaflet is defined as an Anterior Mitral Leaflet (AML) and is adjacent to the aortic valve, whereas the other is shorter and has a quadrangular shape, is connected with the myocardium and defined as the Posterior Mitral Leaflet (PML). There are small indentations and bumbs on the PML, called scallops, while the AML is smoother along

its free edges. The tendons are attached with leaflets to prevent them from collapsing and also make them taut [54, 57].

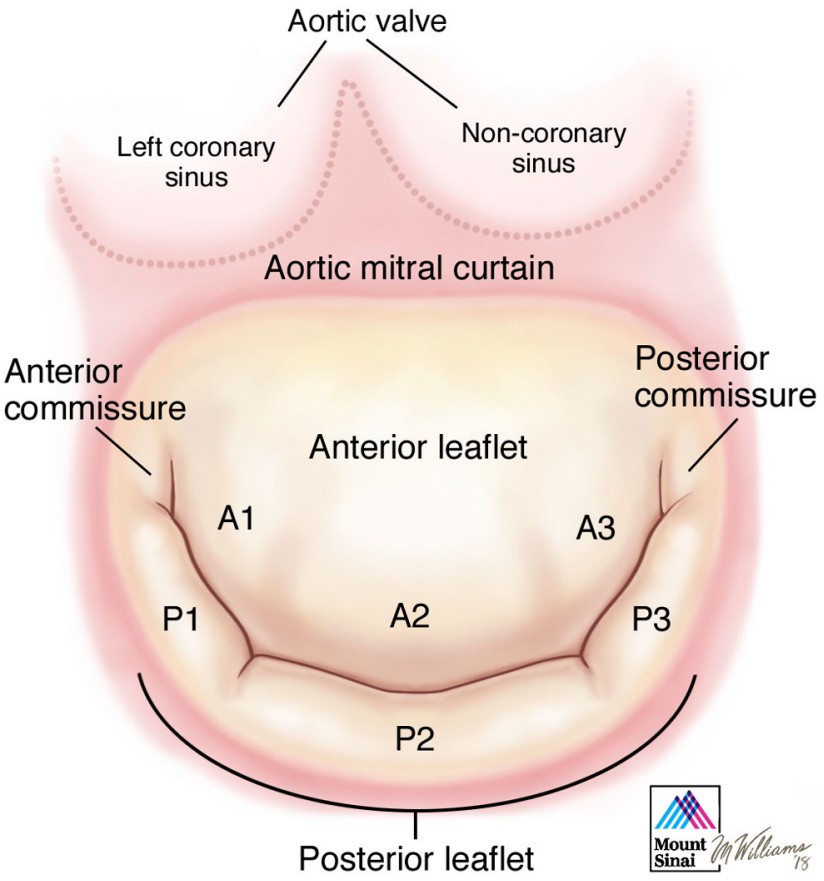

FIGURE 2.4: Anatomy of the mitral valve (adapted from [58])

The junction which separates the left atrium from the left ventricle, and which is attached to the mitral valve leaflet is known as the **mitral annulus** (3D saddle shape, like a ring). Based on the connection with the mitral leaflets, the annulus is divided as the anterior and posterior annulus. The shape and size of the mitral annulus change continuously during the whole cardiac cycle. The contraction of the left atrium takes place at the end of atrial systole, which results in a decrease in the size of the mitral annulus [59].

There are two **papillary muscles** located at the anterolateral and posteromedial positions, arising from the area between the apical and the left ventricle. The function of PM is to prevent regurgitation (backward flow). The PM starts contracting at the end of the ventricular diastole and thus maintain some tension [57].

The chords are fan-shaped structures originated from the PM and inserted into the mitral leaflets. There are three types of **chordae tendineae**, the chords which are

attached to the rough zone, attached to the ventricular surface and the tertiary chord connected with the PML. The thickness varies for each chord. Commonly the thinnest are connected with the free leaflet margin and the thickest are attached away from the free leaflet margin. This physiological structure helps to control the systolic pressure. The function of chordae tendineae is to prevent the flow of blood back to the left atrium. When the systole phase of the left ventricle starts, the mitral valve closes due to intra-ventricular pressure. The chordae tendineae helps to keep the leaflets tightly attached together and prevent the valves from opening in the opposite direction to cope with the intraventricular pressure [57].

2.3 Pathologies of the Heart Valve

Heart valves control the unidirectional flow of blood. In pathological cases, the heart valves suffer two major malfunctions. One is regurgitation and the other is stenosis (see Figure 2.5). In regurgitation, the heart valves don't close properly, which results in a leakage and the blood starts flowing backward. In stenosis, the heart valves don't open properly due to stiffened leaflets, which result into a narrowed path. Therefore, the blood is constrained to flow through the valves. These pathologies usually occur due to RHD and congenital heart disease and if not treated could result in a serious condition of heart failure. In severe cases, sudden death can occur.

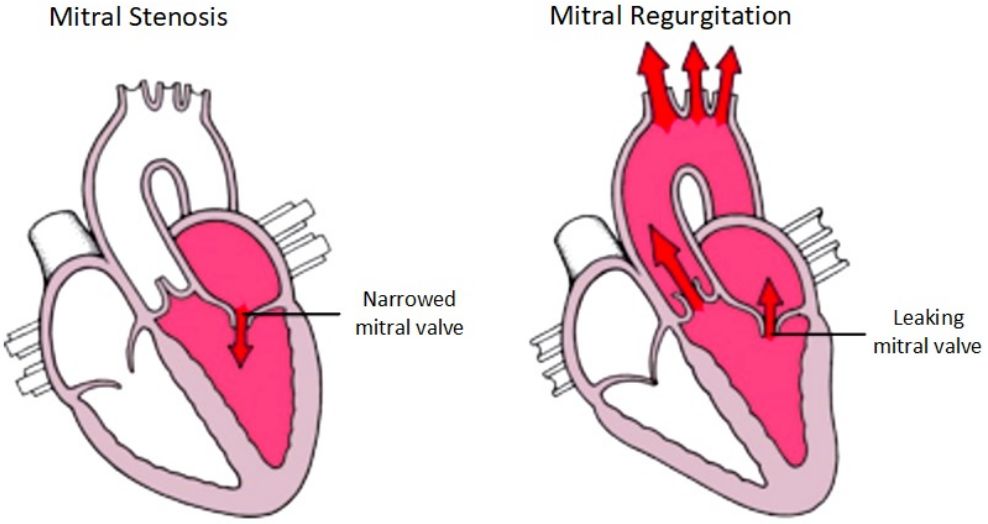

FIGURE 2.5: Regurgitation and stenosis, adapted from [60]

2.4 Rheumatic Heart Disease

RHD is the serious consequences of ARF. ARF is the inflammatory disease that usually starts in childhood between the ages of 5 to 15 years, and whose repeated episodes slowly damage the valves of the heart, more often the mitral valve.

2.4.1 Pathogenesis of Rheumatic Heart Disease

ARF is an autoimmune disease caused by group A streptococcus and is usually found on pharynx and on the skin [1] (see Figure 2.7). Even though no direct relation was found between the previous streptococcal infection and the ARF, the infection treatment results in a sharp decrease in ARF [2]. This provides a significant measure to argue that ARF results from a streptococcus infection. It is an autoimmune disease that tends to run in the families which live in poor health conditions. The symptoms of streptococcal infection start appearing after 1 to 4 weeks of the attack. It was observed that the disease symptoms vary a lot from case to case. The main symptoms are a slight fever, joint pain, tiredness and sometimes even nose bleeding. In severe cases, the fever may reach 40°C and continues for several weeks. However, the fever may take only a couple of weeks in common cases. Around 50 to 65 % of the patients are at risk of developing the RHD after an initial episode of the ARF [61]. Since the RHD doesn't occur after the very first attack, an early detection is considered vital to define the disease burden and to control the disease progression.

Repeated episodes of ARF lead to further inflammatory damage and weaken the heart valves. The most common consequences are the inflammation and the vegetation on the heart valves, more often the mitral valve is involved (see Figure 2.7). With the passage of time, the inflammation and healing process stiffens the heart valves and leaves scars that thicken these valve leaflets. As a result of this damage, the heart valves may become pathological, causing blood to leak from the closed valves or restricting the flow of blood. Since no method yet has been discovered to directly attack the disease, the only available treatment is to control recurrences of ARF. Penicillin is prescribed in case any streptococcal infection is found and is followed for many years with some other medicines to reduce the swelling and the pain [62].

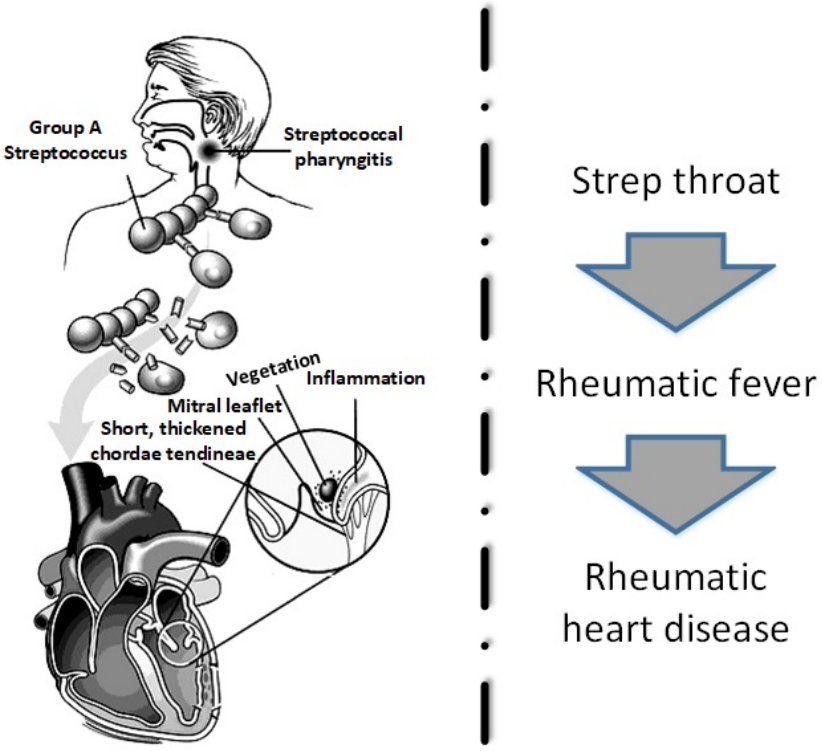

FIGURE 2.6: Repeated episodes of ARF and the mitral valve damage (adapted from [63])

2.4.2 Global Burden of Rheumatic Heart Disease

Over the past decade, the ARF and RHD become a rare disease in developed countries. Firstly, due to the access to medical care services and secondly, due to the improvement in socioeconomic conditions. However, it is still the leading non-communicable cause of morbidity and mortality in the developing countries. Mainly, due to unavailability of the health care, overcrowding and poor hygiene conditions.

RHD is more likely to develop in individuals suffering from ARF. In one study, it was estimated that in 10 to 20 million individuals suffering from the ARF, around 6 million are at high risk of developing RHD each year, resulting in significant childhood deaths [3, 4]. The estimated prevalence of the RHD cases in 2005 was 15.6 to 19.6 million globally, where 2.4 million are children (aged between 5 to 15 years), resulting in 233,000 deaths and 282,000 new cases per year [3, 4]. A significant decline in deaths due to the RHD was presented in a study [7], reporting around 462,600 deaths in 1990 that decreased to 345,100 in 2010. In another study (1990-2013) [5, 64], it was estimated that the disease affects about 32.9 million people and is responsible for 1.4 million deaths per year (see Figure 2.7). In the recent study (1990 - 2015) [65], the estimations suggest

around 33.4 million cases of the RHD globally, with 10.5 million cases in advance stage that requires surgery procedures and about 319,400 reported deaths. This study reflects the significant decline of mortality from 1990 to 2015 globally. However, the prevalence highly depends on the location and it was estimated highest in South Asia, central sub-Saharan Africa etc, as seen in Figure 2.7.

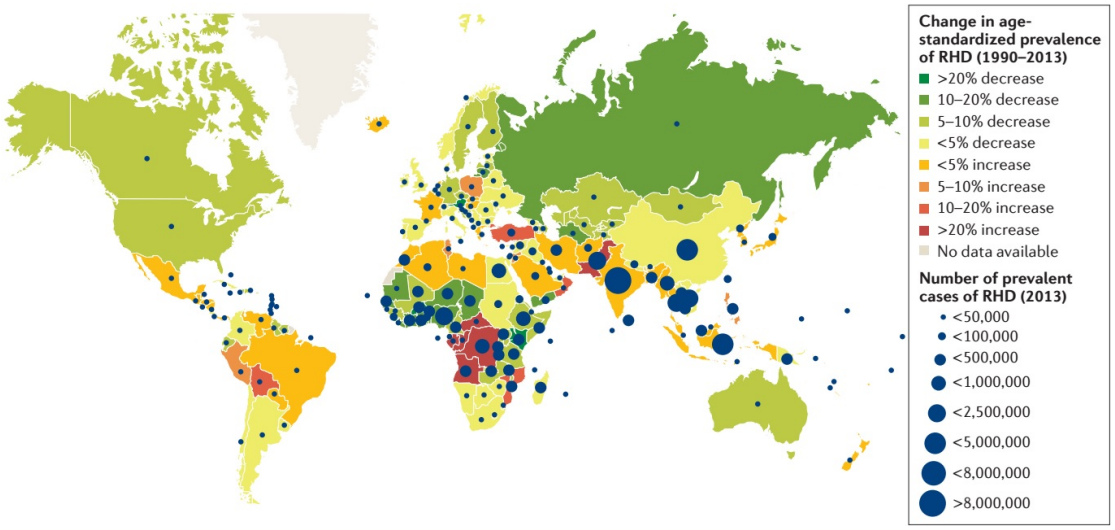

FIGURE 2.7: The global burden of RHD.: from 1990 to 2013. (adapted from [64])

The biggest limitation is that RHD is clinically silent in about 90 % of the cases in its early stages, meaning that the early valve damage doesn't show any clinical murmurs (no audible murmurs) [12, 66, 67]. Following this fact, many people are unaware of their disease and thus don't have any known history of ARF, until their valves are seriously damaged and requires corrective surgery, or are accidentally diagnosed during a medical examination [68]. The World Health Organization (WHO) and World Heart Federation (WHF) have proposed to achieve a significant decrease in the death rate (about 25 %) due to non-communicable disease like RHD by 2025 [69]. The selected targets are achievable for the RHD, especially for the group of children under the age of 25 years, mainly due to the availability of inexpensive and effective control strategies [70]. If the RHD is untreated, patients usually do not live beyond 25 years old [71].

2.4.3 Clinical Manifestations of Rheumatic Heart Disease

Mitral regurgitation is common in the early stages of the RHD and can be seen as valvular lesion [72–74]. However, the mild to moderate mitral regurgitation with and without other pathologies may remain asymptomatic for years, until entering into a

severe stage with a high degree of valve damage. The most common morphological changes due to RHD are the leaflet thickness, excessive/restricted leaflet motion, and short chordae tendineae. The mitral stenosis is supposed to develop in advance stages, when the mitral leaflets fused due to persistent valvular inflammation [10]. Following the disease progression, the severe stages of the RHD usually require a surgical procedure, such as valve repair and valve replacement.

2.4.4 Cost of Rheumatic Heart Disease

In the severe stages of RHD, the leaflets undergo irreversible damage, resulting in dysfunction of the valve. The majority of these patients requires lifesaving surgery [75, 76]. Surgery is a very risky process and the consequence can be re-operation, a higher rate of valve failure and even mortality. In developing countries, surgery is expensive due to other factors like unavailability of the equipment, shortage of human resources, and training opportunities. Eventually, these factors add-up, resulting in long delays and untreated patients undergoing heart failure. The indication for a surgery is most commonly due to severe mitral regurgitation [77]. The estimated cost of health in Auckland were $ 3.60 million [78], where the cost of the RHD management was around $ 2,564,790, about 71 % of the total cost. It includes the nonsurgical admission cost of about 34 %, surgical admission cost of about 23 % and outpatient clinical appointment cost up to 14 %. The hospital admission cost due to the ARF and the RHD in a group of all ages in New Zealand from 2000 to 2009 estimated using a DRG-based system, amounted to $ 12.0 million [79]. The open heart surgery to fix the problem of mitral valve regurgitation with a bio-prosthetic valve costs about $ 11,200 in Nigeria [80]. The surgery has a high risk of failure that can be prevented by the early detection of the RHD. The disease progression can be controlled by using the most cost-effective ($ 50 per person) benzathine penicillin as secondary prophylaxis [6].

2.4.5 Pattern of Valvular Involvement

Previous studies [81, 82], reported that the mitral valve is affected in the majority of the RHD cases (96 %), with and without the involvement of the other heart valves (see Figure 2.8A). The reason for this specific pattern is not very clear. However, researchers believe that it happens due to the dominance of the left part of the heart. In another

study [83], the number of cases with regurgitation and stenosis with respect to each heart valve due to the RHD was reported (see Figure 2.8B). The computed statistics showed that the mitral valve was predominantly involved in these conditions due RHD.

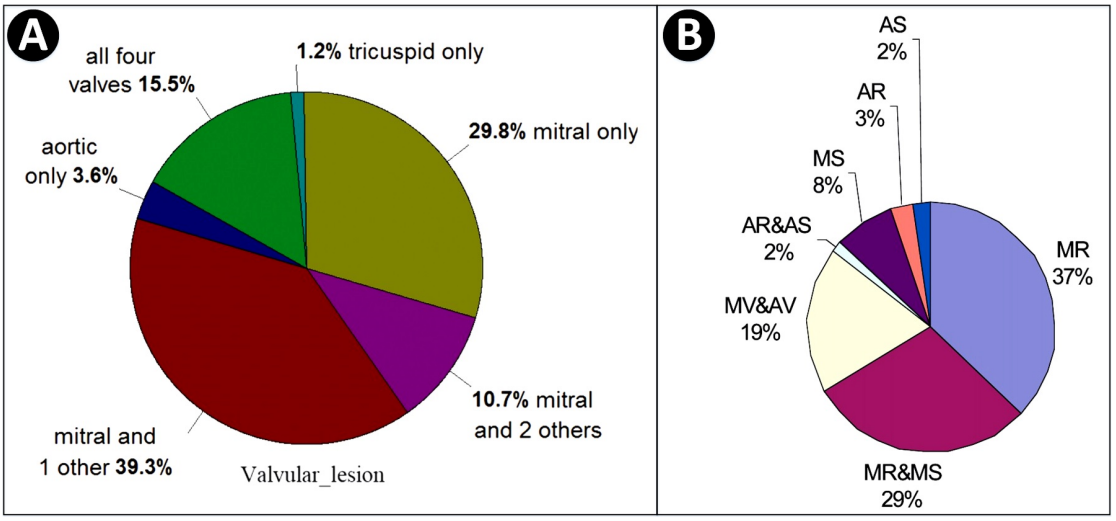

FIGURE 2.8: A) pattern of valve involvement B) Affected valves with pathologies. MR: mitral regurgitation, MS: mitral stenosis, AR: aortic regurgitation, AS: aortic stenosis, MV: mixed mitral valve diseases, AV: mixed aortic valve diseases (adapted from [81, 83])

2.5 Role of Echocardiography Screening

The individuals with RHD have history of strep infection and thus can be identified by blood test and throat culture. The valve involvement can be confirmed by auscultation, hearing the murmur sound produced by the regurgitation (valve leakage) or when the leaflets rub against each other. However, the auscultation is not sensitive to detect sub-clinical cases in which the murmur is not audible. The echocardiography has proven its sensitivity and specificity to detect individuals with sub-clinical RHD [11–15] (see Figure 2.9). The study has shown the large burden of sub-clinical RHD and has shown the superiority of the echocardiography over the traditional auscultation [14, 84, 85]. The early detection by echocardiography paves the way to prevent the RHD progressing by using the penicillin.

2.5.1 WHF Criteria for Echocardiographic Diagnosis of RHD

Echocardiography screening has high sensitivity and specificity to define the RHD burden in the endemic regions of the world. The WHF in 2012 standardized the screening

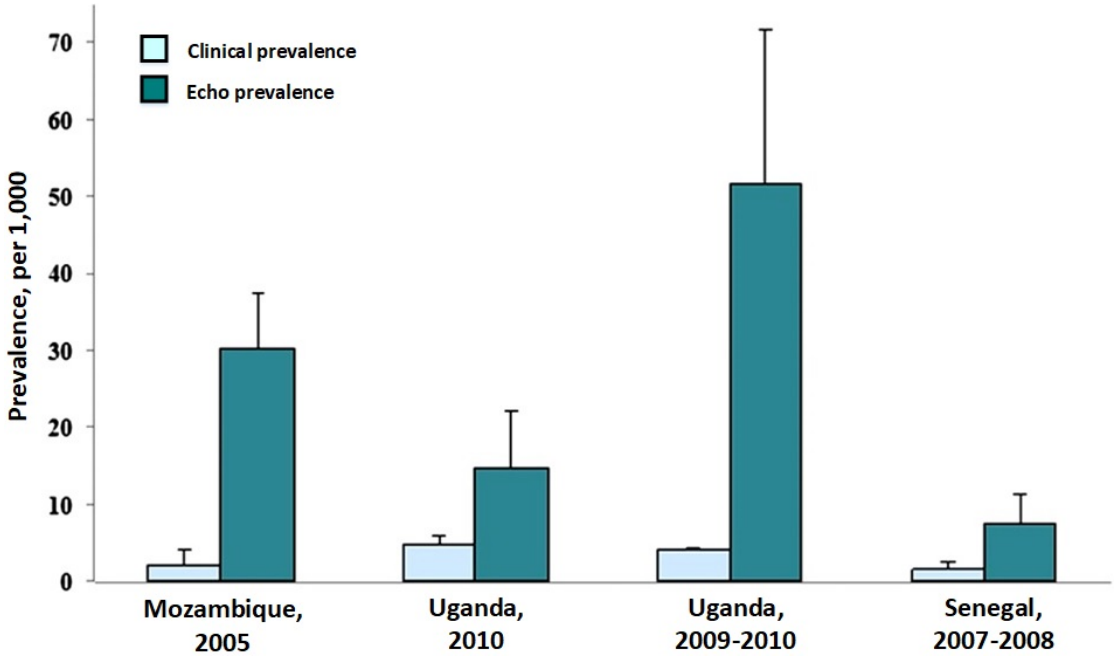

FIGURE 2.9: Clinical versus echocardiography based screening in school children at Africa. (adapted from [86])

criteria, based on an evidence-based consensus for the individuals with age lower than 20 years [87]. It includes the quantification of morphological parameters, and the quantification of the regurgitation jet via Doppler. The WHF criteria helps to define the RHD burden in high prevalence areas and classify the RHD cases as normal, definite and borderline. Definite RHD cases were defined as,

1. Mitral regurgitation with at least two morphological features of the mitral valve.
2. Mitral stenosis with the mean gradient of greater than 4 mmHg.
3. Aortic regurgitation with at least two morphological features of aortic valve.
4. Mitral valve and aortic valve classified as borderline RHD.

Borderline RHD cases were defined as

1. At least two morphological features of the mitral valve.
2. Mitral regurgitation.
3. Aortic regurgitation.

Even though, the previous studies had praised the sensitivity of the echocardiography screening, there are still limitations of using this technique. First, the availability of echocardiography equipment in the RHD prevalent area. Second, equipment with Doppler capabilities is expensive. Third, the unavailability of properly trained people to correctly perform the screening [88].

WHF had recommended the use of Parasternal Long AXis (PLAX) window for the mitral valve analysis (see Figure 4.1), because it is the most suitable window to access and measure the morphology of the AML [10, 89]. It helps to quantify the morphological changes of the AML, like the thickness, shape, restricted and excessive tip motion. To obtain the better view of the AML from the PLAX window, it is recommended to make the structure of the septum as horizontal as possible, and only the mitral and the aortic valve should be visible. However, the PML had shown a low level of inter-observer agreement and thus not recommended for the measurements from the PLAX window.

Chapter 3

Active Contours for Echocardiography Image Segmentation

Image segmentation is the process of partitioning a digital image into multiple regions. Each region has some characteristics and properties, like intensity, texture or color that makes it significantly different from its adjacent regions. The objective of segmentation is to present an image in such a way (locate objects/boundaries) that is more meaningful, easier to analyze and quantify. Segmentation is the first step towards image analysis and the recognition of its unique patterns, and the quality of image segmentation directly affects the results.

Low-level segmentation methods like thresholding drastically reduce in a single step the amount of data to process, resulting in the loss of important information. Given the rich nature of the medical images, low-level segmentation is usually not sufficient to obtain a robust segmentation due to the presence of noise and the low quality of images [90]. Therefore, high-level techniques (model based methods) like deformable models [24], active shape models [91], or active appearance models [92] are more adequate for the medical images. They are more sophisticated but also more computationally expensive.

3.1 Active Contours

Active contour models, also known as deformable models or snakes were first proposed by Kass et al. [24] and were extensively studied and used for the medical image segmentation [93]. Active contour models can be divided into two main classes, the Parametric Active Contours (PAC), and Geometric Active Contours (GAC). In this section, we provide the fundamental concepts and mathematical foundation of each type of active contour model.

A PAC model consists of a parametric framework for a curve/contour that evolves towards certain local image features, which behave like an elastic band. The three most popular PAC models are discussed here

3.1.1 Snake Model – PAC

The snake model [24] is a parametric curve $V(S) = (x(S), y(S))^T \quad S \in [0,1]$ that deforms under geometric shape constraints and the image energy constraints over a series of iterations (time steps) (see Figure 3.1). The total energy of the snake model consists of the internal energy and the external energy (3.1).

$$\mathrm{E}_{Snake} = \int_0^1 \left(\overbrace{1/2 \left(\underbrace{\alpha \left\| \frac{\partial V}{\partial S} \right\|^2}_{Elasticity} + \underbrace{\beta \left\| \frac{\partial^2 V}{\partial S^2} \right\|^2}_{Stiffness} \right)}^{Internal} + \overbrace{\mathrm{E}_{img}(V) + E_{con}}^{External} \right) ds \tag{3.1}$$

The internal energy typically consists of the first derivative and the second derivative of contour. The first derivative holds the contour points together and encourages points to be equally spaced (elasticity). The second derivative controls the bending of the contour points (stiffness). The weighting parameters, α and β controls the relative importance of the elasticity and stiffness, respectively.

The external energy consists of two parts: the image energy E_{image}; and the constraint energy E_{con}. E_{image} is responsible for attracting the curve towards the salient features of the image, like edges, intensity (light/dark) and terminations. The image energy is defined below;

$$\mathrm{E}_{img} = w_{line}E_{line} + w_{edge}E_{edge} + w_{term}E_{term} \tag{3.2}$$

Where, E_{line} is the intensity of the image I, E_{edge} is the gradient of the Gaussian smoothed image $E_{edge} = -\left|\nabla\left[G_\sigma * I\right]\right|^2$, and E_{term} is based on the curvature of lines in a Gaussian smoothed image (3.3) and is responsible of attracting the curve towards the corners and terminations. The weight w_{line}, w_{edge} and w_{term} controls the relative importance of each energy.

$$E_{term} = \int_0^1 \frac{C_{yy}C_x^2 + C_{xx}C_y^2 - 2C_{xy}C_xC_y}{\left(C_x^2 + C_y^2\right)^{\frac{3}{2}}} ds \tag{3.3}$$

The constraint energy E_{con} allows the user to interact with the model and pushes the curve out of any undesired local minimum using the "spring" and "volcanos" force [24]. One of the reasons to use the constraint energy is to improve the capture range that provides a high-level guidance to the curve during convergence. The spring force pulls the curve towards itself and the magnitude of the force depend on the distance between the spring point and the curve (3.4).

$$E_{spring} = K(S - V) \tag{3.4}$$

Where, S is the position of the spring, V is the curve and K is the weight. Volcano force pushes the curve away and the magnitude of the force is inversely proportional to the distance between volcano point and the curve (3.5).

$$E_{volcano} = \frac{V - C}{R} \tag{3.5}$$

Where V is the curve, C is the volcano point and R is the distance between the volcano point and the curve.

Searching for a solution implies transforming the problem into an energy minimization one. It infers that when the curve is located on an object boundary (at edges), the total energy (3.1) function reaches a minimum. Euler Lagrange optimization is typically applied, providing the final equation of the snake model (3.6).

$$\alpha \frac{\partial^2 V}{\partial S^2} - \beta \frac{\partial^4 V}{\partial S^4} - \nabla E_{ext} = 0 \tag{3.6}$$

Finally, the equation 3.6 is solved by taking the partial derivative of v with respect to t, showing that the curve evolves over a series of iterations (3.7).

$$\frac{\partial V}{\partial t} = \alpha \frac{\partial^2 V}{\partial S^2} - \beta \frac{\partial^4 V}{\partial S^4} - \nabla E_{ext} \tag{3.7}$$

The left hand side $\frac{\partial V}{\partial t}$ approaches zero when the curve stops evolving, which at the same time the right hand side satisfies the Euler-Lagrange equation and approach zero.

The main limitation of this work lies with the image energy that has a limited capture range. It happens because the edges are located only at abrupt changes of intensity (grayscale). However, regions are homogeneous from inside and thus there is no significant change in intensity. Owing to this problem, the initial contour must be located near the real boundaries of the object, to converge properly. The parameter adjustment of the internal energy is essential. In a practical applications, it is difficult to obtain the appropriate parameters, resulting in shrinking behavior of the curve and/or slow convergence of the active contour. The second limitation is the inability of the method to segment concave regions. This happens because the direction of the external force is in opposite directions inside the concave shape objects, resulting in a cancellation of the external force. Several methods such as a balloon force model, or gradient vector flow were proposed to improve the capture range and to improve the segmentation performance inside concave shape objects.

3.1.2 Balloon Force Model – PAC

The pressure force [94] was introduced in the external energy term of the original snake model [24] to overcome the limitation of the initialization close to the object boundaries. The evolution of the curve under the pressure force resembles a balloon being inflated in 2D and is thus called as the **balloon force model** (see Figure 3.2). In the snake model [24], the curve shrinks due to the influence of internal energy in the absence of image energy. However, in the balloon force model [94] the curve expands due to influence of the pressure force in the absence of image energy.

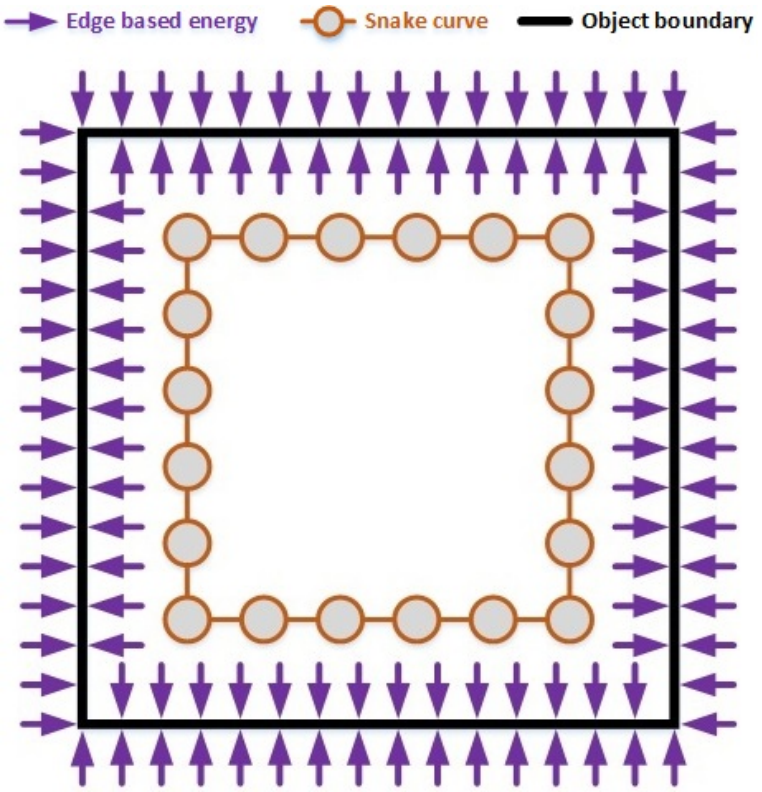

FIGURE 3.1: Snake model

At each point on the curve, the pressure force acts normal to the curve. The modified external energy consists of the external energy of a snake model (image) and the pressure force (3.8).

$$E_{ext} = W_{ballon} n(s) - W_{img} \frac{\nabla E_{img}}{\|\nabla E_{img}\|} \tag{3.8}$$

Where, W_{ballon} is the weight of the pressure force and its sign decides if the curve shrinks (negative) or expands (positive). $n(s)$ is the normal vector at each point on the curve $V(s)$. The purpose of the pressure force is to push the curve towards the object boundaries until trapped in a gradient minimum (edges). The second term in the equation is the normalized version of the image energy with the weight W_{img}.

The limitation of this model is the problem of leakage at weak edges. It means that the curve passes beyond the weak boundaries and never comes back. The balloon model is ineffective in segmenting the concave part of the object. Depending on the application, it is easier or harder to decide the sign of the weight W_{ballon}. However, deciding the optimal weight is quite challenging. In general, the weight parameter of the pressure

force should be smaller than the weight parameter of the image energy, in order to stop the curve at the true shape boundaries. Too small or too large weight of the pressure force results in a bad segmentation result.

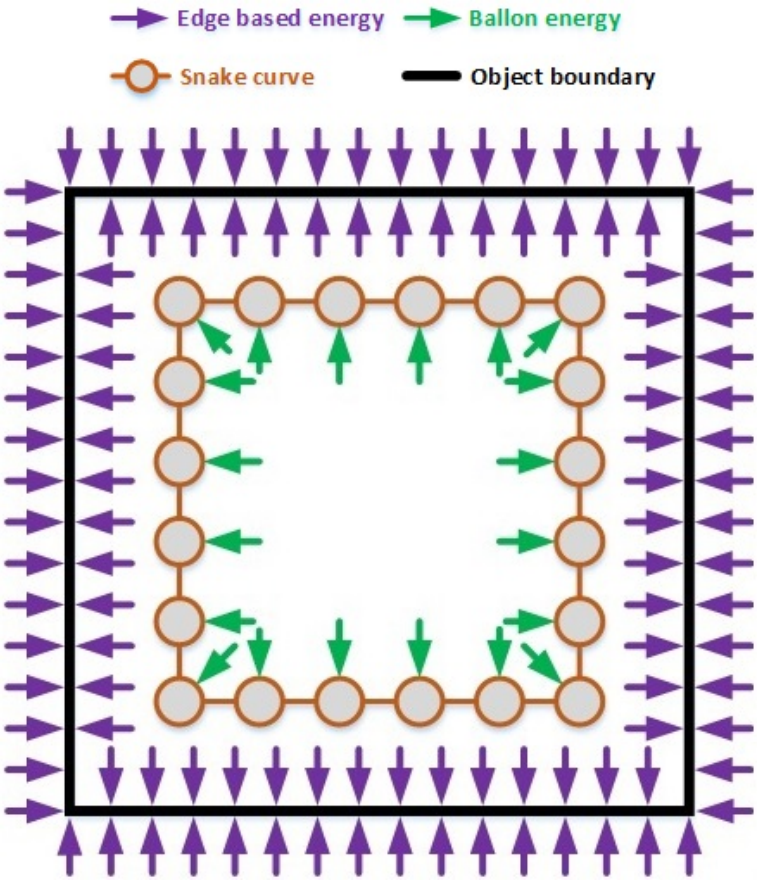

FIGURE 3.2: Balloon force model

3.1.3 Gradient Vector Flow Model – PAC

The limitation found with the balloon active contour model [94] was the inappropriate weight of the pressure force, that may overwhelm the curve at object boundaries with low gradient magnitude. The Gradient Vector Flow (GVF) [95] was proposed to improve convergence of the curve into concave regions (U shape objects) and to improve the capture range from both inside and outside of the object of interest. The GVF replaces the external energy (3.6) in the original snake model (3.3).

$$\alpha \frac{\partial^2 V}{\partial S^2} - \beta \frac{\partial^4 V}{\partial S^4} - E_{GVF} = 0 \tag{3.9}$$

Where in [95], elaborated three important features of the edge map that were derived from the image I. First, the gradient of the image is a vector that points towards the boundary of the object. Second, the obtained vectors have a larger magnitude at the vicinity of the object boundaries. Third, the region and the background are homogeneous from inside, with no abrupt change in intensity, resulting in approximately zero gradient vector.

The GVF is the vector field $f(x,y) = [u(x,y), v(x,y)]$ that minimizes the following equation (3.10).

$$E_{GVF} = \iint \overbrace{\mu\left(u_x^2 + u_y^2 + v_x^2 + v_y^2\right)}^{smoothing} + \overbrace{\|\nabla e\|^2 \|f - \nabla e\|^2}^{data} \tag{3.10}$$

Where, the parameter μ is known as regularization weight and is responsible for adjusting the tradeoff between the first term (smoothing term) and the second term (data term) in equation (3.10). The e shows the edge map of the image I. The value of μ depends on the level of noise present in the image. If the image has a high level of noise, it is recommended to use the large value of μ. The sum of the partial derivative of the gradient field (smoothing term) is dominating in situations when the edge gradient is small (data term) and vice versa. Finally, the equation (3.10) is minimized by using the Euler-Lagrange equation (3.11). Where, ∇^2 is the Laplacian operator.

$$\begin{aligned} \mu\nabla^2 u + (u - e_x)\left(e_x^2 + e_y^2\right) &= 0 \\ \mu\nabla^2 v + (v - e_y)\left(e_x^2 + e_y^2\right) &= 0 \end{aligned} \tag{3.11}$$

Equation 3.11 can be solved by taking the partial derivative of u and v with respect to time t, and solving it iteratively (3.12).

$$\begin{aligned} \frac{\partial u}{\partial t} &= \mu\nabla^2 u + (u - e_x)\left(e_x^2 + e_y^2\right) \\ \frac{\partial v}{\partial t} &= \mu\nabla^2 v + (v - e_y)\left(e_x^2 + e_y^2\right) \end{aligned} \tag{3.12}$$

The above equation provides the intuition that within regions, the data term approaches zero and thus the value of u, v is determined by the Laplacian, showing the effect of "filling-in" of the homogeneous regions.

The GVF vectors originates from inside the region and points toward the boundary (see Figure 3.3). The boundary is seen where the vectors from inside and outside of the region meets.

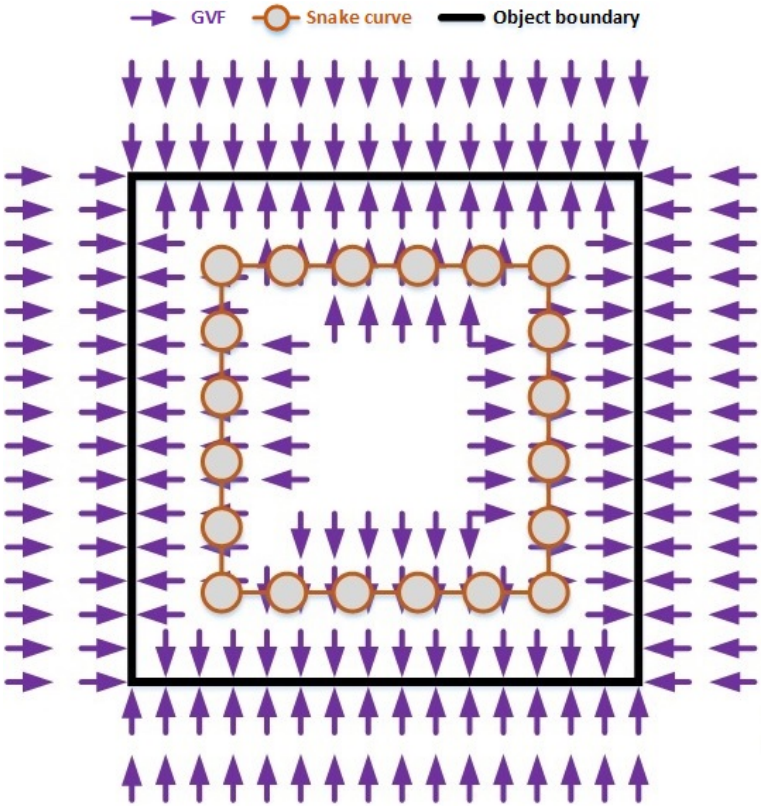

FIGURE 3.3: Gradient vector flow

3.1.4 Geometric Active Contour – Level sets

In the previous section, the PAC models were introduced that explicitly model the motion of the curve. In this section, the variations of the GAC model are presented that shows the motion of the curve implicitly by the level sets [96]. The concept of level set methods was introduced by Osher and Sethian [96] and based on the theory of curve evolution. It was later applied for the image segmentation by Caselles et al. and Madlladi et al. [97, 98]. In the GAC model, the curve is implicitly embedded as the zero level on the higher dimensional level set function ($\phi(x, y, t)$). The level set function is usually defined as a signed distance function. It is negative inside the curve and is positive outside the curve. The key advantages of the GAC over PAC is the ability of the model to automatically handle topological changes. The topological changes of the models with explicit contour is not possible due to the limits applied by the internal

energy (1^{st} and 2^{nd} order continuity). The evolution of the curve is based on the curve evolution theory and is represented as

$$\frac{\partial v}{\partial t} = FN \tag{3.13}$$

Where the parameter F controls the speed of the evolving curve and thus called as the speed function. N is the normal vector and is pointing inward. Several kinds of speed functions were proposed to achieve fast and smooth convergence of the curve. The speed of convergence can be defined by the curvature of the curve [99] and thus the equation (3.13) can be written as

$$\frac{\partial v}{\partial t} = \alpha KN \tag{3.14}$$

Where, α is the positive weight parameter and K is the curvature of the curve. In this formulation, the curve shrinks from large curvature to small curvature, and from large speed to slow speed. The differentiation of the level set function ϕ with respect to time is given as

$$\frac{\partial \phi}{\partial t} = -\nabla\phi \frac{\partial v}{\partial t} \tag{3.15}$$

Where, ∇ is the gradient and the curve v is presented as the zero level set. The normal vector on the level set is written as

$$N = -\frac{\nabla\phi}{|\nabla\phi|} \tag{3.16}$$

The basic form of the level set evolution equation is obtained by inserting the equation 3.16, 3.14 in 3.15, we get

$$\frac{\partial \phi}{\partial t} = F\,|\nabla\phi| \tag{3.17}$$

It is clear from the above equation that the level set function evolves over time (iteration). Numerical errors usually appear while the level set function evolves and thus periodic

re-initialization is recommended to achieve a stable sign distance function [100]. The limitation in curve evolution based models is the stopping criteria, since there is no intrinsic mechanism to stop this curve evolution.

3.1.5 Geodesic Active Contour – Level sets

To stop the curve at object boundaries, Caselles et. al. [30] designed a speed function F that incorporates both the image and the curvature information. The level set equation with a new speed function can be written as

$$\frac{\partial \phi}{\partial t} = g\left(K + V_o\right)\left|\nabla \phi\right| \tag{3.18}$$

Where, g is the edge indicator (3.19) that decreases the speed of the curve near the object boundaries and forces the curve to settle at high gradient values. The defined edge indicator is different from the one used in the snake model [24]. In the snake model [24], if the gradient of the image gets stronger the data term, gets smaller. However in the GAC model [30], the edge indicator function start decreasing with the increase in gradient. The modified edge indicator makes sure that the curve never diverges completely and that the data term is bounded between 0 and 1. V_o provides an additional constant speed to the convergence of the curve. The main advantage of using the speed parameter is to make sure the curve gets the object boundary, even if the curvature term in equation (3.18) approaches zero.

$$g \triangleq \frac{1}{1 + \left|\nabla\left(G_\sigma * I\right)\right|} \tag{3.19}$$

$$K = div\left(\frac{\nabla \phi}{\left|\nabla \phi\right|}\right) \tag{3.20}$$

Where, K is the curvature and $div\left(.\right)$ is the divergence operator. The equation (3.18) is effective only for strong edges, but for the weak edges the curve can easily diverge and pass over the object boundaries. A new term was added to overcome this problem (3.21), so the model can get more stability at weak edges. However, the new term makes the model more sensitive to noise.

$$\frac{\partial \phi}{\partial t} = g\left(K + V_o\right)|\nabla \phi| + \nabla \phi \nabla g \tag{3.21}$$

3.1.6 Chan-Vese Model – Level sets

The edge based active contours are very sensitive to noise and usually fail to find the object boundaries in noisy images. Researchers started thinking on how to modify the stopping criteria designing a function that doesn't depend on the gradient, but some other property of the object in an image. Chan and Vese [31] came up with a new approach that uses the region properties to stop the curve at the object boundary, with in a GAC framework.

The main idea behind the model was to compute two energies (E_1 and E_2), such as

$$\begin{cases} E_1\left(V\right) = \int_{V_{inside}} |I - C_1|^2 \, dxdy \\ E_2\left(V\right) = \int_{V_{outside}} |I - C_2|^2 \, dxdy \end{cases} \tag{3.22}$$

Where, V denotes the contour, I is the image, C_1 and C_2 are the average grayscale intensities inside and outside of the contour V, respectively and can be formulated as

$$C_1 = \frac{\int_{V_{inside}} |I| dxdy}{|V_{inside}|}, \quad C_2 = \frac{\int_{V_{outside}} |I| dxdy}{|V_{outside}|} \tag{3.23}$$

To better illustrate how these energies work, we assume a grayscale image with an object with a low intensity (0) and the background with a high intensity (255) (see Figure 3.4). Based on the energies, four conditions can be derived, as shown below

1. Contour is outside the object boundary, $E_1\left(v\right) > 0$and $E_2\left(v\right) \approx 0$
2. Contour is inside the object boundary, $E_1\left(v\right) \approx 0$and $E_2\left(v\right) > 0$
3. Contour is across the object boundary, $E_1\left(v\right) > 0$and $E_2\left(v\right) > 0$
4. Contour is located on the object boundary, $E_1\left(v\right) \approx 0$and $E_2\left(v\right) \approx 0$, (required condition)

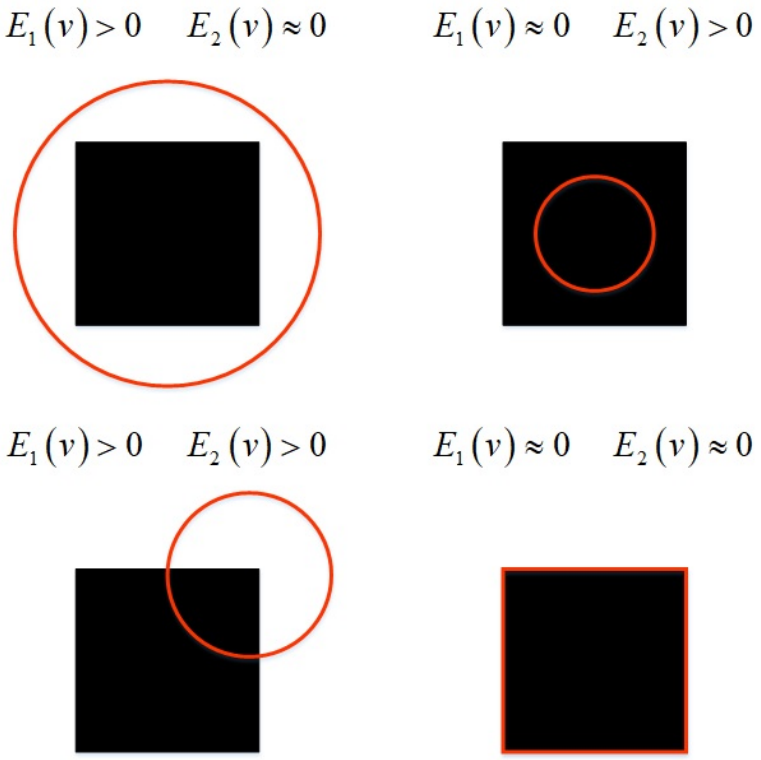

FIGURE 3.4: All possible condition of the curve

As the fourth condition is the required condition, the model $E_1 + E_2$ becomes a region based energy minimization problem. To regulate the motion of the curve, Chan-Vese [31] added the length term and the area term in the model. The total energy can be formulated as

$$E_{CV} = \mu L(V) + QA_{inside}(v) + \lambda_1 E_1(V) + \lambda_2 E_2(V) \tag{3.24}$$

Where, μ, Q, λ_1, λ_2 are the parameters that control the importance of each energy. The length term was introduced to smooth the contour by minimizing its length. The area term is used to accelerate the contour and it helps in conditions when the initial contour is far from the object boundary.

Here, we want to reformulate the total energy of the Chan-Vese model by using the level set framework. To do so, first we introduce the symbols and level set functions. The contour v is now represented by a level-set function ϕ. Regions inside the curve by Ω_{inside} and regions outside the curve by $\Omega_{outside}$ are now represented by the level set function as

$$\Omega_{inside} = \phi > 0, \quad \Omega_{outside} = \ \phi < 0 \tag{3.25}$$

Using the level set, the Heaviside function H and Dirac function δ are defined as

$$H(\phi) = \begin{cases} 1 & \phi \geq 0 \\ 0 & otherwise \end{cases} \tag{3.26}$$

$$\delta(\phi) = \frac{d[H(\phi)]}{d\phi} \tag{3.27}$$

The Heaviside function and thus the Dirac delta are not continuous. So the following approximation is adapted:

$$H_\varepsilon(\phi) = \frac{1}{2}\left(1 + \frac{2}{\pi}\arctan\left(\frac{\phi}{\varepsilon}\right)\right) \tag{3.28}$$

$$\delta_\varepsilon(\phi) = \frac{\varepsilon}{\pi(\varepsilon^2 + \phi^2)} \tag{3.29}$$

Where, ε is the small positive constant. Regions inside and outside of the zero level set in the form of Heaviside function are:

$$|\Omega_{inside}| = \int_\Omega (1 - H_\varepsilon(\phi))\, dxdy, \quad |\Omega_{outside}| = \int_\Omega (H_\varepsilon(\phi))\, dxdy \tag{3.30}$$

Each energy term in the level set function is:

$$L(\phi = 0) = \int_\Omega |\nabla H_\varepsilon(\phi)|\, dxdy = \int_\Omega \delta_\varepsilon(\phi)\, |\nabla\phi|\, dxdy \tag{3.31}$$

$$A(\phi \geq 0) = \int_\Omega H_\varepsilon(\phi)\, dxdy \tag{3.32}$$

$$E_1(\phi \geq 0) = \int_\Omega |I(x,y) - C_{in}|^2 H_\varepsilon(\phi)\, dxdy \tag{3.33}$$

$$E_2(\phi < 0) = \int_{\Omega} |I(x,y) - C_{out}|^2 (1 - H_{\varepsilon}(\phi)) \, dxdy \tag{3.34}$$

The total energy in the level set framework is written as:

$$\begin{gathered} E_{CV} = \mu \int_{\Omega} \delta_{\varepsilon}(\phi) |\nabla \phi| \, dxdy + Q \int_{\Omega} H_{\varepsilon}(\phi) \, dxdy \\ +\lambda_1 \int_{\Omega} |I - C_{in}|^2 H_{\varepsilon}(\phi) \, dxdy + \lambda_2 \int_{\Omega} |I - C_{out}|^2 (1 - H_{\varepsilon}(\phi)) \, dxdy \end{gathered} \tag{3.35}$$

The average intensities inside and outside the level set are written as:

$$C_{in} = \frac{\int_{\Omega} |I(H_{\varepsilon}(\phi))| dxdy}{\int_{\Omega} H_{\varepsilon}(\phi) dxdy}, \quad C_{out} = \frac{\int_{\Omega} |I(1 - H_{\varepsilon}(\phi))| dxdy}{\int_{\Omega} (1 - H_{\varepsilon}(\phi)) dxdy} \tag{3.36}$$

The Euler-Lagrange equation minimize the energy function E_{CV} by keeping the C_{in} and C_{out} constant, and is formulated as:

$$\frac{\partial \phi}{\partial t} = \delta(\phi) \left[\mu div \left(\frac{\nabla \phi}{|\nabla \phi|} \right) - Q - \lambda_1 (I - C_{in})^2 + \lambda_2 (I - C_{out})^2 \right] \tag{3.37}$$

Where, div(.) is the divergence operator. $\frac{\partial \phi}{\partial t}$ Shows that the level set function evolves over time (iterations). The values of C_{in} are C_{out} is updated in each iteration. The first term in equation (3.37) minimizes the length of the curve by the mean of change in curvature.

3.1.7 Localized Active Contour Model – Level sets

Medical images usually have a heterogeneous intensity profile such as with ultrasound images. In such situations, region based active contours fails to represent the real object boundaries, based on global intensity statistics. Lankon et. al. [101] had observed that in the heterogeneous images, the object has a different intensity profile than the background along the boundary of the object, if analyzed locally. Based on the above assumption, the author proposed a framework that computes the interior and the exterior regions locally along the contour (see Figure 3.5). The function that identifies the local region is:

$$B\left(x,y\right)=\begin{cases}1 & \|x-y\|<r\\ 0 & otherwise\end{cases} \tag{3.38}$$

Where, r is the radius and is manually defined by the user. At each point x, the function $B(x,y)$ is 1 if the point y stays inside the local circular region of radius r, otherwise zero. The resulting energy function using the function $B(x,y)$ is

$$E\left(\phi\right)=\int_{\Omega_x}\delta\phi(x)\int_{\Omega_y}B(x,y)F(I,\phi,x,y)dydx \tag{3.39}$$

Where, F presents a generic internal energy measure that allows the integration of several region based energy such as, the uniform modeling energy, or the mean separation energy. A regularization term was added to penalize the length of the curve, producing a smoothing effect and is controlled by the parameter λ. The framework after adding the regularization term is:

$$E\left(\phi\right)=\int_{\Omega_x}\delta\phi(x)\int_{\Omega_y}B(x,y)F(I,\phi,x,y)dydx+\lambda\int_{\Omega_x}\delta\phi(x)\left|\nabla\phi(x)\right|dx \tag{3.40}$$

After taking the first derivative with respect to ϕ, we get:

$$\frac{\partial\phi(x)}{\partial t}=\delta\phi(x)\int_{\Omega_y}B(x,y)F_{UM}(I(y),\phi(y))dy+\lambda\delta\phi(x)div\left(\frac{\nabla\phi(x)}{|\nabla\phi(x)|}\right) \tag{3.41}$$

Following the mean intensities of the interior and exterior region (3.36) of the Chan-Vese model [31], Lankon et. al. [101] proposed a localized version of the mean intensities in term of $B(x,y)$.

$$C_{in}(x)=\frac{\int_{\Omega_y}B(x,y).H\phi(y).I(y)dy}{\int_{\Omega_y}B(x,y).H(\phi)dy},\quad C_{out}(x)=\frac{\int_{\Omega_y}B(x,y).I(y).(1-H\phi(y))dy}{\int_{\Omega_y}B(x,y).(1-H\phi(y))dy} \tag{3.42}$$

The Chan-Vese model (3.35) without the regularization term and weighting parameter (λ_1 and λ_1) is referred as the uniform modeling energy, and can be written as:

$$E_{UM}=H\phi(y)(I(y)-C_{in}(x))^2+(1-H\phi(y))(I(y)-C_{out}(x))^2 \tag{3.43}$$

The derivative of the obtained energy with respect to ϕ is:

$$F_{UM} = \nabla_{\phi(y)} E_{UM} = \delta\phi(y) \left((I(y) - C_{in}(x))^2 - (I(y) - C_{out}(x))^2 \right) \tag{3.44}$$

The localized version of Lankon et. al. model (3.41) after inserting the uniform modeling energy (3.44) can be written as:

$$\begin{aligned} \frac{\partial\phi(x)}{\partial t} = \delta\phi(x) \int_{\Omega_y} B(x,y)\delta\phi(y) \left((I(y) - C_{in}(x))^2 - (I(y) - C_{out}(x))^2 \right) dy \\ +\lambda\delta\phi(x) div \left(\frac{\nabla\phi(x)}{|\nabla\phi(x)|} \right) \end{aligned} \tag{3.45}$$

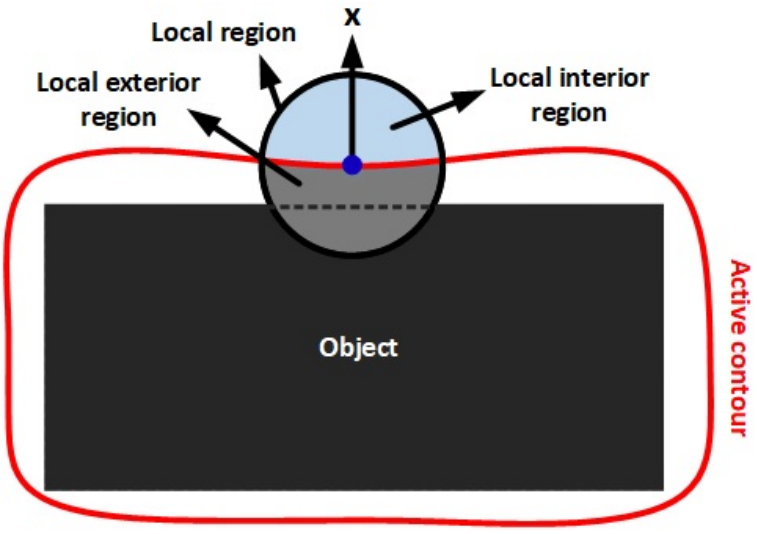

FIGURE 3.5: Localized active contour model

3.2 Echocardiography Image Segmentation

Echocardiography is an application of medical ultrasound used for analyzing anatomical structures of the heart to detect the underlying pathologies. The segmentation allows to access the structures, such as the heart chambers (e.g left atrium) to estimate the area and volume and track it throughout the cardiac cycle, in order to better understand the functioning of the heart. For instance, the obtained measurement can be used to compute the ejection fraction. In the literature, the problem of segmentation and tracking of the left ventricle and the endocardium was extensively studied [102, 103]. The ultimate goal is the assessment and early diagnosis of the heart diseases. Earlier studies focus

on 2D echocardiography and assumed that the principal component of the motion of structures are on a single 2D plane. Due to the low quality of the images, artifacts, and no reliable features, the segmentation of visual structures is very challenging. Another major problem is the over segmentation that happens due to lack of reliable features in echocardiography

Mishra et. al. [104] in 2003, proposed the use of an active contours framework, optimized by using a genetic algorithm to segment and track the endocardium in short axis view, in 2D echocardiography. The works can be realized in two steps, estimating the initial boundary of the structure, followed by the boundary refining step. The first step was accomplished by the combination of the low pass filter and the morphological operators. The second step of refining boundaries was achieved by using the active contour framework. Tracking capabilities were achieved by using the segmentation results of the previous frame as an initial boundary to segment the structures in the present frame.

Mignotte and Meunier [105] in 2001, proposed a discrete active contour framework with the multiscale optimization approach for the segmentation of endocardium in short axis view, in 2D echocardiography. The external energy was computed by using the gray level distribution obtained by using the shifted Rayleigh distribution method. The total energy of the model was minimized by using the multiscale optimization strategy [106].

Skalski et. al. [107, 108] in 2011 and 2012, proposed a region based active contour method to segment the left ventricle, in 2D echocardiography. The method can be divided into three main parts. First is to define the region of interest that was estimated by using the Hough transform followed by the thresholding to get the triangular-like region in an image. Second is the image denoising using the SRAD filter. Finally, the segmentation using the region based active contours framework.

Dietenbeck et. al. [109] in 2012, proposed a level set based model with shape constraint to segment the myocardium, in 2D echocardiography. The work was based on the assumption that the heart boundary can be represented by two hyper-quadrics, later used as a shape prior and was integrated into the model. The method was efficient to segment the region of the myocardium in four standard views, helping to analyze the structures from several angles.

Juang et. al. [110] in 2011, proposed a fully automatic graph based left ventricle segmentation method, in 3D echocardiography. The method was robust to segment the left ventricle at any time frame throughout the cardiac cycle and was valid for both the open and the close mitral vlave conditions. A minimum graph cut method was applied to segment the region of the left atrium and the left ventricle.

Chapter 4

Tracking of the Anterior Mitral Leaflet using Active Contours in Echocardiography Videos

This chapter is based on our contributions published in [111, 112]. The main focus of this chapter is to modify the framework of the classical snake model [24] to obtain a robust tracking performance of the AML, in 2D echocardiography. The classical snake model is an iterative energy minimizing process in which parametric contours evolve under the influence of image forces and the shape is controlled by an internal constraint. The framework offers automatic/semi-automatic image segmentation and motion tracking capability.

1. **M.S. Sultan**, N. Martins, E. Costa, D. Veiga, M. Ferreira, S. Mattos, and M. Coimbra, "Tracking Large Anterior Mitral Leaflet Displacements by Incorporating Optical Flow in an Active Contours Framework", in Proc. IEEE EMBC, Jeju Island, South Korea, Jul 2017, (DOI: 10.1109/EMBC.2017.8037548)

2. **M.S. Sultan**, N. Martins, D. Veiga, M.J. Ferreira, and M. Coimbra, "Tracking of the Anterior Mitral Leaflet in Echocardiographic Sequences using Active Contours", in Proc. IEEE EMBC, Orlando, USA, Aug 2016, (DOI: 10.1109/EMBC.2016.7590889)

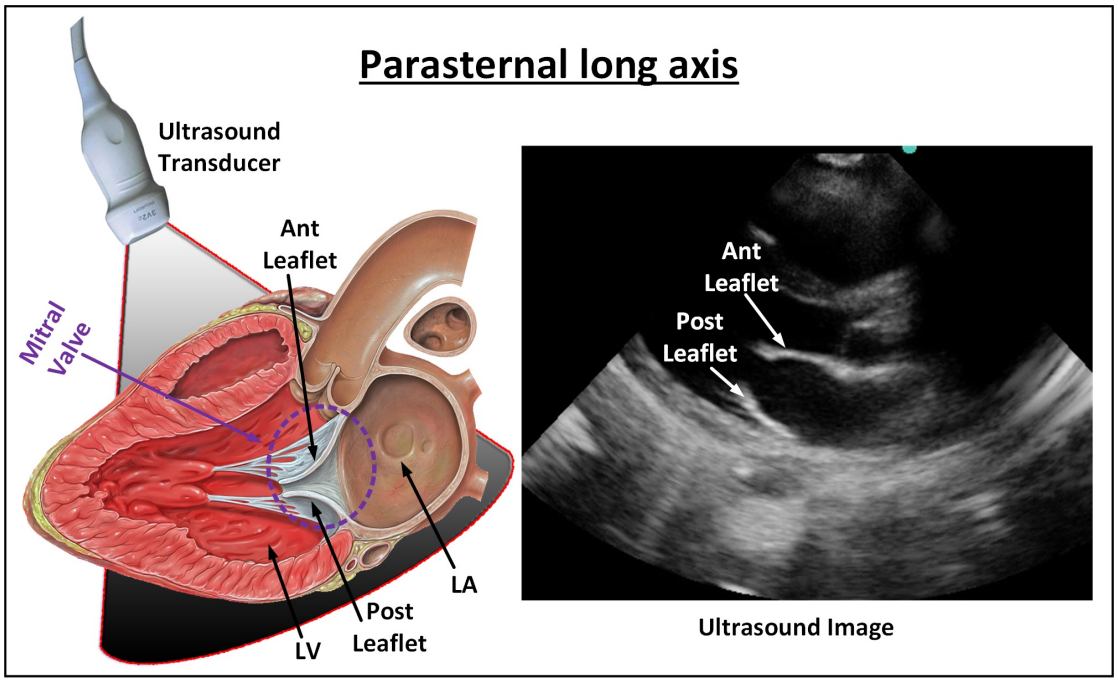

FIGURE 4.1: Parasternal long axis view of a normal mitral valve in diastole.

4.1 Incorporating Harris Energy in an Active Contour Framework

In this work, the classical snake model was modified to track a thin and elongated AML in the PLAX view of ultrasound images (see Figure 4.1). Open ended contours were used and the external energy of the model was adapted in a way that increases the range of the contour and encourages the end point of the is contour to stay on the tip of the AML.

The proposed method will focus on the tracking of the leaflet and so it assumes perfect segmentation of the AML in the first frame. In the experiments as well as in its potential practical applications, this is achieved by manual segmentation, in order to avoid the errors of automatic segmentation which are beyond the scope of this specific contribution. Our modified snake model is then responsible to track these points during the whole cardiac cycle. These modifications are now explained in detail.

4.1.1 Internal Energy

As previously explained, the internal energy is responsible to regulate the contour by imposing the elasticity and stiffness that are the first and second derivative, respectively. The weights, α and β control the relative influence of each term (3.1).

Elasticity motivates the shrinking of the contour length in each iteration and given that we are using a perfect initial segmentation and that the physical length of the AML does not change in the PLAX view, this measure of internal energy was not adequate for our problem. Only stiffness is used, that controls the bending energy of the snake. The weight β remains constant for all the contour points. A free boundary condition was used that allows the end points of the contour to move freely on the image plane to get minimum energy, promoting 'line' contours instead of 'circles'. However, it was bounded to remain closer to its neighbour contour point. The above boundary condition leads to N linear equations that provide us a convenient way to write in a matrix form (4.1). This configuration allows us to solve all the points simultaneously.

$$x^{t+1} = (M + \gamma I)^{-1} x^t, y^{t+1} = (M + \gamma I)^{-1} y^t$$

$$\underbrace{\begin{bmatrix} \hat{r} & q & p & & & & \\ \hat{q} & r & q & p & & & \\ p & q & r & q & p & & \\ & \ddots & \ddots & \ddots & & & \\ & & p & q & r & q & p \\ & & & p & q & r & \hat{q} \\ & & & & p & q & \hat{r} \end{bmatrix}}_{M} \begin{cases} p = \beta \\ q = -4\beta \\ r = 6\beta \\ \hat{r} = 3\beta \\ \hat{q} = -3\beta \end{cases} \tag{4.1}$$

Whereas, γ control the step size and is always positive and I is an identity matrix.

4.1.2 External Energy

The external energy of the classical snake model consists of image and constraint energies (3.1). The image energy is the combination of three energy functions (3.2). The first

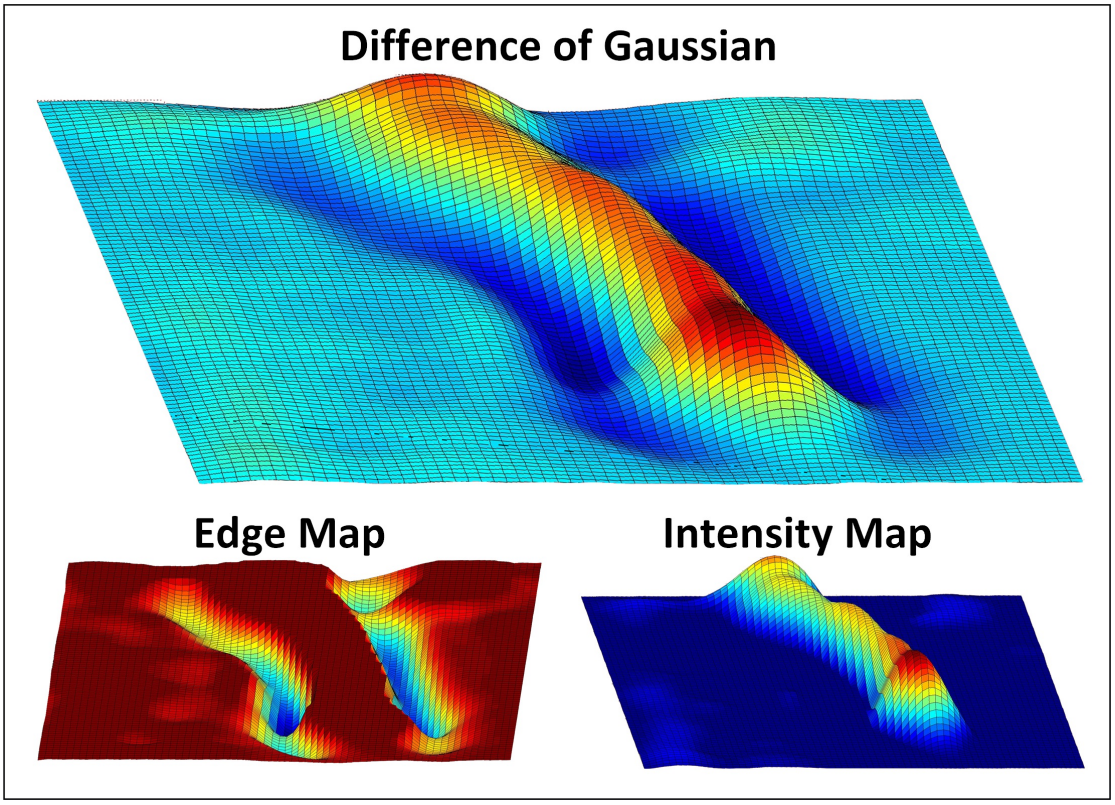

FIGURE 4.2: Surf plots: DoG of AML region of grayscale image. Positive valued pixels (intensity map), negative valued pixels (edge map).

term is the line energy that forces the snake towards light/dark regions, the second term is the edge energy that aligns the points at high image gradients, and finally term energy uses the curvature of level lines to find terminations. The respective weights assigned to each of the energy terms $w_{line}, w_{edge}, w_{term}$.

In this work, the external image energy of the snake was modified so that it best fits with our particular application. Instead of using a simple intensity image and the edge map, we use a Difference of Gaussians (DoG), which is a simplified way to approximate the Laplacian of Gaussian. DoG was found very effective in ignoring low frequency details from ultrasound images [113]. DoG was divided into two main parts: pixels with positive values were characterized as high-intensity regions and negative valued pixels characterized as edges (4.2) (see Figure 4.2). Obtained edges are wider which increases the capture range, and intensity regions are enhanced and well localized, that encourages contour points to be aligned exactly in the middle of the AML.

$$\begin{aligned} E_{DoG\_line} &= I \times (G_{\sigma_1} - G_{\sigma_2}) \quad DoG \geq 0 \\ E_{DoG\_edge} &= I \times (G_{\sigma_1} - G_{\sigma_2}) \quad DoG < 0 \end{aligned} \tag{4.2}$$

In the above equation, the image is convolved with the difference of Gaussian kernels of width σ_1 and σ_2 whereas, $\sigma_2 > \sigma_1$. In this work, we used a Gaussian filter of size 20 with sigmas 8 and 10, obtained empirically in pilot tests.

To obtain better tracking performance, end points of the contour are encouraged to continuously follow the tip of the AML. To achieve this, cornerness energy was used, instead of line or edge energy, that encourages end points to stay on the AML tip. Several key methods such as edge-related corner, topology corner and auto-correlation were tested for our specific images. Kitchen et al. [114] proposed an edge-related cornerness measure that defines the change in gradient direction and magnitude along the edge map. This algorithm is very sensitive to noise, unstable and not well localized at blurred edges. Deriche et al [115] proposed a topology related scale-space cornerness measure. His method intelligently merges the useful property of the Laplacian (zero at the corners) and Beaudet's measure (positive maximum at corner) [116]. The method was found very unstable in noisy images and extremely slow.

The methods based on auto-correlation were found quite satisfactory, thus used in this work. Moravec [117] had explored that the maximum intensity variation in various directions within the local window represents a corner. However, he was looking for a distinct region, not specifically the corners. Later on, Harris et al. [118] has improved his approach by proposing an analytic expansion of the shift (4.3).

$$S = \sum_x \sum_y \underbrace{w\,(x,y)}_{window} \left(\underbrace{I\,(x+u, y+v)}_{shifted\_intensity} - \underbrace{I\,(x,y)}_{intensity} \right)^2 \tag{4.3}$$

The window function can be a Gaussian or rectangle at position x, y. (u, v) shows a small displacement in all directions that estimate the intensity difference. After applying a Taylor series expansion and arithmetic operations, we get the covariance matrix A (4.4).

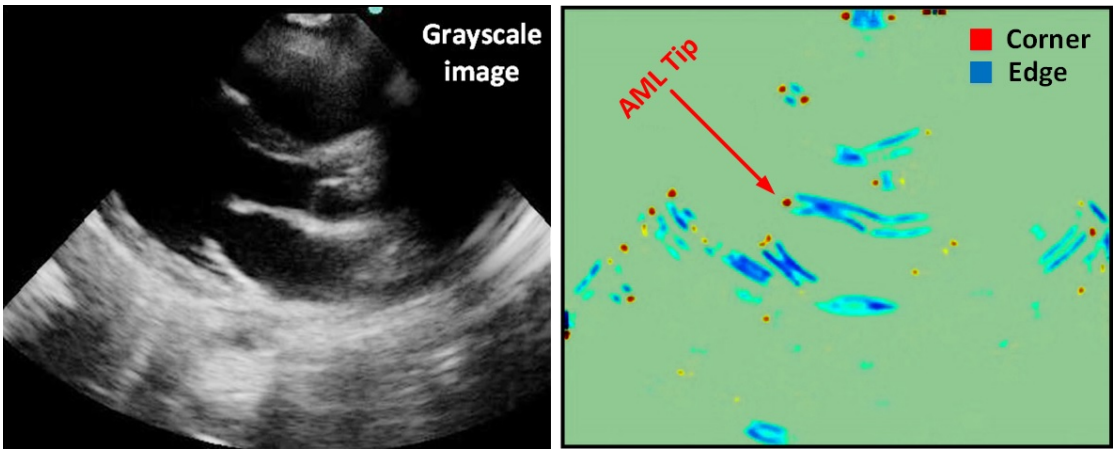

FIGURE 4.3: Harris Cornerness measure (E_{Harris}), shows corners in Red and edges in Blue

$$A = \sum_x \sum_y w(x,y) \begin{bmatrix} I_x^2 & I_x I_y \\ I_x I_y & I_y^2 \end{bmatrix} \tag{4.4}$$

In this work, E_{DoG_line} image was convolved with filter $[-8\ 0\ 8]$ to get the derivatives. The derivatives are then smoothed with a Gaussian filter of size 10 and sigma 3. Finally, the cornerness measure was evaluated using (4.5) (see Figure 4.3)

$$E_{Harris} = det(A) - k(trace(A))^2 \tag{4.5}$$

The modified external energy of the snake was (4.6)

$$\begin{aligned} E_{ext} = E_{image} = w_{harris} E_{harris} - w_{DoG\_line} E_{DoG\_line} \\ + w_{DoG\_edge} E_{DoG\_edge} \end{aligned} \tag{4.6}$$

This external energy affects the snake points in a very particular way. The modified edge and intensity snake energy provide an attraction force that attracts all the points except the ones close to the AML tip (4.7).

$$\begin{aligned} x_S^{t+1} &= \gamma x_S^t + \Big((f_x)_{DoG\_line} + (f_x)_{DoG\_edge} \Big) \\ y_S^{t+1} &= \gamma y_S^t + \Big((f_y)_{DoG\_line} + (f_y)_{DoG\_edge} \Big) \end{aligned} \tag{4.7}$$

Whereas, γ is the step size, f_x and f_y are the derivatives with respect to x and y. The first two points of the contour are encourages to move towards the tip of AML (4.8).

$$\begin{aligned} x_U^{t+1} &= \gamma x_U^t + (f_x)_{Harris} \\ y_U^{t+1} &= \gamma y_U^t + (f_y)_{Harris} \end{aligned} \tag{4.8}$$

4.1.3 Materials

In one of the activities of Real Hospital Português, in Recife, Brazil, a dataset of ultrasound mitral valve videos has been collected for the purposes of screening acute rheumatic fever in children. The data was collected using a M-Turbo model by SonoSite ultrasound system, with C11x transducer (5-8 MHz). Nine of these exams were fully annotated (manual segmentation of all frames) using support software and were used to test the novel algorithm proposed in this work. These nine videos include a total of 1137 frames with dimensions of $[351 \times 441]$.

4.1.4 Experimental Methodology

The performance of the proposed tracking method was evaluated by computing the Modified Hausdorff Distance (MHD) [119], that actually computes the distance between two curves. The evaluation matrix consists of two parts. First, accessing the performance of the AML tracking by comparing the manual annotation (obtained by the doctors) to the automatic annotation (obtained by the proposed method) using MHD. Second, it allows the comparison to other studies, like in this work with the classical snake model [24].

4.1.5 Tracking results

The proposed algorithm used the manual annotation as its contour initialization for the first frame of every video sequence. The algorithm managed to handle small to medium frame to frame displacements. However, the algorithm fails to track if the displacement was very high (about 33 pixels). The MHD [119] error between the set of manually annotated points (GS) and snake control points (SEG) used the following formula (4.9).

$$\begin{cases} d_{GS \to SEG} = min\{GS, SEG\} \\ d_{SEG \to GS} = min\{SEG, GS\} \\ A = avg\{d_{GS \to SEG}\} \\ B = avg\{d_{SEG \to GS}\} \end{cases} \tag{4.9}$$

$$Error = max(A, B)$$

The algorithm was also compared with the classical snake approach [24] exhibiting superior performance (Table. 4.1).

TABLE 4.1: Tracking error (Pixel)

Video No.	***No. Of Frames***	Our Approach	Kass Approach [24]
		Avg / STD *Error (PX)*	***Avg / STD*** *Error (PX)*
1	131	5.32 / 1.89	6.08 / 3.26
2	360	4.6 / 1.8	5.7 / 1.85
3	66	5.22 / 2.4	7.84 / 2.47
4	131	4.33 / 1.81	6.7 / 1.67
5	66	5.6 / 4.06	7.66 / 3.95
6	66	5.74 / 1.56	5.15 / 2.19
7	120	4.95 / 1.96	5.61 / 1.66
8	66	4.97 / 2.27	6.1 / 1.94
9	131	3.67 / 1.72	5.56 / 2.45
Total	**1137**	**4.93 / 2.16**	**6.26 / 2.38**

Although the used dataset was limited to nine videos, all results showed that snake points converged and were tracked accurately, with very small differences to the manual annotation.

4.1.6 Discussion

The classical snake model was successfully modified for better performance in the specific scenario of mitral valve tracking in ultrasound images. Exploiting specific characteristics of the scenario led to a reformulation of both the internal (open contours, removal of elasticity) and external energy (DoG energy, cornerness energy for the tip of the valve) of classical snakes. This work provides the base to better understand the abilities and the limitations of the classical snake model for the problem of AML tracking in 2D echocardiography. It paves the way to address the limitations of the proposed method, more specifically the problem of tracking failure, a step towards the robust tracking approach.

4.2 Incorporating Optical Flow Energy in an Active Contour Framework

In this work, our main objective was to improve the tracking performance by addressing situations with large displacements. As contributions, the external energy of our previous method was modified to incorporate optical flow energy, promoting solutions associated with the large motion exhibited by the mitral valve leaflet. This work builds upon our previous research [111] that frequently encountered failures in such situations.

The focus of this work was to improve the tracking capabilities of our previous algorithm, discussed in last section. We assume perfect segmentation in the very first frame, which is then tracked throughout the cardiac cycle. Since this is an extension of our previous work, the integration of the optical flow in classical snake model is here explained in more detail.

4.2.1 Internal energy

We used the open ended contours obtained through the free boundary condition. The open ended contours results into lines that segment and track the AML in a more natural way. The end points are free to move on the image plane to get an energy minimum and are constrained to stay close to their neighbors (4.1). The elasticity and stiffness are controlled in the same way as in the classical snake model [24].

4.2.2 External Energy

The new external energy can be divided into two main parts, the image and the motion energy (4.10).

$$E_{ext.} = E_{image} + E_{motion} \tag{4.10}$$

The image energy is the same, as used in our previous work (4.6), consisting of three terms, the line and the edge energy obtained through the Difference of Gaussians, and the Harris corner energy (4.4). The Harris corner energy encourages the endpoint of the contour to continuously follow the tip of the AML.

The motion energy quantifies the image displacement energy for overcoming the limitation (tracking failure in large motion) of our previous work [111]. Optical flow was integrated in the external energy of the classical snake model as a dynamic energy (4.11).

$$E_{motion} = w_{optical\_flow} E_{optical\_flow} \tag{4.11}$$

Optical flow methods, which attempt to quantify the motion of brightness patterns in a sequence of images, can be divided into local methods, such as Lucas-Kanade [120, 121], and global methods, such as Horn-Schunck [122]. We selected the Lucas-Kanade approach, considered by literature as still the most interesting cost-benefit optical flow method [123].

In this work, we used a coarse-to-fine approach to Lucas-Kanade to efficiently handle both large and small motions. This consists on creating multiple copies of the same image with different resolutions. In each level, the resolution was reduced 1/4 of the size of the previous level (4.12).

$$g_L(x,y) = \sum_{m=-2}^{2}\sum_{n=-2}^{2} w(m,n)\, g_{L-1}(2x+m, 2y+n) \tag{4.12}$$

The 2D mask w of size 5×5 was convolved with the image g at level $L-1$, to obtain the low resolution image at level L. The pre-filtering step in pyramid construction plays a vital role for the true optical flow estimation [124]. Based on this work, a Gaussian filter with the standard deviation of 1.3 was used to smooth the image for all the levels instead of smoothing only the initial image. The image was downsampled using the nearest neighbor approach with a scale factor of 0.5.

The pipeline to obtaining the true optical flow in this pyramid approach (see Figure 4.4) was as follows: First, the optical flow was computed in the highest level ($L3$). Since the motion is reduced in the highest level ($L3$) due to low resolution, the estimated optical flow is easier to calculate given the presence of more image structures. The obtained flow in the previous level ($L3$) was used as an initial guess to obtain the flow in the next level ($L2$). This level ($L2$) have double the resolution of the last level ($L3$). Thus, we used the bilinear interpolation to obtain the optical flow in that level.

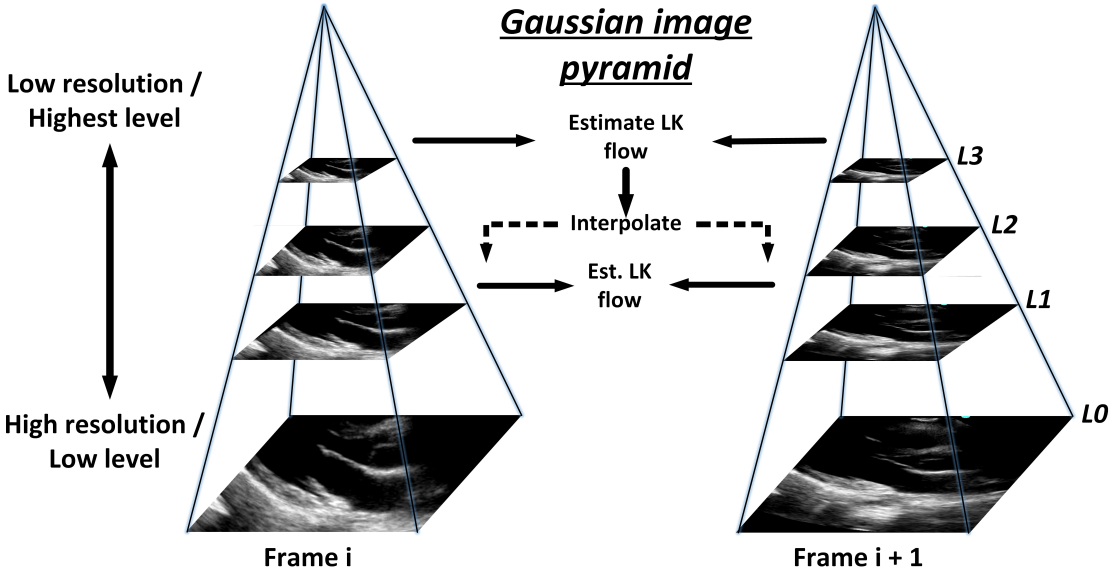

FIGURE 4.4: Lucas-Kanade [120, 121] optical flow with pyramids (Coarse-to-fine)

At this point, we have the motion vectors for each pixel that give us the displacement in relation to the previous frame (see Figure 4.5). Our objective was to integrate this

information (displacement and direction) in the classical snake model. We added the motion vectors as the displacement force in an external energy that encourages the contour points towards areas with large motion, as is the case of the AML.

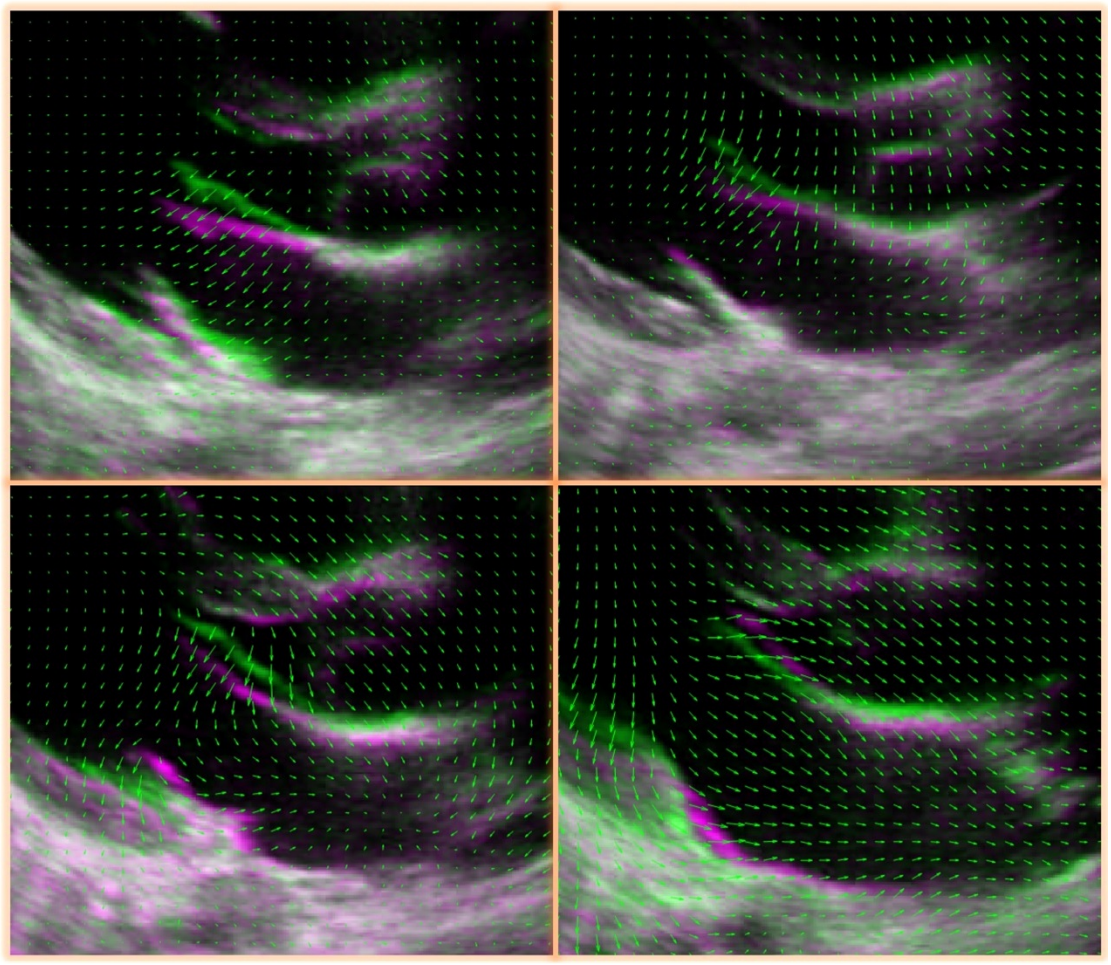

FIGURE 4.5: Motion vectors of the optical flow (Lucas-Kanade). Last frame: Green, Present frame: Magenta

The iterative form of the modified classical snake model is shown (4.13, 4.14)

$$\nabla E_{ext.} = \begin{bmatrix} \frac{\partial E_{image}}{\partial x} \\ \frac{\partial E_{image}}{\partial y} \end{bmatrix} + \begin{bmatrix} \frac{\partial E_{motion}}{\partial u} \\ \frac{\partial E_{motion}}{\partial v} \end{bmatrix} = \begin{bmatrix} f_x \\ f_y \end{bmatrix} + \begin{bmatrix} f_u \\ f_v \end{bmatrix} \tag{4.13}$$

$$\begin{aligned} X_t = \quad & (A+\gamma I)^{-1}(\gamma X_{t-1} - f_x(X_{t-1}, Y_{t-1}) \\ & + f_u(X_{t-1}, Y_{t-1}) \\ Y_t = \quad & (A+\gamma I)^{-1}(\gamma Y_{t-1} - f_y(X_{t-1}, Y_{t-1}) \\ & + f_v(X_{t-1}, Y_{t-1}) \end{aligned} \tag{4.14}$$

Whereas, I is the identity matrix, γ is the step size and A is coefficient matrix. The first part of the equation $(A+\gamma I)^{-1}$ imposes the internal constraints and the other part attracts the contour toward the image energy.

4.2.3 Materials

In one of the activities of Real Hospital Português, in Recife, Brazil, a dataset of ultrasound mitral valve videos (PLAX view) has been collected for the purposes of screening acute rheumatic fever in children. The data was collected using a M-Turbo model by SonoSite ultrasound system, with $C11x$ transducer (5-8 MHz). Nine of these exams were fully annotated (manual segmentation of all frames) using support software and were used to test the novel algorithm proposed in this work. These nine videos include a total of 1137 frames with dimensions of $[351 \times 441]$.

4.2.4 Experimental Methodology

The performance of the proposed tracking method was evaluated by computing the Modified Hausdorff Distance (MHD) [119], that computes the distance between two curves. The evaluation matrix consist of two parts. First, accessing the performance of the AML tracking by comparing the manual annotation (obtained by doctors) to the automatic annotation (obtained by the proposed method) using MHD. Second, it allows the comparison to other studies, like in this work with our previous contribution [111], to evaluate the degree of improvement.

4.2.5 Tracking Results

The tracking starts with a manual initialization by inserting 6 points on the AML, in the first frame of each video. To evaluate the performance, results of the reference approach [111] and the proposed approach are compared with the ground truth (doctor's annotation). The MHD [119] error was computed for the ground truth and the automatic segmentation. Table 4.2 shows the mean, median and the standard deviation of the MHD error in each video, for both the reference and our approach. The results are computed for the most difficult situation, when the AML shows large displacement, for example, at first opening of the AML and in the diastole phase. The results shows improvement in each video, with the overall mean, median and standard deviation of 2, 4.5 and 4.2 pixels, respectively.

TABLE 4.2: Tracking results (in pixels)

	Our Approach	**Ref. Approach [111]**
Video No.	STD / Mean / Median	STD / Mean / Median
1	2.2 / 3.2 / 2.5	3.2 / 6.0 / 5.8
2	2.5 / 6.0 / 5.5	4.0 / 9.9 / 11.3
3	1.7 / 4.2 / 3.9	2.5 / 5.8 / 5.3
4	2.2 / 4.9 / 4.5	1.4 / 5.6 / 5.1
5	1.6 / 4.5 / 4.6	2.7 / 6.4 / 5.7
6	3.4 / 5.3 / 4.9	6.2 / 7.9 / 5.3
7	0.7 / 4.7 / 4.6	1.1 / 5.1 / 4.7
8	0.9 / 3.5 / 3.6	0.9 / 4.8 / 4.8
9	3.2 / 4.5 / 3.7	3.5 / 5.4 / 4.2
Total	**2.0 / 4.5 / 4.2**	**2.8 / 6.3 / 5.8**

In order to visually inspect these results, we plotted in the same image the reference approach (green) [111], our approach (blue) and the ground truth (red) (see Figure 4.6). Figure 4.6 clearly shows the limitation of the reference approach. In the case of large leaflet motion there is no force near the contour points that makes the curve evolve towards true boundaries. However, in our proposed approach the optical flow (motion vector) can guide the contour towards true boundaries. One can see that the results of our approach was approximately overlapping the ground truth, reinforcing the number presented in Table 4.2.

Better tracking performance was achieved but at the cost of computational complexity. Our previous approach (discussed in last section 4.1) consumes about 0.58 second/frame

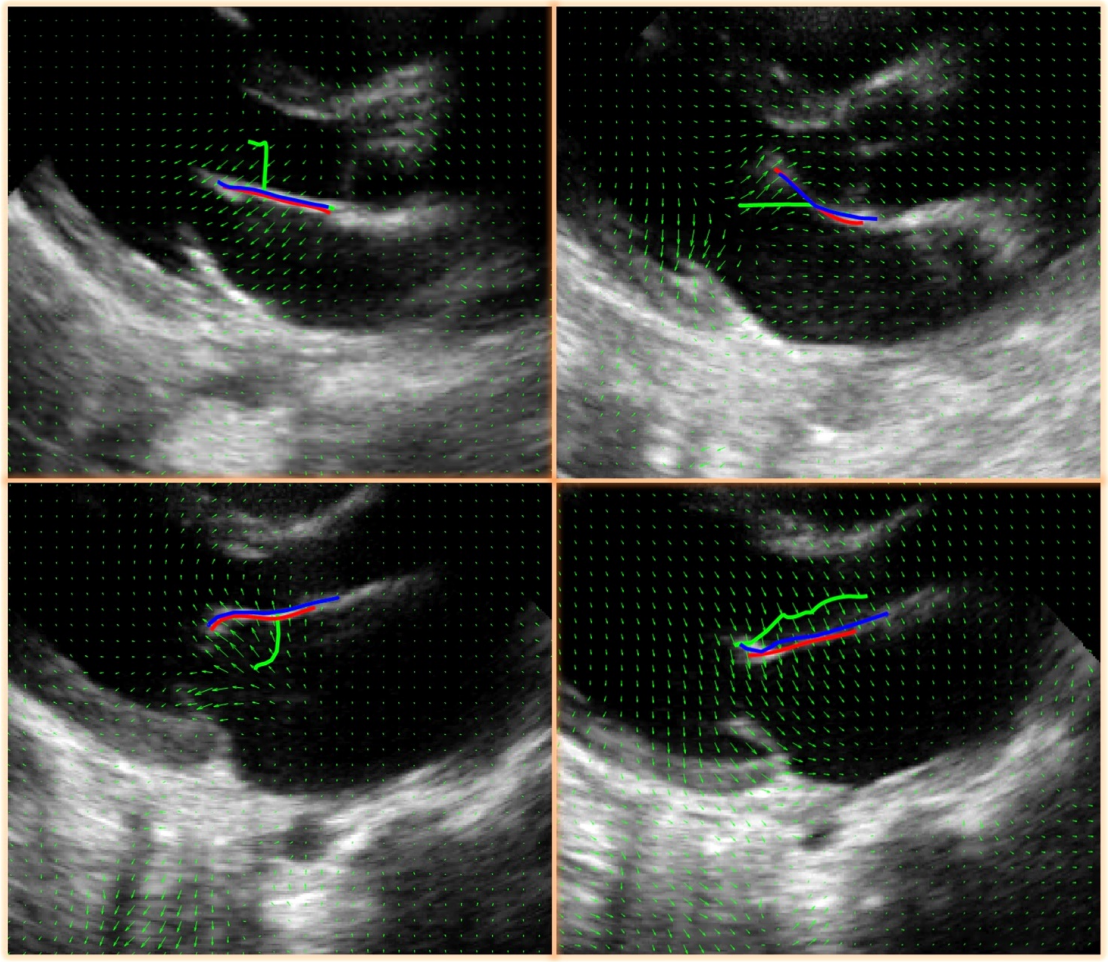

FIGURE 4.6: Tracking of the AML. Red: Ground truth, Green: Ref. approach, Blue: Our approach, Green arrows: Motion vectors

to automatically delineate the AML. However, our approach takes about 14.07 second/frame, on a desktop computer (Quard-Core AMD Phenom II processor, 3.2 GHZ, 8 GB RAM) in window 10 environment.

4.2.6 Discussion

Experiments showed that the proposed algorithm was more robust than the previous approach [111], exhibiting improved tracking capability (less failures). The AML shows large displacements and thus classical snake models are not adequate for tracking in such situations, since there is no force that can attract the contour towards the desired location. To overcome this problem, we integrated the optical flow as an external energy in the classical snake framework. The proposed framework considers the movement of tissues in the successive frames for improved tracking performance.

As still unaddressed issues, the proposed algorithm still needs a failure recovery mechanism, and was computationally expensive (due to integration of the optical flow) for portable systems, unless some sort of cloud-based processing is used.

Chapter 5

Real-Time Anterior Mitral Leaflet Tracking using Morphological Operators and Active Contours

This chapter is based on our contribution published in [125, 126]. The objective of this work was to obtain robust and real-time tracking of the AML in ultrasound videos. Mathematical morphology was previously used to segment the left ventricle [127], myocardium, ischemic viable and non-viable in echocardiography [128]. Our key contribution in this work was the novel use of the combination of the morphological operators and active contours to address robust AML tracking in frames with large displacement.

1. **M.S. Sultan**, N. Martins, E. Costa, D. Veiga, M. Ferreira, S. Mattos, and M. Coimbra, "Real-time Anterior Mitral Leaflet Tracking using Morphological Operators and Active Contours", in Proc. Int. Joint Conf. on Biomedical Engineering Systems and Technologies, BIOSTEC, Porto, Portugal, Feb 2017, (DOI: 10.5220/0006244700390046)

2. **M.S. Sultan**, N. Martins, E. Costa, D. Veiga, M.J. Ferreira, S. Mattos, M. Coimbra, "Tracking Anterior Mitral Leaflet in Echocardiographic videos using Morphological Operators and Active Contours", Communications in Computer and Information Science, Biomedical Engineering Systems and Technologies, 881, Chapter 9, (DOI:10.1007/978-3-319-94806-5_9).

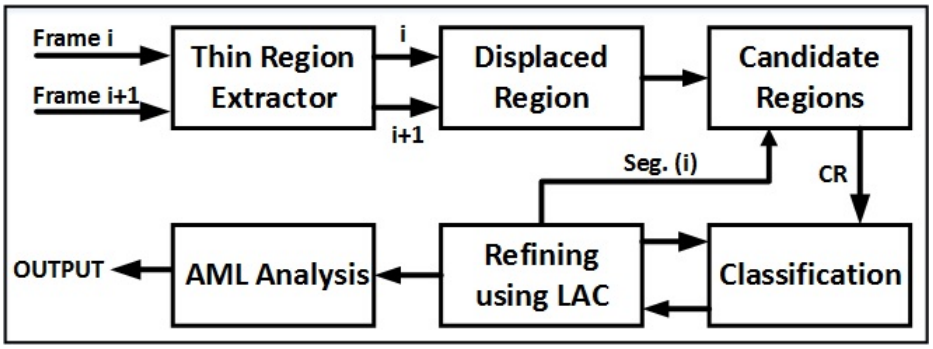

FIGURE 5.1: AML tracking pipeline

In the first step, an echocardiography video was read, followed by contrast stretching to normalize the illumination of the image. In this work, we assumed that the perfect segmentation (manual) of the first frame was provided a priori. In each step, two successive frames are iteratively selected. Since AML is a thin region that shows fast motion, the thin regions of the successive images are extracted followed by the regions with large displacement, using basic mathematical morphology filtering. These regions are subsequently merged with the segmentation result of the preceding frame and filtered in the candidate region module. Obtained regions are classified by taking into account their shapes and geometrical properties. The obtained boundaries of the AML with morphological operators are not well localized. Therefore, a localized active contour model was used to refine the obtained boundaries. After having the segmentation results, we proceed to the post processing step of AML analysis. A summary of the proposed processing pipeline is depicted in Figure 5.1, and each step will now be discussed in detail.

5.1 Thin Region Extractor

In this stage, two consecutive frames were extracted iteratively until the whole cardiac cycle was covered. The basic mathematical morphological operations were used that requires, the input image and the structuring element of suitable size and shape. These morphological operations can be used for both binary and grayscale images. For the resolution of the videos used in this experimental work, the maximum recorded thickness of the AML was 24 pixels. Following this, we used the grayscale images with the disk shape structuring element of width 24 pixels, to extract the potential regions.

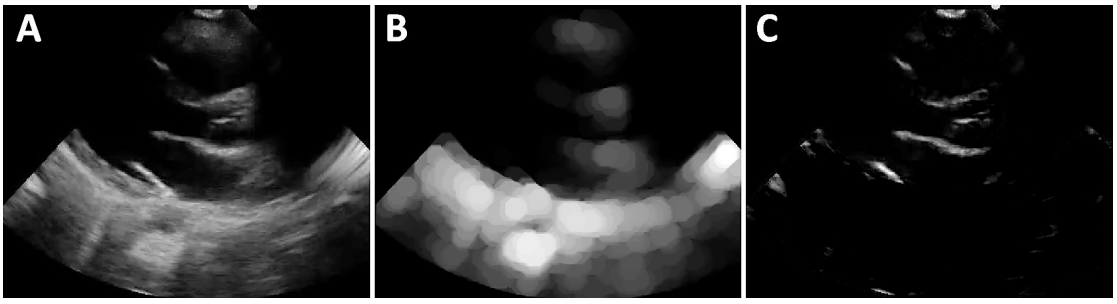

FIGURE 5.2: A) Grayscale image B) Morphological opening C) Top-hat transform

Finally, The thin AML region (see Figure 5.2C) was extracted by taking the difference between the grayscale input image (see Figure 5.2A) and the grayscale opened image (see Figure 5.2B) with the flat disk shape structuring element of 24 pixel diameter.

5.2 Displaced Region

Based on the analysis of the AML in the PLAX view, the thin AML region shows a very large displacement in successive frames, when compared to other regions in an image. Other regions such as the septum or the inferior wall (see Figure 5.3) do not show a significant displacement in successive frames and thus the regions are overlapped. This prior information is meaningful to overcome the problem of tracking in frames with large AML displacement.

The focus of this module is to extract the region that showed the largest displacement from frame t-1 to frame t. This can simply be achieved by taking the difference between successive frames followed by selecting only the positive intensity values (see figure 5.4), (5.1). A threshold was then applied to get the binary image.

An optimal global threshold was automatically obtained by analyzing the intensity histogram using the Otsu's method [129]. The method selects the lowest point between the two classes on the histogram (between black and white pixels), minimizing the intraclass variance. Since the Ostu's method is very sensitive in noisy images, we have selected the good segmentation cases and average out their threshold. The obtained average threshold was $T_{avg}^{DR} = 0.07$ and was relatively insensitive to noise and thus used in this work.

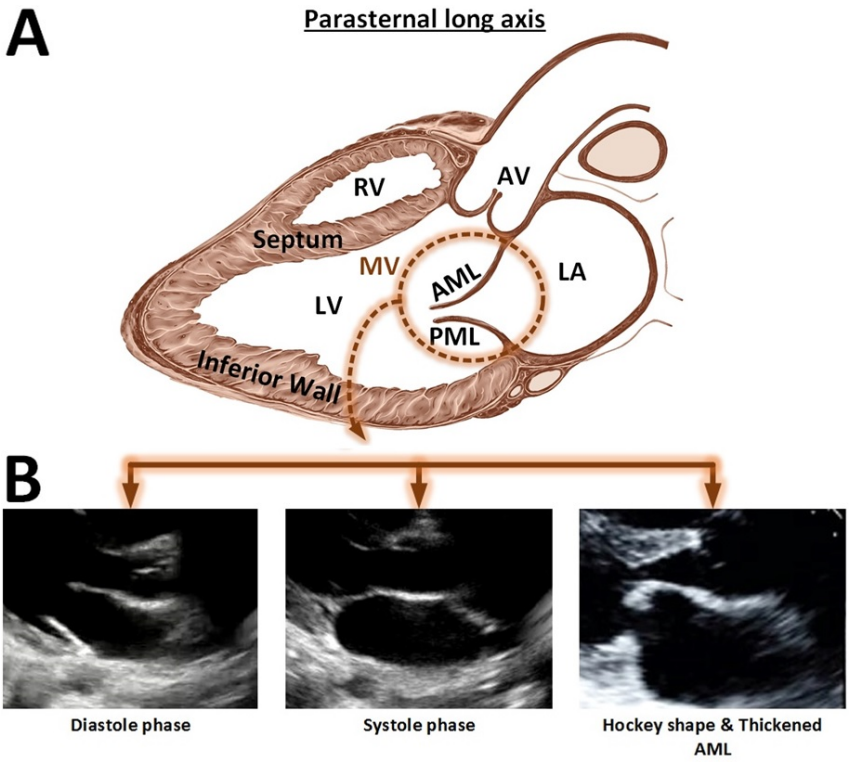

FIGURE 5.3: Parasternal long axis view (A): showing Mitral valve (MV), Anterior Mitral Leaflet (AML), Posterior Mitral Leaflet (PML) and other structures. (B): Shows the MV in Diastole/Systole phase, the thickened and hockey shape leaflet.

$$Disp^{t}_{gray} = [I_t(x,y) - I_{t-1}(x,y)] \quad Disp^{t}_{gray} < 0 \tag{5.1}$$

5.3 Candidate Image

In this module, the segmentation result of AML obtained at time t-1 was summed up with the results of the displaced region module to get the candidate image (See Figure 5.1). The candidate image was then filtered in two steps. First is to remove the regions in the candidate image that belongs to the blood pool. The original grayscale image (at time t) was binarized by using the threshold, automatically obtained by the Otsu's method [129]. The average threshold was around $T^{CI}_{avg} = 0.13$. Next, we compute the overlap between the binarized image and the candidate image. We keep the overlapped regions and discard other, as they belong to the blood pool. Second, the small discontinuities between the regions (with a distance of 2 pixels or less) were merged by a

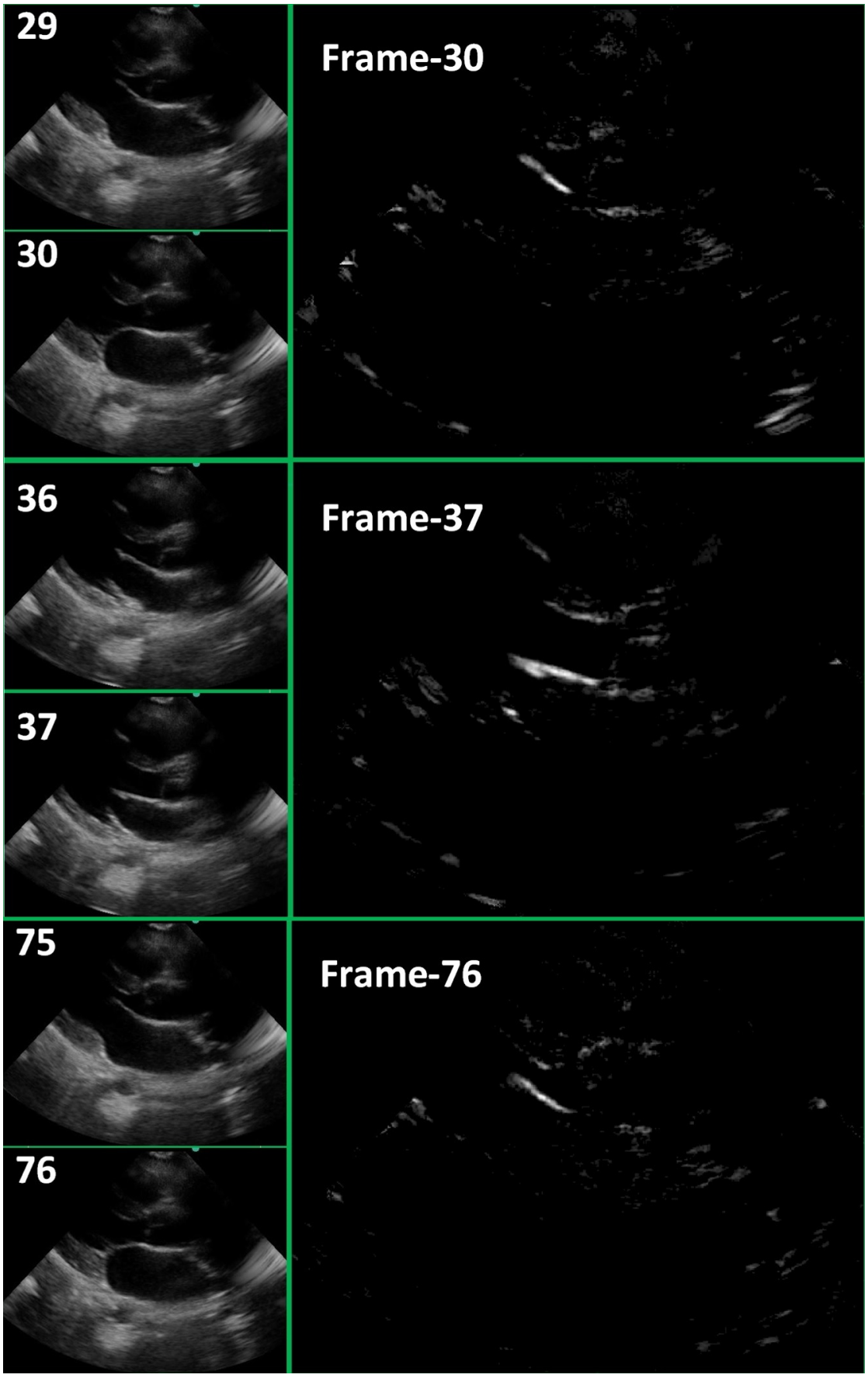

FIGURE 5.4: Regions with high displacement at four different times (frames)

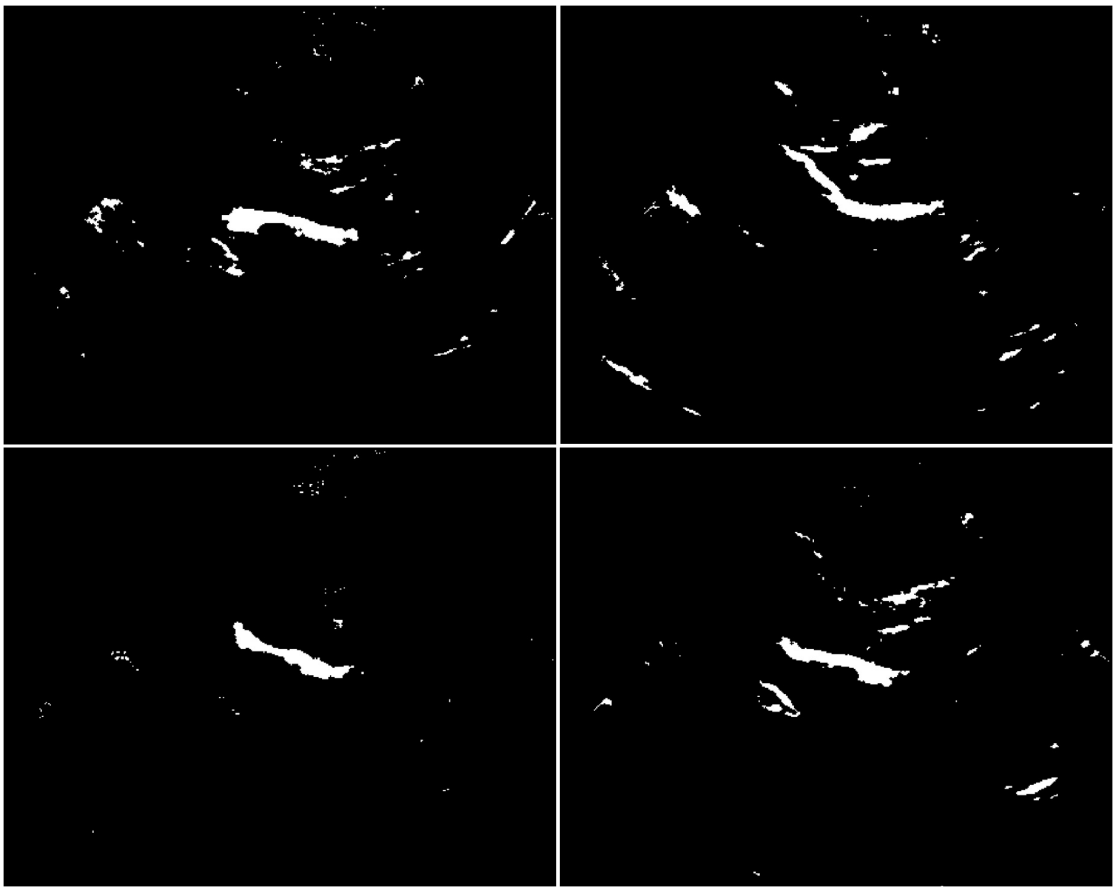

FIGURE 5.5: Candidate image for final AML classification

morphological closing using a disk shape structuring element with a radius of 2. The obtained results are shown in Figure 5.5.

5.4 Region Classification

The region classification module is based on the assumption that the shape of the AML doesn't change a lot in successive frames. Therefore, the basic morphological features, such as area, centroid, minor axis length, and major axis length, do not typically change significantly. These features provide the structural and locality information to assign the probability to a region being the AML or an outlier.

Following above assumption, the segmentation obtained in the last frame (at time t-1) was used as a reference for the upcoming frames (at time t), and the manual segmentation of the first frame was considered optimal and was used to initialize the algorithm.

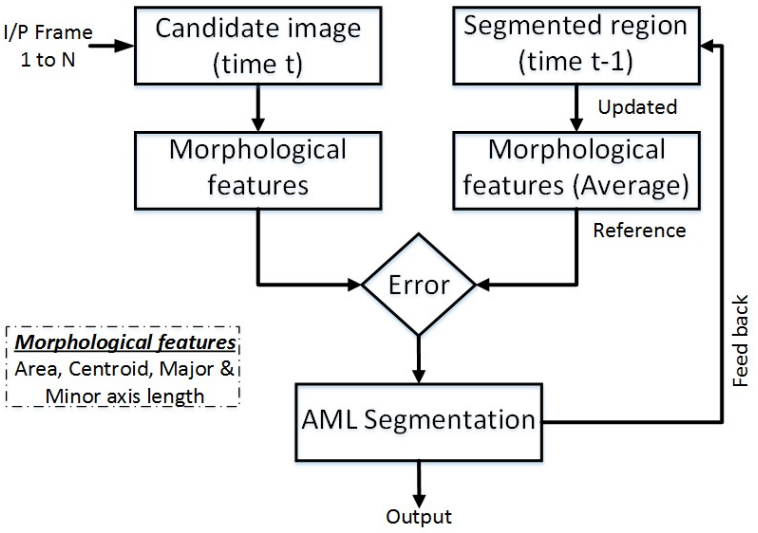

FIGURE 5.6: Classification scheme

An error matrix was designed that search for the best match in the candidate image, obtained at time t. The matrix quantifies the change in the morphological features at time t, reference to the last frame at time t-1. The matrix consists of four vectors that computes the change, area error: computes the change in an area, centroid error: computes the change in location, major/minor axis length error: compute the change in length and width.

Finally, the region with the minimum overall error shows the best match and was classified as AML and other as outliers. After processing each frame, the reference features were automatically updated with the average, by using the feedback channel (see Figure 5.6).

5.5 Refining Using Active Contours

The active contour framework has been extensively used for the purpose of image segmentation and tracking [130]. The most popular Geometric Active Contours (GAC) are the edge based [30], region based [31], and hybrid based (uses both edge and region properties) [131] (see section 3.1.4).

The edge based active contours [30] use the image gradient information (edges) to attract the contour towards the desired boundary. They work reasonably well in images with heterogeneous regions (see Figure 5.7). However, they are very sensitive to the initial

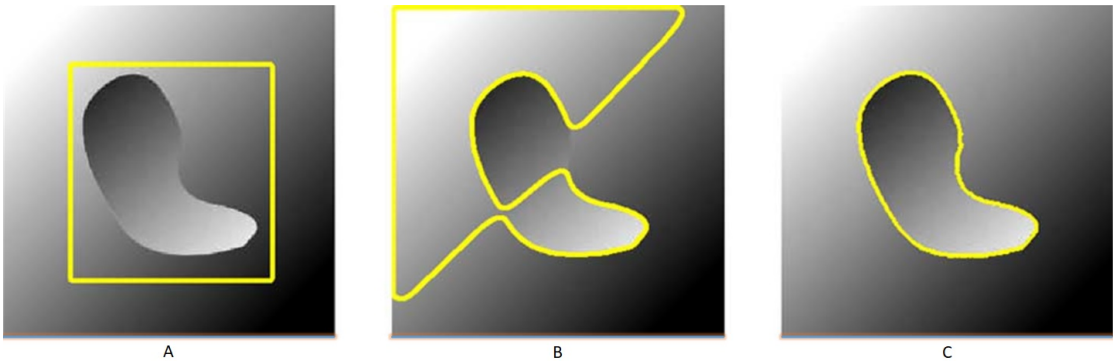

FIGURE 5.7: Synthetic image with heterogeneous intensity A) Initial contour. B) Region-based segmentation. (c) Edge-based segmentation. (adapted from [131])

placement of the contour and the image noise, such as the speckle noise in ultrasound images. On the other hand, the region based active contours [31] use the global intensity statistics of the regions to evolve the contour, until find the optimum choice. They are not sensitive to the initial placement of the contour and are insensitive to noise. However in heterogeneous images, they cannot distinguish the object from the background by using only the global statistics. It happens because in those images the foreground and background share roughly the same intensity profile.

The heterogeneous structures are usually visible in medical images like in the ultrasound. It was observed that the local intensity profile along the boundary of object in these images are statistically different and thus the local region analysis can robustly classify structures as foreground and the background. Based on that a localized active contours method was proposed [131].

5.5.1 Automatic Initialization

The boundaries of the AML obtained by the mathematical morphological techniques are used to initialize the active contours framework. Initial boundaries are close to the real boundaries, but are not well localized. Therefore, analyzing local regions can provide robust and well defined boundaries, with a few iterations.

5.5.2 Localized Active Contours

Ultrasound images are very noisy and frequently contain heterogeneous regions, and as such situations neither edge based contours, nor region based contours are suitable

choices. In this situation, we need a model that take the benefits from both edge and region based active contours. A localized region-based active contour (LAC) framework [131] were proposed to address this problem. This hybrid region-based curve evolution is robust to noise and doesn't rely on the global configuration of the image (see section 3.1.7).

The rough boundaries of the AML obtained from the morphological operators were used to initialize the LAC framework, to refine the leaflet boundaries. The algorithm is based on the analysis of the local circular regions with five pixels radius, at each point on the curve. At each point the algorithm locally identifies the background and foreground optimally by their mean intensities. The formulation of the local energy function along the curve is defined as:

$$\begin{aligned}\frac{\partial\phi}{\partial t}(x) = \delta\phi(x)\int_{\Omega_y} B(x,y)\,\delta\phi(y).((I(y)-u_x)^2 \\ -(I(y)-v_x)^2)dy + \lambda\delta\phi(x)div\left[\frac{\nabla\phi(x)}{|\nabla\phi(x)|}\right]\end{aligned} \tag{5.2}$$

Here, δ is the Dirac function, $B(x,y)$ represents a region that locally defines the interior and the exterior of the region at point "x" and the radius of the local region is specified by the user. The uniform modelling energy was used as an internal energy [31]. The localized version of the internal energy is defined as the local interior regions and exterior regions at each point on the curve. (υ_x, ν_x) are the localized version of means at each point x. The second term is the normalization term that keeps the curve smoother. It penalizes the arc length based on the weights λ tuned by the user.

5.6 AML Analysis

5.6.1 Skeletonization

Prior to performing the analysis, the shape of the AML was simplified by using skeletonization. Morphological thinning was used to get a line of one pixel width, while preserving the topological characteristics of the AML. Skeletonization works in the same way as morphological operators, convolving the structuring element (template) on the binary image. The Mark-and-Delete based templates were found very reliable and effective for thinning algorithms and thus used in this work [132]. Ultrasound images

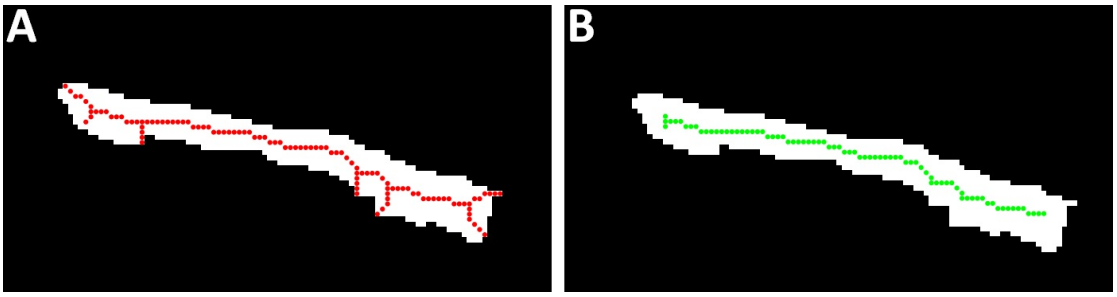

FIGURE 5.8: Segmented region of AML: A) Obtained skeleton B) Obtained skeleton after removing minor branches

are usually affected by the speckle noise resulting into irregular boundaries, producing superfluous minor branches of the skeleton. These branches are filtered out to extract the fundamental part of the skeleton. This can be done by computing the Euclidean distance between the branch and the end points. All those branches whose length are less than the defined threshold (6 pixels) are discarded (see Figure 5.8).

5.6.2 Motion Patterns

The focus of this stage was to compute the motion pattern of the AML and analyze it to extract the meaningful information. The mean motion of the X and Y coordinates of the skeleton was computed. The motion of the AML in X-axis was small and did not seem to provide any meaningful information. However, the motion of the AML in Y-axis has shown large motion with a unique pattern. The mean of the y-coordinates of the AML skeleton for each frame was plotted against time, showing the motion pattern of the AML (see Figure 5.9). The cardiac cycle was divided into systole and diastole phase based on the maximum and minimum of the peaks of the obtained motion pattern. The classification helps to label the AML as open or close and will be useful for the analysis such as, computing the thickness when the valve is open. Further work can help to classify frames in early filling and late filling phase (see Figure 5.9). The late filing will be useful to extract frames in which the AML is perpendicular to the ultrasound beam. This is the best position to measure the thickness of the AML tip, which provides a strong clue regarding the presence or not of diseases.

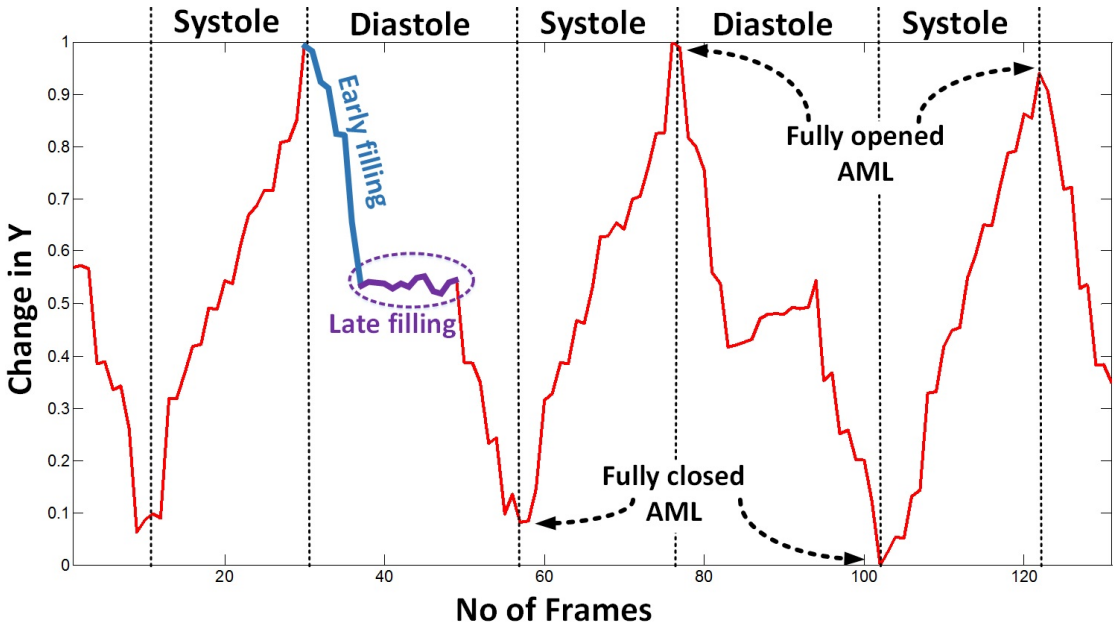

FIGURE 5.9: Motion patterns generated by AML

5.6.3 Shape

The hockey stick like appearance of the AML in PLAX view is an indicator of stenosis. A condition in which the heart valve leaflets get restricted (narrowed, blocked) resulting into interruption in the normal blood flow. In order to identify this condition, we proposed the measurement of the local curvature on the skeleton of the AML. A template based method was used to measure the local bending of the AML [133]. We tested two template based methods, the trigonometrical and crossover point method (see Figure 5.10).

The trigonometrical approach relates the crossover angle with the curvature (5.3). The crossover angle is the angle between the crossover point, where the curve intersects the disk mask and the X-axis of the disk. This approach is sensitive to noise to estimate the precise angle of the crossover points.

$$K_{tr} = \frac{2sin\theta_c}{1 - sin^2\theta_c} \tag{5.3}$$

The crossover point approach approximate the curvature by computing the area between curve and the disk, and is related to the crossover angle (θ_c). The squared area covered by the curve and disk are inversely proportional to the curvature (5.4).

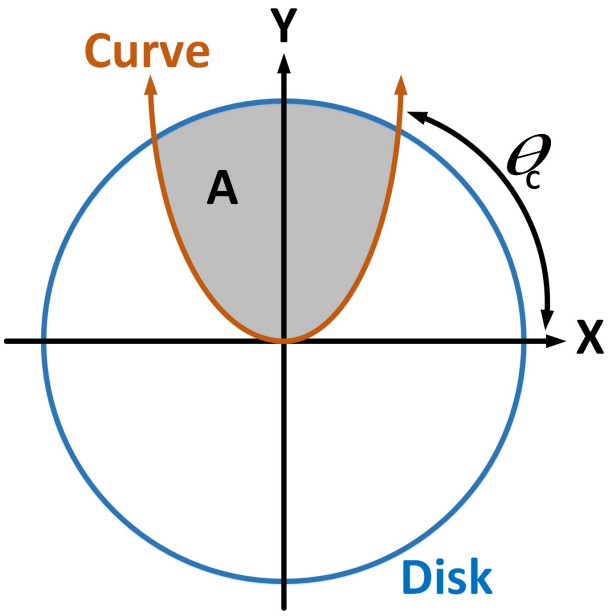

FIGURE 5.10: Curvature approximation using Area and crossover angle θ_c

$$K_{cp} = \frac{1}{A^2} \tag{5.4}$$

The obtained area is large for the small curvature. Thus the reciprocal of squared area is close to zero that increase the confidence by avoiding infinity and the reliability of the approach.

Experiments have shown that the area based method is less sensitive to speckle noise and provides smoother results, and was thus selected for this analysis. For each frame, we measured the local curvature at each point on the AML skeleton, followed by the computation of the overall mean to obtain the global curvature. In a stenosis, situation the leaflet is restricted and can be identified by the curvature (shape) change.

We observed that the motion pattern of the AML and the pattern of the global curvature change are correlated. When the valve opens the curvature of the AML tends to decrease showing the straightness of the leaflet and when the valve closes the curvature start increasing, suggesting the bending of the leaflet. This motion shape relation might help in the future by providing a clue to identify pathological condition.

For a better visual representation of the motion and curvature pattern, we first smoothed the curve and then normalize values to restrict them to the range (0-1) (see Figure 5.11).

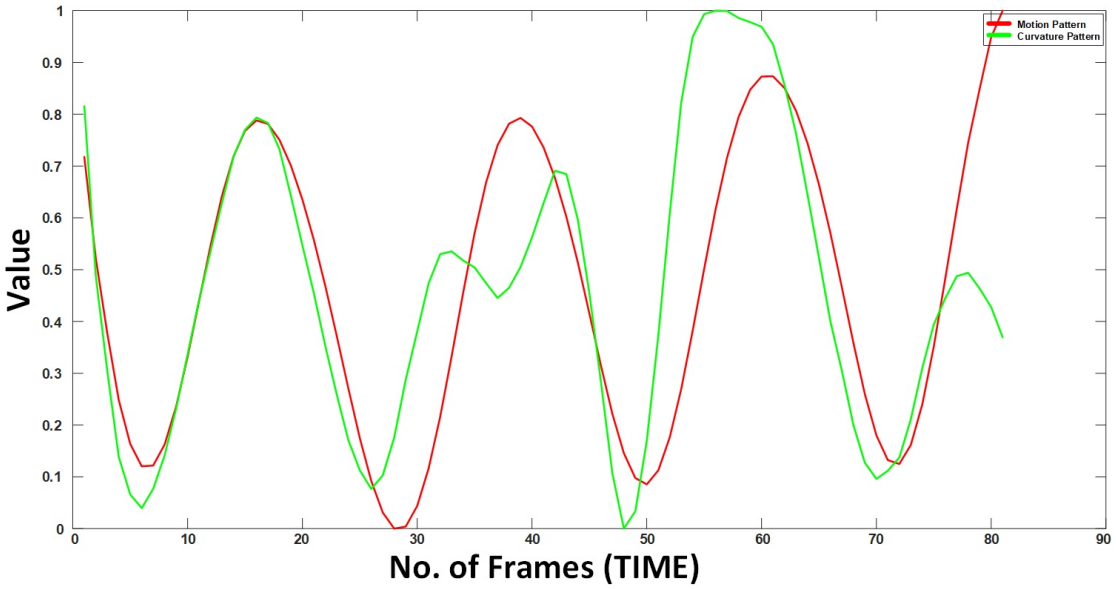

FIGURE 5.11: Motion and curvature pattern of AML, red: motion pattern, green: curvature pattern

5.6.4 Extended Modified Hausdorff Distance

The Modified Hausdorff Distance [119] was proposed to obtain a distance measure to match two objects. In this work, we extended this approach by categorizing the segmented region as false positive, false negative and true positive. We assumed that the nearest point between Automatic Segmentation (AS) and Ground Truth (GT) with Euclidean distance smaller than 2 pixels are true positives. The part of the AS that is falsely segmented as AML were considered false positives and the parts of the GT that were missed by the automatic segmentation were considered as false negatives, always using 2 pixels distance as reference "T" (see Figure 5.12), (5.5).

$$\begin{aligned} d_{AS\to GT} &= min\{AS, SEG\} \;\; FP = d > T \; TP = d < T \\ d_{GT\to AS} &= min\{AS, SEG\} \;\; FN = d > T \; TP = d < T \\ D_{MHD} &= max\left[avg\left(d_{AS\to GT}\right), avg\left(d_{GT\to AS}\right)\right] \end{aligned} \tag{5.5}$$

5.7 Materials

An initiative from the Real Hospital Português, in Recife, Brazil lead to the screening of 1203 children's and pregnant women, looking for cardiac pathologies. All patients were tested regarding the presence of streptococcal infection and short mitral valve videos

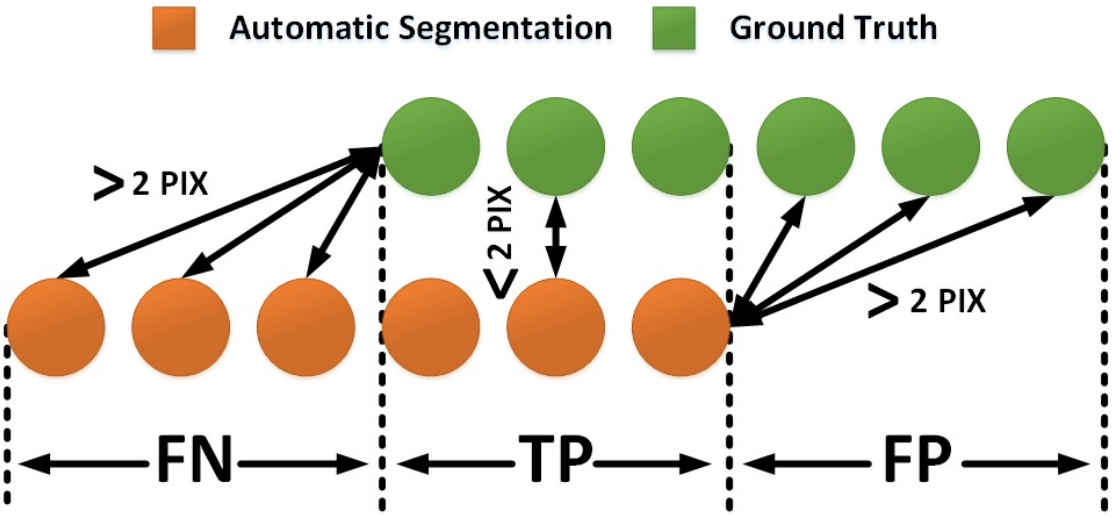

FIGURE 5.12: Region classification

were recorded. The data were collected using different ultrasound devices (M-Turbo, Edge II model by SonoSite, Vivid my model by *GE* health-care and *CX*50 model by Philips), with a wide range of transducers, frequency and scanning depths. The mean duration of the echocardiography videos is 2.9 sec with the mean frame rate of 34 frames/sec. Sixty seven of these exams was manually annotated by the doctors using Osirix software and were used to test the novel method proposed in this work. These sixty seven videos include a total of 6432 frames with a dimensions of 422×636 pixels. The proposed method has been implemented using *MATLAB* R2016b.

5.8 Experimental Methodology

In this work, the Extended Modified Hausdorff Distance (E-MHD) was used to evaluate the performance of the proposed algorithm. E-MHD not only help to compute the distance between two curves but also to define false positives, false negatives and true positives. The evaluation matrix consist of three parts. First, accessing the performance of the AML tracking by comparing the manual annotation (obtained by doctors) to the automatic annotation (obtained by the proposed method) using E-MHD. Second, the E-MHD error allows to compute the sensitivity and recall of the proposed method that shows how well the AML is segmented. Third, it allows the comparison to other studies, like in this work with our previous contribution [111] to evaluate the degree of improvement.

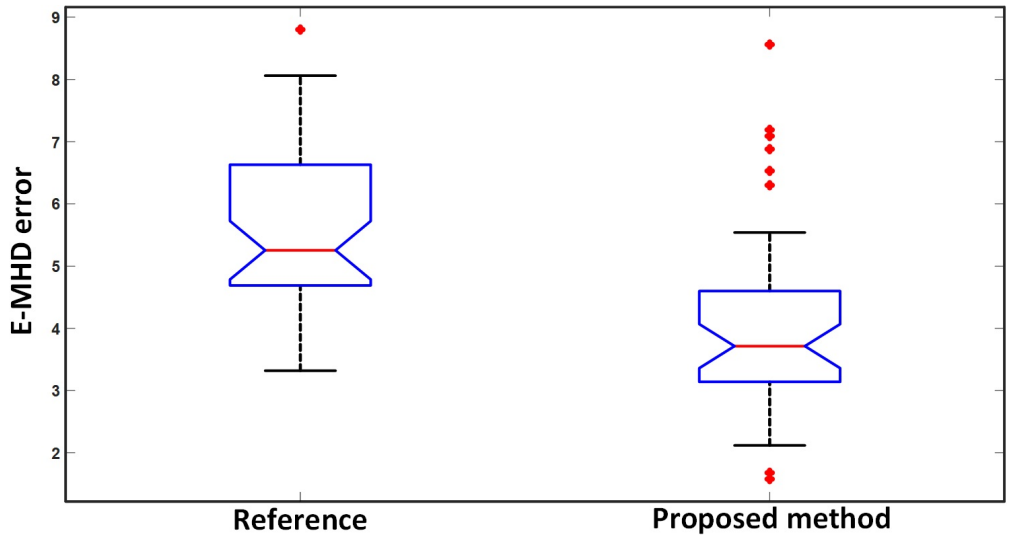

FIGURE 5.13: Extended modified Hausdorff distance error, 67 cases. Reference [111]

5.9 Tracking Results

In this work, we assumed perfect segmentation (manual annotation) for the first frame of the video, followed by a manual definition of a region of interest. This removes irrelevant structures to the right and left of the AML.

The performance metrics used were: the E-MHD error, the number of failures and the processing time. The morphological operators are relatively fast to obtain the boundaries of the AML, spending on average 0.4sec/frame on a desktop computer (Quad-Core AMD Phenom II processors, 3.2 GHZ, 8 GB RAM) in Window 10 environment. However the reference algorithm [111] consumes 1.2sec/frame. To refine the obtained boundaries, we used the LAC that consumes about 0.7sec/frame. The boxplot was used for the statistical analysis of the mean E-MHD and the number of failure in each video. The E-MHD error was computed for each frame of the video.

The boxplot of the E-MHD error (see Figure 5.13) shows that the median E-MHD error of proposed method is smaller than the reference algorithm [111], 3.7 and pixels 5.2 respectively. The most frequent error for the proposed method lies between 3.14 to 4.6 pixels. However, the reference algorithm [111] covers the comparatively large range from 4.6 to 6.6 pixels. The overall range of proposed method was also improved, from 2.1 to 5.5, whereas the reference [111] covers the higher values from 3.3 to 8.0 pixels. In Figure 5.13, the red dots show the outliers.

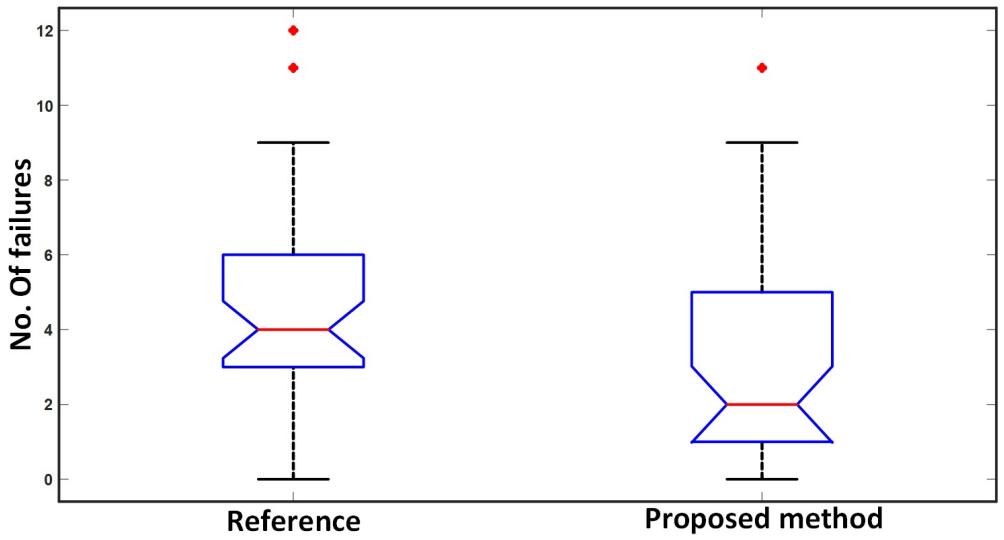

FIGURE 5.14: Number of failure in each video, 67 cases. Reference [111]

The proposed method has shown an improvement in tracking, with a median number of failure in each video of 2 (see Figure 5.14). The reference method [111] failed twice as much as the proposed method (median of 4). The most frequent range of failure of the proposed method was between 1 to 5 failures. On the other side, the reference method [111] shows between 3 to 6 failures.

The proposed algorithm has performed reasonably well, with respect to computational costs, E-MHD and number of failures. The main limitation of this work is the inability of the algorithm to avoid segmenting the neighboring regions. The algorithm can segment the whole leaflet with a sensitivity of 85% and a recall of 72%.

The segmentation results were plotted for better insight on this problem. Figure 5.15A and 5.15B show reasonable results with a fully segmented AML and with a small region falsely segmented as the AML. The quality of the ultrasound images are highly operator dependent. The skills of the operator directly affects the visibility of structures in an image. The Figure 5.15C shows the low visibility of the AML structure, and thus missed by the proposed algorithm. This situation is the main reason of the tracking failure in the proposed algorithm. In Figure 5.15D, the proposed method has segmented not only the AML, but also segmented the chordae tendineae and the posterior aorta. These missing and over-segmented regions are the responsible of having large E-MHD, with low sensitivity and recall.

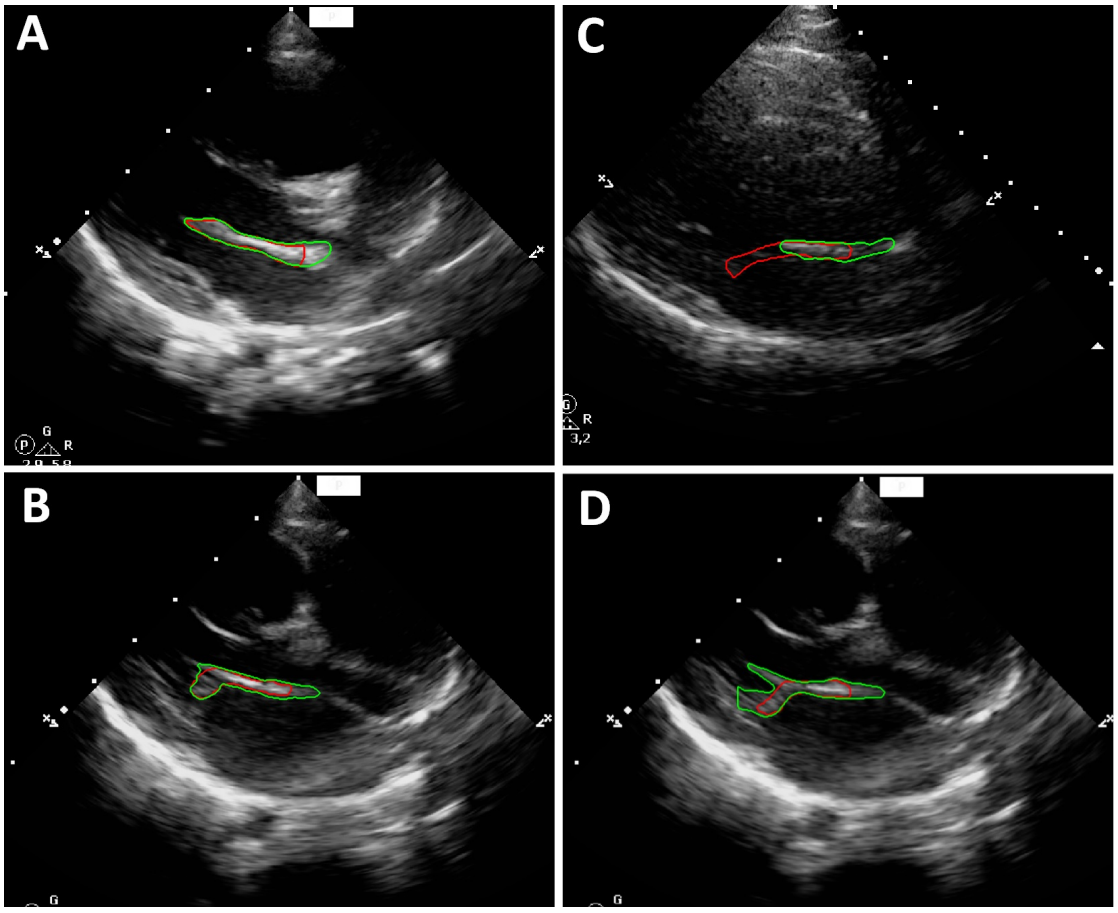

FIGURE 5.15: Segmentation results, red: doctor's annotation, green: proposed method

5.10 Discussion

In this work, a new tracking approach was proposed that uses morphological operators to predict the location and boundaries of the AML. To obtain more precise boundaries, the localized active contour framework was adapted. The algorithm was found robust to be in the difficult situations when the valve opens with a mean AML displacement of about 35 pixels. In such situations, active contours often fail to segment the boundaries (edges) that are far from the contour. The proposed algorithm outperforms the reference algorithm [111] with respect to time computational cost. It was still slow to reach a real time performance for the used hardware.

The main limitation of the algorithm was its incapability to avoid segmenting neighboring regions (chordae tendineae, cardiac walls, septum etc.). This happens because the intensity and texture of the neighbor regions are similar. The chordae tendineae and the posterior aorta are directly connected with the AML, containing the same features.

In this work, we defined a region of interest that minimizes this problem. However, we need an automatic system that robustly defines the region of interest and impose the shape constraints in the active contour framework to further improve the segmentation performance.

Another limitation of the proposed algorithm was its incapability to recover from the failure. This is the situation that occur frequently due to low quality of the image and due to the missing structures in several frame of the ultrasound video.

Chapter 6

Virtual M-Mode Space for the Anterior Mitral Leaflet Segmentation in Echocardiography Videos

This chapter is based on our contributions published in [134, 135]. The objective of this work was to minimize the limitations found in our previous contributions [111, 112, 125, 126] and in literature such: as, extensive user interaction, failure in frames with large leaflet displacement, excessive parameter adjustment, inability to recover from failure and to avoid segmenting the false positive regions (chordae tendineae, aortic valve, cardiac walls).

1. **M.S. Sultan**, N. Martins, E. Costa, D. Veiga, M.J. Ferreira, S. Mattos, M. Coimbra, "Virtual M-Mode for Echocardiography: A New Approach for the Segmentation of the Anterior Mitral Leaflet", (early access publication) in IEEE Journal of Biomedical and Health Informatics (DOI: 10.1109/JBHI.2018.2799738)

2. **M.S. Sultan**, N. Martins, E. Costa, D. Veiga, M.J. Ferreira, S. Mattos and M.T. Coimbra, "A New Method for the Anterior Mitral Leaflet Segmentation in Echocardiography Videos using the Virtual M-mode Space", in Proc. IEEE EMBC, Honolulu, Hawaii, Jul 2018.

It is unclear how the evolution of the promising active contours frameworks can address all limitations, which motivated us to try a different approach. What if we transform the image space into a simplified one, in which we can robustly identify and track selected points of the AML across time? This would give us a "seed point" per video frame, thus simplifying the segmentation of the full AML in the original echocardiography image. Our research questions are thus:

1. Can we transform the $2D$ echocardiography image space into a more adequate space for identification and tracking of the AML throughout time?
2. Can we successfully segment the AML in a single echocardiography frame, by using the seed points obtained from the previous step?

We contributed to this segmentation problem by proposing:

1. A new image space, called the virtual M-mode (VM-mode), obtained by sampling the original echocardiography image over automatically estimated scanning lines.
2. A new segmentation method for the anterior mitral leaflet, effective for every frame of the echocardiography video.

6.1 Virtual M-mode Space

The Motion mode (M-mode) echocardiography uses a single ultrasound beam over time to record the time events of the cardiac cycle (systole, diastole, early and late filling phase), and the chamber width [136]. It depicts the motion of structures towards or away from the transducer and has very high temporal resolution with a sampling rate of approximately 2000 frames/Sec. The M-mode remains a fundamental part of the echocardiographic screening. However, it is used only in selected situations, since the 2D ultrasound with frame rate of 30 to 100 frames provides more accurate anatomical measurements [136]. The distance between the tip of the AML to the septum in the early filling phase (diastole) is measured in the M-mode at the mitral valve level. It shows the extent of the opening of the valve and defines the global functioning of the left ventricle and provide the unique motion pattern that help to classify the cardiac

cycle into diastole and systole phase. Here it is important to note that the left atrium anteroposterior diameter was routinely measured in PLAX view using M-mode echocardiography. Following the American Society of Echocardiography guidelines (2015), it is no longer recommended to use this measurement due to non-symmetric shape of the LA in 3D space [137].

Can we exploit the benefits of the M-mode, by extracting a virtual M-mode from conventional 2D ultrasound?

We propose the sampling of the echocardiographic videos over time (frames) using a semi-automatic estimation of a scanning line, which results in a new image space, referred as VM-mode. The VM-mode provides us clues (a seed point) to identify the AML in each frame of the video. The work was inspired from the M-mode echocardiography that has the ability to accurately assess the rapid anterior mitral leaflet movement and register the time events of the cardiac cycle.

In this work, the only manual step was to insert a single user specified point P_{Ref} and an angle (θ), on the very first frame, much like what cardiologists do during regular M-mode echocardiography. The location of the point (P_{Ref}) and the angle (θ) was then used to compute a scanning line, $L(P_{Ref}, \theta)$ that samples the echocardiographic video over time to get a VM-mode, as in (6.1).

$$\begin{aligned} x_{Line} &= \pm r cos\theta + x_1 \\ y_{Line} &= \pm r sin\theta + y_1 \end{aligned} \quad \begin{cases} \frac{y_1 - 1}{sin\theta} \leq r \leq \frac{W - y_1}{sin\theta} \\ \frac{x_1 - 1}{cos\theta} \leq r \leq \frac{H - x_1}{cos\theta} \end{cases} \tag{6.1}$$

Where, (x_1, y_1) are the Cartesian coordinates of the point P_{Ref} and r is the distance from the point P_{Ref} and remains within the horizontal and vertical limits of the image, of height H and width W. The sign $\pm$ shows that the line extends in both directions from the point P_{Ref}. We have tested the sampling line with several angles and found that the 90° angle better approximates the motion of the Anterior Wall of the Aorta (AWA), Posterior Wall of the Aorta (PWA) and Posterior Wall of the Left Atrium (PWLA). Different angles of the scanning line may intersect irrelevant structures in an image, which leads to erroneous motion patterns. This is reinforced by the fact that in the standard PLAX view, the sonographer is supposed to make sure that the structure of the septum is as horizontal as possible. Thus, the other structures like the mitral

valve, left atrium and left ventricle in the PLAX view are also horizontal. Therefore, a scanning line with a 90° degree angle is the most obvious choice. The selection of a proper P_{Ref} point is fundamental, since sampling image at different locations provides different motion patterns. The tip of the AML is not an adequate location since it is not always visible, has large, fast and irregular motion patterns. On the other hand, the baseline of the AML exhibits smaller and more regular motions and provides better structure visibility, making it the preferred location to initialize our method. The baseline of the AML is the location where the PWA connects with the AML. In short, a single point P_{Ref} manually inserted on the PWA was enough to initialize our method with the default 90° degrees angle Figure 6.1.

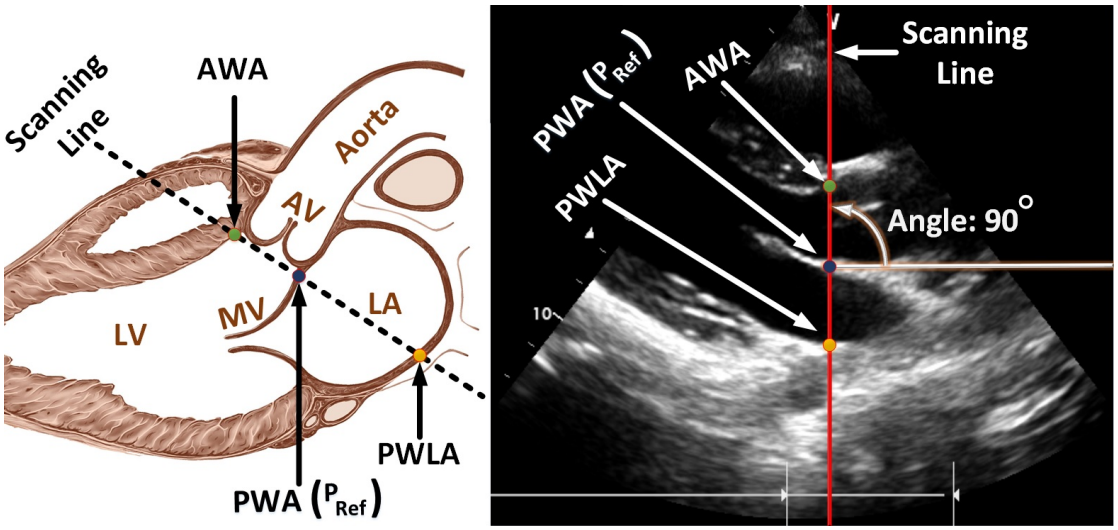

FIGURE 6.1: Initialization point (P_{Ref}) at the posterior wall of the aorta (PWA) with a default 90° angle and the scanning line intersecting with the anterior wall of the aorta (AWA) and the posterior wall of the left atrium (PWLA).

Since the quality of the ultrasound images is low, commonly affected by speckle noise and with missing visualization of the AML, sampling through a single scanning line L_{i1} may lead to some missing information. Therefore, instead of sampling through a single scanning line L_{i1}, we used five consecutive scanning lines with one pixel apart that results into a matrix $L_{ij} \in \mathbb{R}^{M \times N}$. Where, M is the length of initial scanning line and N is the number of lines.

The images are sampled with the defined metrics L_{ij} over time (frames) and analyzed to find the missing value in each row. The missing entries are then filled using $1D$ linear interpolation and at the boundaries empty entries are filled with the nearest non-zero

values in the neighborhood. Finally, we take the mean of each row to construct the sampled line (SL), as in (6.2)

$$SL_{i1} = \frac{1}{N}\sum_{j=1}^{N}[L_{ij}]_{nn}^{lin} \tag{6.2}$$

Where, N is the number of lines, lin is the linear interpolation and nn is the nearest neighbor. The sampled line was computed overtime to obtain the VM-mode, as in (6.3), Figure 6.2

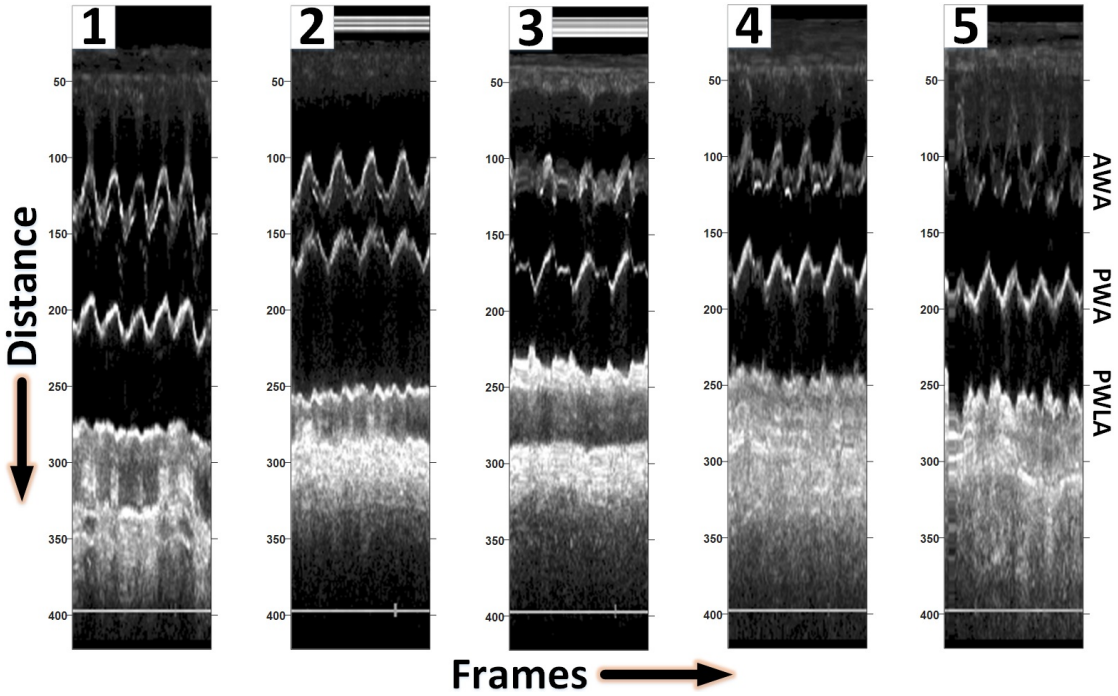

FIGURE 6.2: VM-mode obtained from 5 videos. X-axis shows the number of frames and Y-axis showing the distance from the transducer. Visible structures are the anterior wall of the aorta (AWA), posterior wall of the aorta (PWA) and posterior wall of the left atrium (PWLA)

$$\begin{aligned} VM_{mode} &= \begin{bmatrix} SL_{11} & SL_{12} & \cdots & SL_{1T} \\ SL_{21} & SL_{22} & \cdots & SL_{2T} \\ \vdots & \vdots & \ddots & \vdots \\ SL_{M1} & SL_{M2} & \cdots & SL_{MT} \end{bmatrix} \\ &= (SL_{ij}) \in \mathbb{R}^{M\times T} \end{aligned} \tag{6.3}$$

Where, T is the total number of frames in echocardiographic video.

In conventional M-mode, the single vertical measurements are manually obtained, showing the position of a structure in a specific frame only. In the VM-mode, we can automatically measure the width of the left atrium, aorta and can compute the aspect ratio throughout the cardiac cycle.

In conventional M-mode the user manually takes several vertical measurements on certain frames of the M-mode that show the width of the left atrium and aorta in the diastole and systole phase. In our VM-mode, we propose a methodology to automatically segment the region of anterior wall of the aorta (AWA), posterior wall of the aorta (PWA) and posterior wall of the left atrium (PWLA) (section III-A). Using these segmentation results, it is possible to measure the width of the left atrium, aorta and can compute the aspect ratio throughout the cardiac cycle. However, this was out of the scope of this work, and so we propose the study of these metrics as future work. This information can provide a strong clue to identify valve abnormalities. The VM-mode also provide the motion patterns of the structures which helps to record the time event of the cardiac cycles, followed by computing the seed points on $2D$ image for the effective identification of the AML.

6.2 Identify the AML in Each Frame using the VM-mode

The methodology adapted in this work to segment the AML throughout the cardiac cycle was based on the estimation of the previously presented VM-mode. The method pipeline is presented in Figure 6.3.

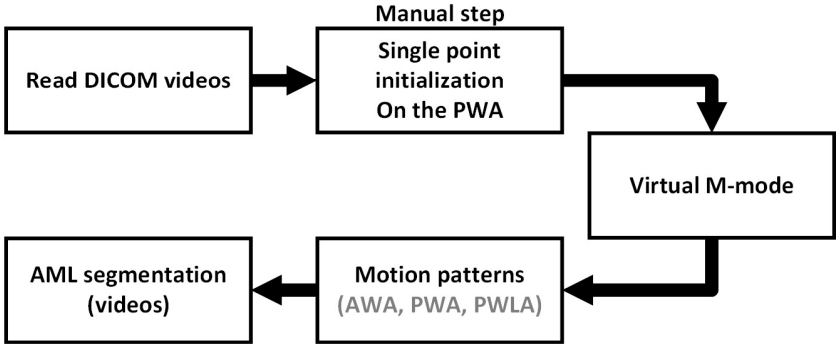

FIGURE 6.3: The pipeline of the method to segment AML in echocardiography videos.

The first step was to read the echocardiography videos in $DICOM$ format and apply contrast stretching to normalize the illumination. The only manual step in this work

was to insert a single point on the PWA to initialize the VM-mode. The VM-mode contains the motion and location information of the structures (AWA, PWA and PWLA) over time. Therefore, by segmenting each structure, it is possible to reconstruct motion patterns as well as their location on the $2D$ image. The location information provides a clue of the position of the AML in each frame which leads to a robust and efficient way to segment each frame with high confidence. Finally, the AML was segmented using localized active contours, initialized by the seed point.

6.2.1 Estimating Motion Patterns from the VM-Mode

The VM-mode contains motion and location information of the structures in $2D$ PLAX view over time. So the automatic segmentation of those structures in the VM-mode can provide local information of each structure on the $2D$ PLAX images. To achieve this, a two-step strategy was proposed. In the first step, we segment the region of the PWA with the new approach that computes the location over time on the sampled line (SL). In each frame, the location of the PWA was computed using the previous frame as reference and by taking the local optimal choice. In the second step, we adapted the open ended active contour to segment the region of the PWLA and the AWA. The active contour was automatically initialized by the previously segmented region of the posterior aorta.

- Posterior wall of the aorta (PWA)

The motion pattern of the PWA was obtained simultaneously while obtaining the VM-mode. The initialization point P_{Ref} Figure 6.1 manually inserted to get the VM-mode is tracked throughout the cardiac cycle. A minimum path was used which continuously computes the movement of the PWA on the discrete indices of the sampled line Figure 6.4. The proposed framework consists of internal and external energy, as in (6.4).

The analysis of the VM-mode reveals that the region of the PWA is a continuous region and shows regular motion patterns. This prior knowledge was incorporated in the internal energy to assign higher weights to the pixels near to the reference point on the scanning line Figure 6.4A. The position of the current point (i) was computed based on its position in the previous frame ($i-1$). The internal energy consists of

Euclidean distance metric that was computed from the reference point V_{ref} to the pixel locations on the scanning line V_R. The pixels further away from the reference point has higher distance measure than the ones nearby. Therefore, we take the complement of the obtained metric to assign higher distance measures (weights) to the locations close to the reference point Figure 6.4A that increase the probability of being the location of the AML.

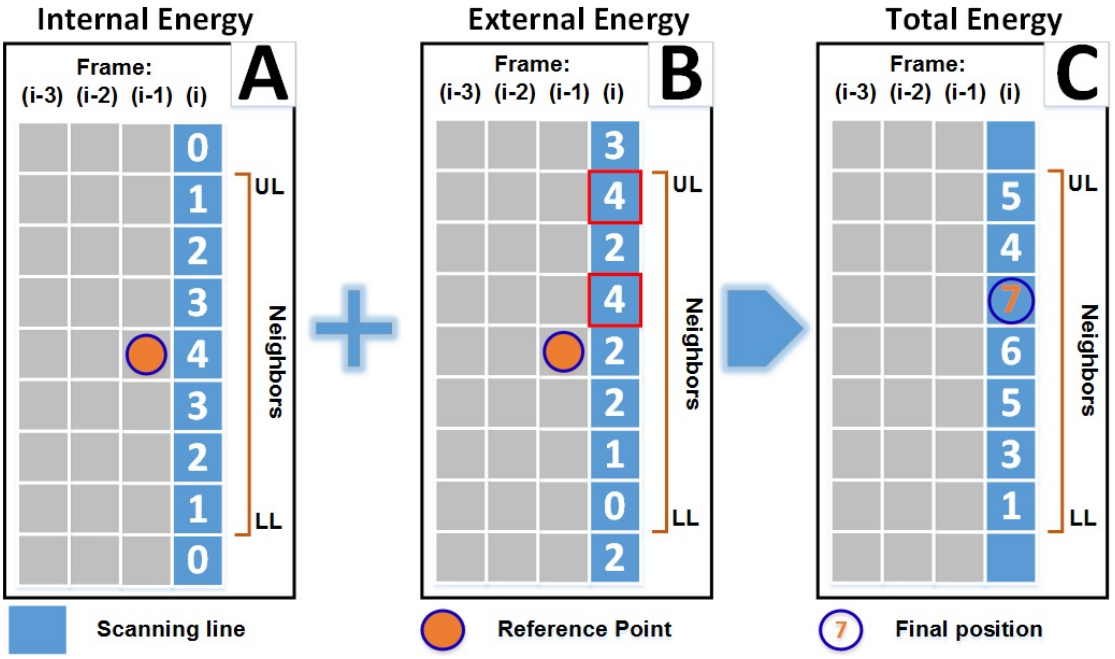

FIGURE 6.4: Model details: Internal, external and total energy. Movement of points on the scanning line to segment pattern of the posterior wall of the aorta (PWA) in VM-mode. UL and LL are respectively, the upper and lower limits.

In the external energy, we simply used the intensity values smoothed by the Gaussian filter with a standard deviation of 2, as in (6.4), Figure 6.4B.

$$\begin{aligned} E_{Total} = & \quad E_{Internal} + E_{External} \\ = & \quad \alpha \left| V_{ref} - V_R \right|_C^2 + \gamma \left| G_\sigma \times SL_R \right|^2 \end{aligned} \tag{6.4}$$

Where, the parameter α and γ with values 0.3 and 0.8 respectively, control the relative importance of the distance constraint (internal) and the influence of the sampled line (SL), respectively. C is the complement of the distance vector. G is the Gaussian smoothing with sigma ($\sigma = 2$). V_{ref} is the reference point and V_R are the discrete indexes on the scanning line (L) and R is the defined range of selected neighbor regions.

A greedy optimization approach was used to maximize the total energy. The movement of each point appears on the locally defined region. In each frame the model makes the locally optimal choice on the sampling line. The neighbor regions R are defined and updated for the upcoming frame Figure 6.4 and are computed using the upper limit (UL) and the lower limit (LL), as in (6.5)

$$\begin{aligned} \mu &= \tfrac{1}{T-1}\textstyle\sum_{i=1}^{T-1} V_i \quad \sigma = \sqrt{\tfrac{1}{T-1}\textstyle\sum_{i=1}^{T-1}(V_i-\mu)^2} \\ LL &= \mu + \sigma + C \qquad UL = \mu - \sigma - C \end{aligned} \tag{6.5}$$

In each stage, the mean (μ) and standard deviation (σ) of the estimated positions V_i of the PWA in the previous frames ($T-1$) are computed to update the defined limits. The value of C is the maximum possible displacement of the PWA from one frame to another.

In short, the $2D$ image was sampled over time using the estimated scanning line (L). In each time frame, the position of the PWA was calculated on the sampled line (SL) under the distance constraint and within the defined neighborhood (UL, LL) which was updated periodically. The results obtained by the proposed method are shown Figure 6.5, red annotation

- Anterior wall of the aorta (AWA) and posterior wall of the left atrium (PWLA)

In this module, we address the segmentation problem of the AWA and the PWLA. The open ended active contours [111, 112] are adapted to segment these regions. Each column of the VM-mode shows the sampling results of each frame and thus contains important motion information of the structures. Therefore, a single contour point is needed for each column and was constrained to move only in the vertical direction. The total energy of the active contour consists of internal and external energy, as in (6.6). The internal energy consists of the first derivative (elasticity) that encourages the contour points to stay close to each other and the second derivative (stiffness) which controls the bending of the curve. Removing the influence of elasticity and stiffness on the end points of the contour, results into open ended contours (free boundary condition) [138]. In the external energy, we used the edge information of the VM-mode that aligned the contour points at high image gradients.

$$E_{Total} = \int_0^1 \left[\frac{1}{2} \left(\alpha \left\| \frac{\partial V}{\partial S} \right\|^2 + \beta \left\| \frac{\partial^2 V}{\partial S^2} \right\|^2 \right) + \gamma E_{image}(V) + K \overrightarrow{n} \perp V \right. \tag{6.6}$$

Where, the parameters α, β and γ with values 0.5, 0.2 and 0.8 respectively, control the relative importance of each energy. A pressure force was added in the external energy to get stable results [94]. If the initial contour is not close to the true image gradient, the pressure force evolves the contour under the predefined direction to get the true boundaries. K ($\pm$ 0.2) is the weight of the pressure force and its sign controls the direction of motion (negative for upward and positive for downward). The weight γ of the image energy should be higher than the weight K of the pressure force, in order to make sure that the curve cannot pass through the edges. $\vec{n}$ is the norm vector at the contour point.

Active contour models require an initialization step. In order to perform an automatic initialization, the prior knowledge of the anatomy of the VM-mode is used. One can verify from the VM-mode Figure 6.2 that the motion patterns of the AWA and the PWLA are above and below the motion pattern of the posterior aorta. Following this fact, the global maximum and minimum of the motion pattern of the PWA was computed, resulting in two distance values. For the PWLA, all the contour points were initialized using the maximum distance and with positive direction, while the opposite was done for the AWA. The obtained results are shown in Figure 6.5 green and blue annotations.

Eventually, the computed motion patterns are translated on the scanning line (see Figure 6.1) to get the location of each structure (seed points) back on the $2D$ image.

6.2.2 AML Segmentation

The echocardiographic images are very noisy and mostly contain heterogeneous regions. Following the nature of the images, the localized region-based active contours (LAC) [131] are the most adequate choice and thus used in this work. In each frame, the LAC were initialized by the seed point on the PWA, obtained from the VM-mode. The LAC use the local statistics to define foreground and background, instead of relying on global statistics. At each point on the curve, the LAC framework analyses local circular regions

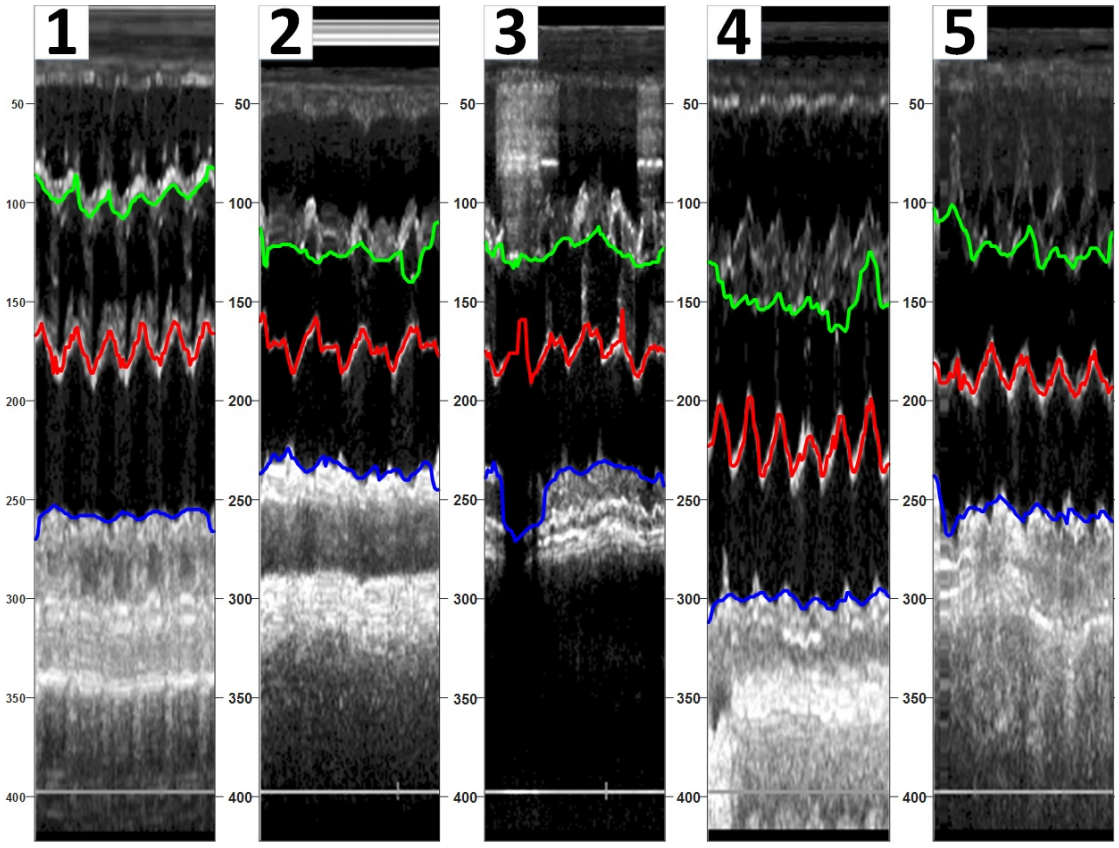

FIGURE 6.5: Segmented motion patterns of the VM-mode in 5 videos. Green: Anterior wall of the aorta (AWA), Red: Posterior wall of the aorta (PWA), Blue: Posterior wall of the left atrium (PWLA).

of the user specified radius (5 pixels). Based on the mean intensity of the local regions, the method locally identifies the region as foreground or background. The mathematical formulation of the model is given below

$$\begin{aligned} \frac{\partial \emptyset}{\partial t}(x) = \delta\emptyset(x) \int_{\Omega_y} B(x,y)\, \delta\emptyset(y) .((I(y) - u_x)^2 \\ -(I(y) - v_x)^2)dy + \lambda\delta\phi(x) div\left[\frac{\nabla\emptyset(x)}{|\nabla\emptyset(x)|}\right] \end{aligned} \tag{6.7}$$

Here, $B(x, y)$ is the circular mask of defined radius to locally identify interior and exterior regions, at point x. u_x, v_x are the local means, I is the image in the domain Ω, $\delta\phi(x)$ is the smoothed Dirac delta function. The second term ensure that the curve is smooth and is called as regularization term, λ is the weight manually tuned by the user to adjust arclength of the curve. To summarize, the contour point iteratively moves inside the circular mask, until it reaches the location that is well approximated by the local mean intensities. The results of the proposed method are shown in Figure 6.6.

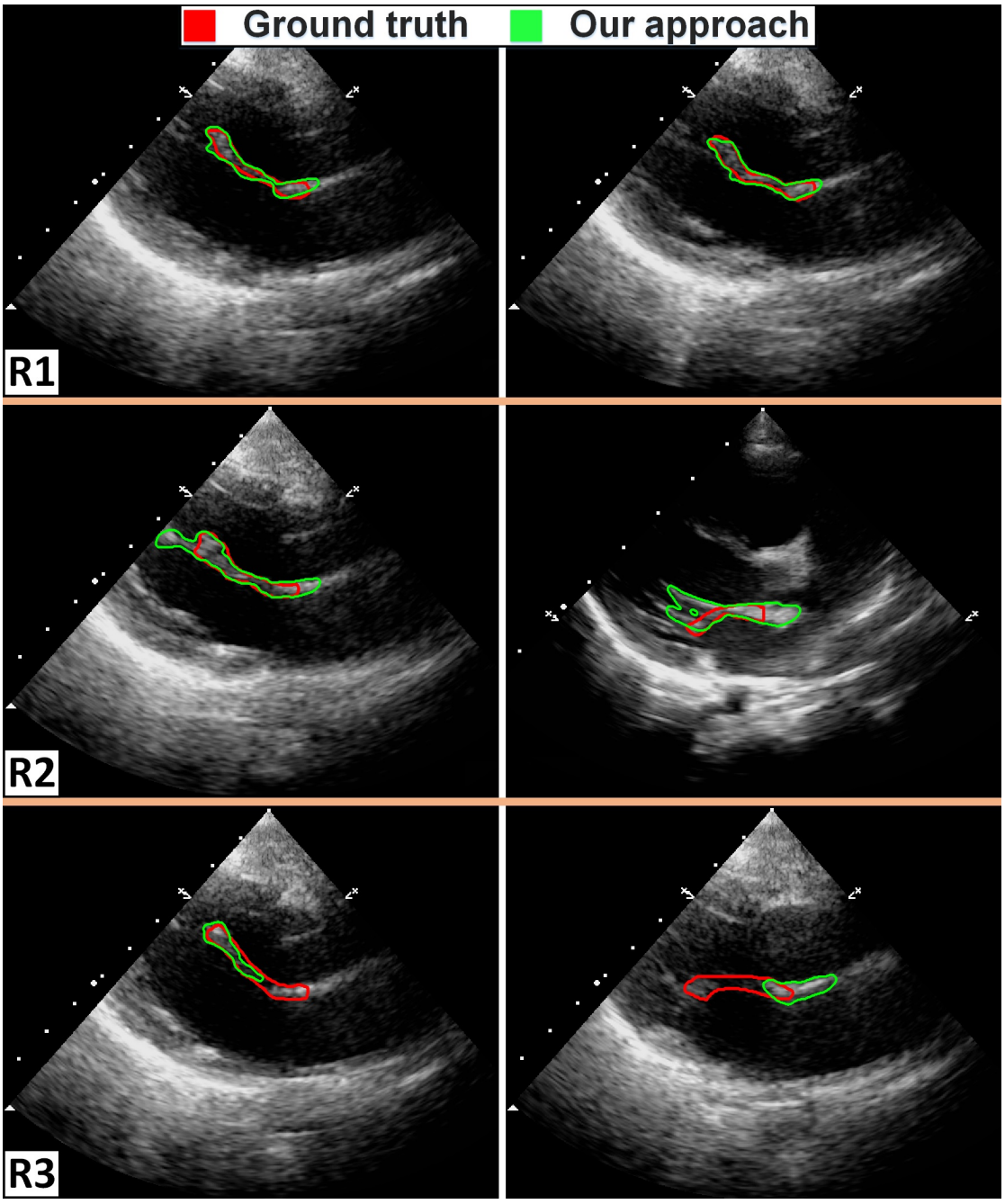

FIGURE 6.6: Segmentation result, row 1: good segmentation, row 2: segmentation with outliers, row 3: segmentation with missing parts.

6.2.3 Materials

An initiative from the Real Hospital Português, in Recife, Brazil lead to the screening of 1203 children's and pregnant women, looking for cardiac pathologies. All patients were tested regarding the presence of streptococcal infection and short mitral valve videos were recorded. The data were collected using different ultrasound devices (M-Turbo, Edge II model by SonoSite, Vivid i model by *GE* health-care and *CX*50 model by

Philips), with a wide range of transducers, frequency and scanning depths. Depending on the equipment and depth, the spatial resolution ranged was between 0.115 to 0.384 mm. The mean duration of the echocardiography videos is 2.9 sec with the mean frame rate of 34 frames/sec. Sixty seven of these exams were manually annotated by the single doctors using Osirix software[1] and were used to test the novel method proposed in this work. The dataset was balanced, having 33 pathologic cases and 34 normal cases. These sixty seven videos include a total of 6432 frames with a dimensions of 422×636 pixels. The proposed method has been implemented using MATLAB R2016b (MathWorks Inc., Natick, MA, USA) on a desktop computer (Quad-Core AMD Phenom II processors, 3.2 GHZ, 8 GB RAM) in Windows 10 environment.

6.2.4 Experimental Methodology

For the comparison, we selected two state of the art reference method which address the problem of AML segmentation in 2D echocardiography and are provided with the source code [26, 125]. For the validation, firstly we computed the Modified Hausdorff Distance (MHD) against the ground truth for each method, followed by the comparison of the proposed method with the reference methods. The first reference method ($Ref.1$) use basic mathematical morphology features to obtain the initial boundaries of the AML that are further refined using a localized active contour approach [125]. The second reference method ($Ref.2$) is based on the continuous outlier detection to identify fast moving regions like the AML, chordae tendineae and papillary muscles. The regions of the AML are classified using either morphological operations or graphcut and then, the obtained boundaries are refined using active contours [26].

In this work, the modified Hausdorff distance (MHD) [119] and the number of tracking failures will be used as performance metrics. The MHD was used to compare the results of automatic segmentation with the ground truth (manual annotation by the doctor). The failure was a pre-defined condition, in which the automatic segmentation method delineates a structure other than the AML. To identify failure, we rely on spatial overlap ($AS \cap GT$) and the Euclidean distance between the binary regions $D(AS, GT)$, the automatic segmentation (AS) and the ground truth (GT) respectively, as in (6.8)

[1] https://www.osirix-viewer.com/osirix/osirix-md/

$$f(i) = \begin{cases} 1 & if \begin{bmatrix} AS \cap GT = 0 \\ min\left(D\left(AS, GT\right)\right) > T \end{bmatrix} \\ 0 & Otherwise \end{cases} \tag{6.8}$$

Where, i is the frame number. In some cases, when we have the missing visualization of the AML in certain frames, the algorithm might segment some small regions near the real boundaries of the AML. Thus, there is still a chance that the algorithm found the true boundaries in the very next frame. To identify this possibility, we measure the Euclidean distance between the falsely segmented region and the ground truth. If it is smaller than the defined threshold, there is a great possibility that the algorithm recover and segment the true boundaries of the AML in upcoming frame. The Euclidean distance of $T = 14$ mm was adjusted by taking the diameter of the aortic annulus in our videos as reference, ranged from (14 –26 mm). A region at the distance of more than 14 mm reflect that some neighbor region is segmented.

For each video, we count the number of times the above condition was true and this was used as the number of failures. The precision and recall were obtained by analyzing the spatial overlap of the binary regions [139]. The precision is the measure that reflects how much noise do we have in the segmentation and the recall shows how much of the ground truth is detected.

6.2.5 Segmentation Results

Boxplots are used to visualize the statistical measures of the segmentation, most importantly the variability, the median and the spread. The MHD error for each frame of the video and the median of all frames was computed. The median MHD error for the whole dataset (67 videos) was analyzed and presented in Figure 6.7.

Figure 6.7 clearly shows that the median MHD error of the proposed method is smaller than the reference approaches, with a value of 2.3 mm, whereas the median error of the $Ref.1$ and $Ref.2$ is 3.8 mm and 5.7 mm respectively. The range of the most frequent error is estimated by computing the width of the box that is from the 25^{th} percentile to the 75^{th} percentile. The range of the error in our approach was between 1.7 to 3.2 mm, for the $Ref.1$ it was between 3.2 to 5.3 mm and for the $Ref.2$ it was between 4.7 to

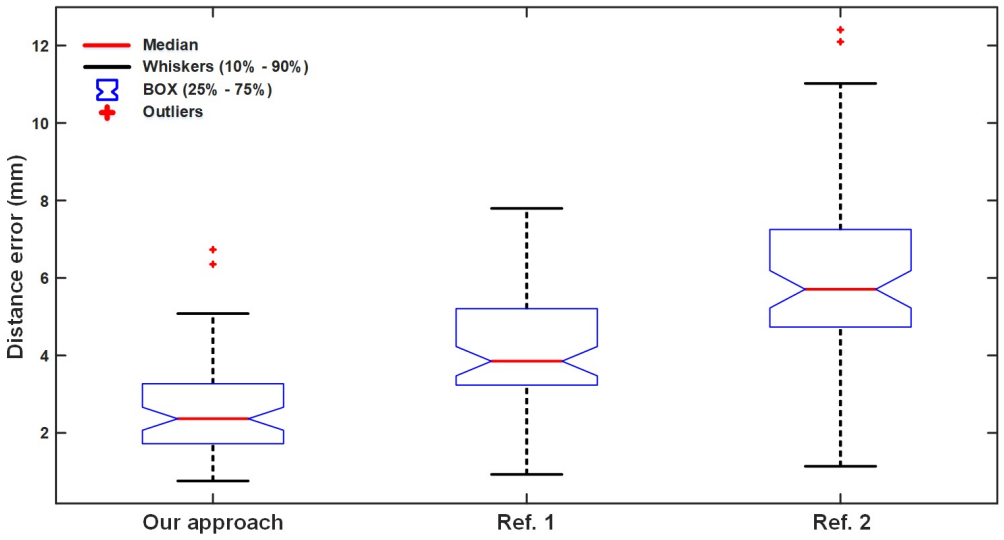

FIGURE 6.7: Evaluation of segmentation with MHD error (mm) obtained against the ground truth for our approach, Ref.1 [125] and Ref.2 [26] using 67 videos.

7.2 mm. The upper and lower whiskers of each boxplot provide the total spread of the median MHD error. The median MHD error of the proposed approach has less spread (4.24 mm) than the reference approaches (6.87 mm, 9.89 mm).

The statistical difference between three approaches were tested using a non-parametric Friedman test. The mean rank difference between our approach, Ref 1 and Ref 2 was 1.1, 2.1 and 2.8 respectively. The computed difference between three methods were significant with the P-value of < 0.0001.

The computational cost of the proposed method can be divided in three parts: 1) The time it takes to preprocess the DICOM file, averaging 3.5s; 2) The calculations for the VM-mode and the motion pattern of the Posterior Wall of the Aorta (PWA) takes, on average 18s; 3) the LAC algorithm depends on the number of iterations but on average it requires 7s for 50 iterations.

The number of failures per video for the whole dataset provides an important performance metric of the tracking capability. For each video, the total number of frames was divided by the number of failures, to get the average number of frames between failures. The results are presented in Figure 6.8.

The boxplot shows that our method does not fail, though the $Ref.1$ method fails around once every 30 frames and the $Ref.2$ method fails more frequently, around once every 25 frames.

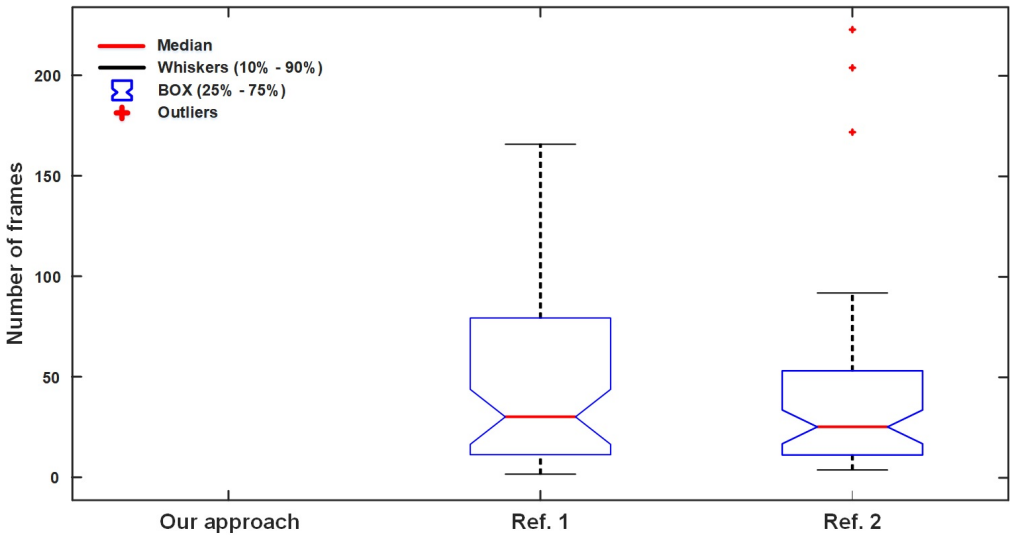

FIGURE 6.8: Failure after an average number of frames for our approach, Ref.1 [125] and Ref.2 [26] using 67 videos.

The recall and precision were used to evaluate the segmentation consistency in the whole dataset (Table 6.1). It was calculated based on the overlap between the segmentation results and the ground truth.

TABLE 6.1: Comparison of Precision and Recall (67 videos)

	Our approach	Ref. 1 [125]	Ref. 2 [26]
Recall	0.94	0.73	o.66
Precision	0.50	0.51	0.45

The recall of the proposed method was much higher (0.94) than the reference method (0.73, 0.66). It shows that the proposed method can successfully detect the most part of the ground truth (see Figure 6.6 R1, R2). The limitation was the discrete AML structure in the ultrasound images. The proposed method fails to overcome the gaps and cannot jump to segment the whole leaflet (see Figure 6.6, R3).

The ultrasound images have a low quality and no reliable features (similar intensity for all structures). The automatic segmentation results into significant over-segmentation (see Figure 6.6, R2) that leads to low precision. The over segmentation means the proposed method not only segments the AML, but also fails to avoid segmenting unwanted regions like, chordae tendineae, papillary muscles, anterior aorta and cardiac walls.

6.2.6 Discussion

The results presented in the last section show that the proposed method outperforms the current state of the art, achieving promising results in the whole dataset (67 videos). The conversion of the ultrasound video to the new image space (VM-mode) makes it possible to identify the AML in the most difficult situations. The method was able to handle large frame to frame displacements, and missing structures. Another benefit of the proposed method is the minimum user interaction, a single point, manually specified on the PWA can robustly initialize the proposed method. The method has worked equally well for both the normal and pathological cases Figure 6.9.

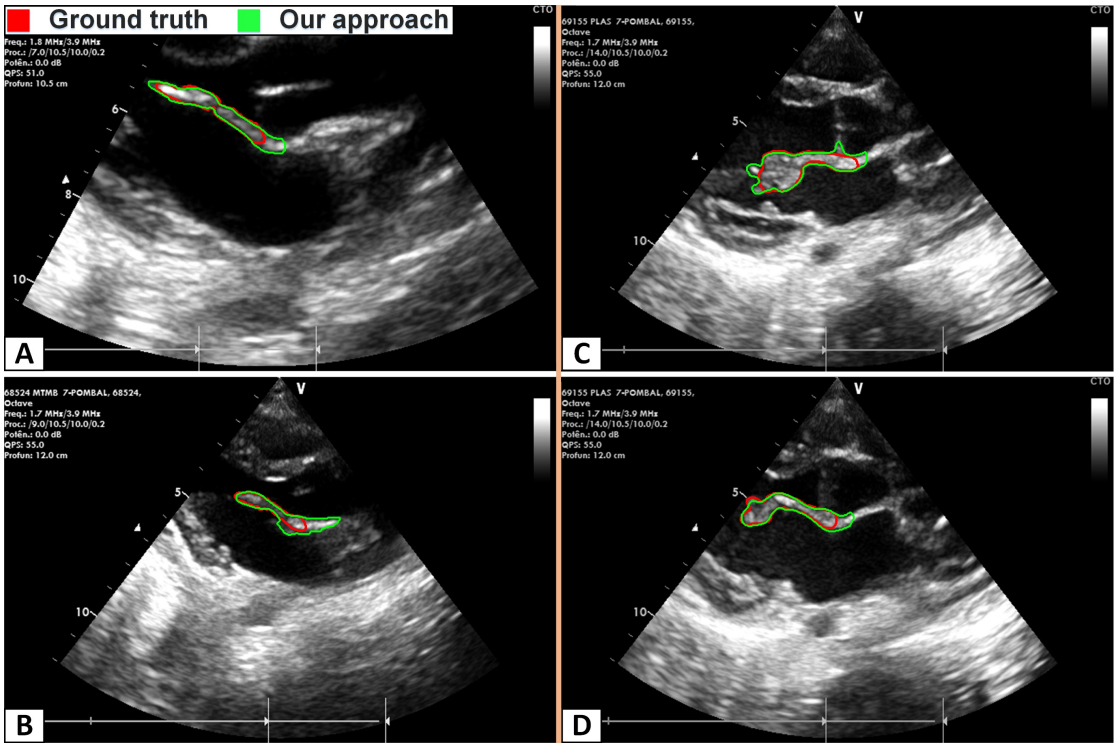

FIGURE 6.9: Segmentation result, A, B) Normal, C) Thickened D) Hockey shape leaflet.

The earliest manifestation of RHD is the thickened AML Figure 6.9C, that restricts the normal opening and closing of the valve. The restricted tip of the AML shows the doming motion (hockey like appearance) in the diastole phase, in the PLAX view Figure 6.9D.

The main limitations of the proposed method is over and under segmentation. It mainly occurs due to same texture and intensity of neighbor regions (over segmentation), and due to the discrete region that results from the low image quality or improper scanning

(under segmentation). This can be possibly minimized by incorporating additional shape constraints in the proposed model.

6.3 Segment the Whole AML in Each Frame using the VM-mode

The objective of this work was to segment the AML in echocardiography images throughout the cardiac cycle. The key contributions of the proposed work are:

- Sampling the echocardiography images over time by automatically estimating a set of scanning lines.
- Obtaining the rough estimation of the full AML in the original image space by using the VM-mode space.

The methodology adapted in this work to segment the AML is summarized in Figure 6.10.

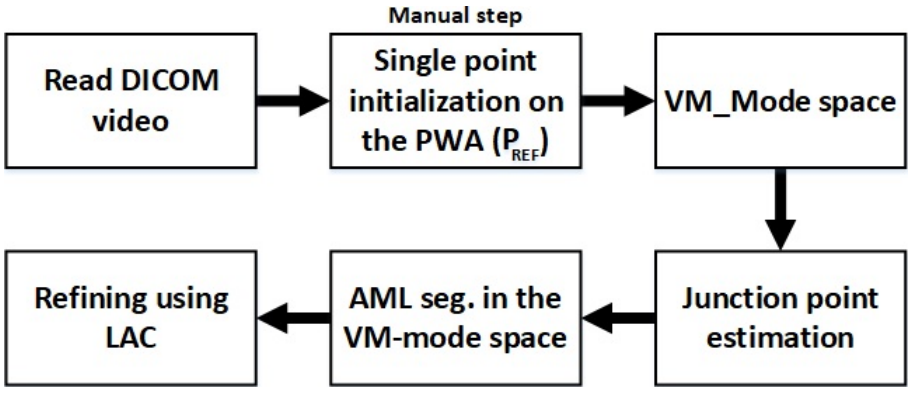

FIGURE 6.10: Pipeline of the AML segmentation in echocardiographic videos.

In the first step, the echocardiographic video in DICOM format was read. The second step was the only manual step, requiring a single point initialization on the PWA, in the very first frame. This consists of a single mouse click over a pixel belonging to the PWA. The third step involves the creation of multiple scanning lines that are used to sample whole image over time, resulting in multiple images in the VM-mode space. In the fourth step, a single image was created using the whole stack of images in the VM-mode space, which was used for the estimation of the mitral leaflet junction's location.

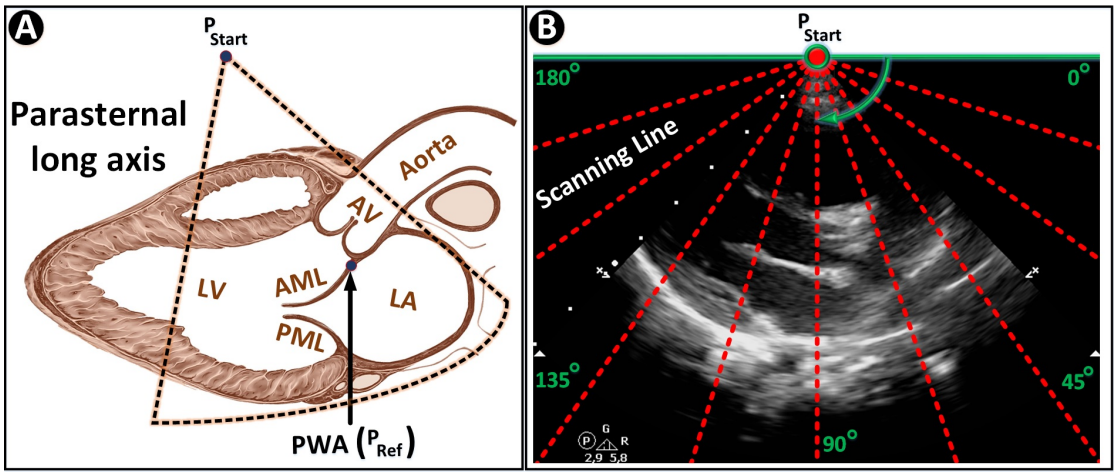

FIGURE 6.11: A) Parasternal long axis (PLAX) view (AML - Anterior Mitral Leaflet, PWA - Posterior Wall of the Aorta, P_{Start}- starting point of the ultrasound); B) PLAX view of the ultrasound image, origin point P_{Start} with respective angles and scanning lines.

This junction point helps to redefine the number of images in the VM-mode space in which the AML was visible. In the fifth step, the AML was segmented in the VM-mode space. Finally, the segmented region of the AML was sampled back to the regular image space and refined using the localized active contours (LAC) [131].

6.3.1 VM-mode Space

The VM-mode space was introduced to efficiently identify the location of the AML in each frame [134]. The VM-mode image shows the position (distance) of structure over time (frames) (see Figure 6.12). In [134], a single scanning line was used over time to sample the whole echocardiographic video. In this work, we are proposing the use of multiple scanning lines to sample the whole image over time (see Figure 6.11B), aiming to reconstruct not only the seed point but the complete region of the AML.

The metadata incorporated in the DICOM file was used to obtain the coordinates (x_1, y_1) of the starting point P_{Start} of the ultrasound beams (see Figure 6.11). The point P_{Start} was used as an origin to obtain a set of scanning lines, by varying the θ from 0° to 180° degrees (6.2).

$$\begin{aligned} x^j_{Line} &= r cos\theta_j + x_1 \\ y^j_{Line} &= r sin\theta_j + y_1 \end{aligned} \quad \begin{cases} \frac{y_1 - 1}{sin\theta_j} \leq r \leq \frac{W - y_1}{sin\theta_j} \\ \frac{x_1 - 1}{cos\theta_j} \leq r \leq \frac{H - x_1}{cos\theta_j} \end{cases} \tag{6.9}$$

where, r is the Euclidean distance from the starting point P_{Start} and was constrained by the horizontal (W) and vertical (H) limits of the image. x_{Line} and y_{Line} are the coordinates of the scanning lines, and j is the number of the scanning line.

For simplicity, the scanning lines are represented in the matrix form $L_{ij} \in \mathbb{R}_{R\times N}$, where R is the length of the scanning lines and N is the total number of scanning lines. Next, all the images are sampled using the matrix L_{ij} over time, to obtain the matrix of sampled lines $SL^f_{ij} \in \mathbb{R}^T_{R\times N}$, where T is the total number of frames. SL^f_{ij} is a representation of the images in the VM-mode space, for each scanning line j (6.10).

$$I_{VMmode} = \left[\begin{array}{cccc} SL^1_{1j} & SL^2_{1j} & \cdots & SL^T_{1jT} \\ SL^1_{2j} & SL^2_{2j} & \cdots & SL^T_{2j} \\ \vdots & \vdots & \ddots & \vdots \\ SL^1_{Rj} & SL^2_{Rj} & \cdots & SL^T_{Rj} \end{array}\right]\Bigg|_{j=1}^{M} \tag{6.10}$$

The first row of Figure 6.12 shows the obtained images for each scanning line j in the VM-mode space, where the X-axis and Y-axis of the images show the frames and the Euclidean distance to the starting point P_{Start}, respectively.

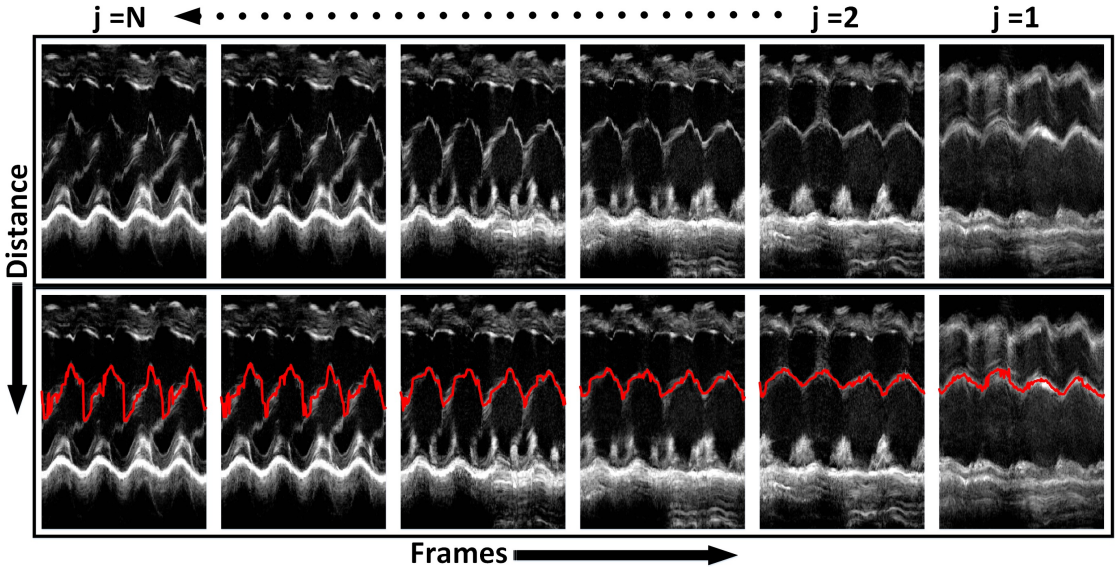

FIGURE 6.12: Row-1: Images in the VM-mode space obtained from the N scanning lines. Row-2: Segmented AML region in the VM-mode space.

6.3.2 Junction Point Estimation

The visual analysis of the AML in the VM-mode space shows that the AML is visible in a small number of images. Therefore, an automatic approach was proposed that defines the number of images in which the AML is visible. This step helps to improve the computational efficiency of the proposed algorithm.

To do so, the vertical motion of the structures in the VM-mode space was analyzed. The mean and standard deviation of the stack of all the images in the VM-mode space was computed (6.11, 6.12), aiming to construct a single image. The constructed image shows the standard deviation of structures from its mean position.

$$\mu = \frac{1}{T}\sum_{f=1}^{T}\left(I_{VMmode}\right) \tag{6.11}$$

$$I_{JNC}\left(i,j\right) = \tfrac{1}{T}\textstyle\sum_{f=1}^{T}\left(I_{VMmode} - \mu\right)\Big|_{j=1}^{M} \tag{6.12}$$

where, μ is the mean, i and j are the depth (distance) and scanning line number, respectively. I_{JNC} was the constructed image (see Figure 6.13A).

The constructed image closely resembles the PLAX view in the systole phase, roughly showing the region of the left atrium (LA), the limits of the motion of the AML and the junction point P_{JNC} of the mitral leaflets (see Figure 6.13A). The manual point P_{REF} was used as a reference to initialize the LAC [131], to segment the region of the LA (see Figure 6.13A). The junction point P_{JNC} is the leftmost point of the segmented LA. A scanning line L_{iK} was obtained by using the junction point P_{JNC} (see Figure 6.13B), where K is the index of the scanning line.

The L_{iK} was used to create two limits, the left side limit (LL) and the right side limit (RL). The limits are computed using the manual annotation by the doctor (62 videos with 5650 frames). The horizontal motion (X-axis) of the tip of the AML from systole to diastole (close to fully open) is analyzed in the manual annotations. The obtained displacement of the AML tip varies from 7.5mm to 23.1mm. To segment the whole AML (especially the tip), the maximum displacement was used as a threshold $T_1 = 23.1mm$ to adjust LL (6.13). The median length of the AML was measured in the manual

annotations and it was used as a threshold $T_2 = 21.6mm$ to adjust the RL. The RL helps to minimize the problem of over segmentation (6.13). After defining the new limits, the images in the VM-mode space that lie within the range ($LL \geq j \leq RL$) are processed (see Figure 6.13B).

$$LL = K + \frac{T_1}{Rez}, \quad RL = K - \frac{T_2}{Rez} \tag{6.13}$$

where, Rez is the spatial resolution of the image.

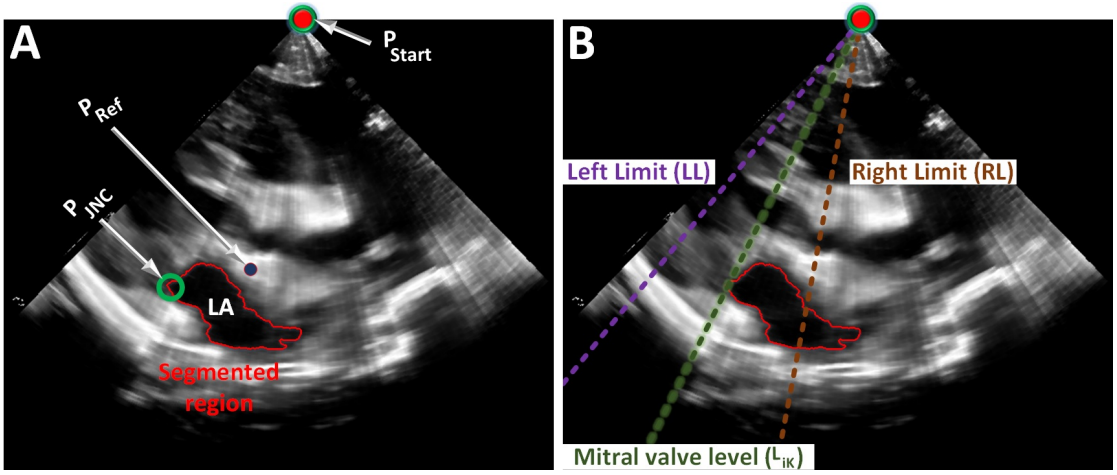

FIGURE 6.13: A) Reconstructed image from the N number of images in the VM-mode space. Showing the left atrium (LA), the reference point (P_{REF}) and the junction point (P_{JNC}). B) Showing the left and right limits with their respective scanning lines.

6.3.3 AML Segmentation in the VM-mode Space

Our previously proposed PWA segmentation framework in the VM-mode image was adapted [134]. The point P_{REF} (see Figure 6.10) was used to extract the respective scanning line L_{iREF} and the image SL^f_{iREF} in the VM-mode space.

The adapted framework comprises an internal energy term and an external energy term. The internal energy imposes a distance constraint. The Euclidean distance was computed from the reference position of the contour point V_{ref} at time $t-1$ to the discrete indexes V_R on the scanning line L_{iREF} at time t. The external energy forces the contour to move vertically on the smoothed sampled line to make locally optimal choice (6.14).

$$\begin{aligned} E_{Total} = & \quad E_{Internal} + E_{External} \\ = & \quad \alpha \left| V_{ref} - V_R \right|_C^2 + \gamma \left| G_\sigma \times SL_{Rj}^f \right|^2 \end{aligned} \tag{6.14}$$

where, the parameter α and γ with values 0.5 and 0.8 respectively, are responsible for controlling the relative importance of both energies, G is the Gaussian smoothing of the sampled line with sigma $\sigma = 2$ and R is the allowed step size.

The segmented AML region in the reference image SL_{iREF}^f in the VM-mode space was translated towards right and left within the defined range (LL to RL), to segment the AML (6.14) in all the images in the VM-mode space (see Figure 6.12 second row).

6.3.4 Refining Using LAC

The segmented AML region was reconstructed back to its original image space by using the matrix of scanning lines L_{ij}, where j varies from LL to RL. The region of the AML was then refined by the LAC [131] to extract the true boundaries of the AML.

6.3.5 Materials

An initiative from the Real Hospital Português, in Recife, Brazil lead to the screening of 1203 children's and pregnant women, looking for cardiac pathologies. All patients were tested regarding the presence of streptococcal infection and short mitral valve videos were recorded. Sixty two of these exams were manually annotated by doctors using the OsiriX software and were used to test the method proposed in this work. The mean duration of the echocardiography videos is 2.9 sec with the mean frame rate of 34 frames/sec. These sixty two videos include a total of 5650 frames with dimensions of 422 × 636 pixels. Depending on the equipment and depth, the spatial resolution ranged was between 0.115mm to 0.384mm. The proposed method was implemented using MATLAB R2016b on a desktop computer (Quad-Core AMD Phenom II processors, 3.2 GHZ, 8 GB RAM) in Windows 10 environment.

6.3.6 Experimental Methodology

The performance of the proposed tracking method was evaluated by computing the Dice Similarity Coefficient (DSC) [139], that actually computes the overlap between two regions. The evaluation matrix consist of two parts. First, accessing the performance of the AML segmentation by comparing the manual annotation (obtained by doctors) to the automatic annotation (obtained by the proposed method) using DSC. Second, allows the comparison to other study, like in this work with our previous contribution (Ref.) [134] to evaluate the degree of improvement.

6.3.7 Segmentation Results

The median DSC score of the proposed algorithm and the Ref. was 0.63 and 0.62, respectively (Table 6.2). Showing that the both algorithms have shown the same degree of similarity against the ground truth.

The precision and recall are used to evaluate the quality of the automatic segmentation against the ground truth. The precision measure of the proposed algorithm and the Ref. was 58% and 60%, respectively. Showing that the Ref. approach was slightly better in avoiding over segmentation than the proposed algorithm (Table 6.2). The over segmentation was the problem of segmenting unwanted regions like the chordae tendineae, posterior mitral leaflet, anterior aorta and cardiac walls. It happens due to no reliable features and similar intensity values between neighbor structures. The recall measure of the proposed algorithm and the Ref. was 73% and 65%, respectively. Showing that the proposed approach was more effective than the Ref. in segmenting most part of the AML and it is relatively better at avoiding the problem of under estimation. The problem of under segmentation happens due to the low quality of the image resulting into discrete visualization of the AML.

TABLE 6.2: Comparison matrix, (Median / STD)

62 videos, 5650 frames	**DSC**	**Precision %**	**Recall %**
Our approach	0.63 / 0.14	58 / 20	73 / 16
Ref. [134]	0.62 / 0.15	60 / 18	65 / 22

6.3.8 Discussion

A new method for the segmentation of the AML in echocardiography was proposed. Results shown that the proposed algorithm is feasible for the segmentation of AML. The proposed algorithm has successfully segmented the AML throughout the VM-mode space, providing a rough estimation of the AML in the original image space for each frame, later refined by the LAC. The proposed algorithm is capable of segmenting the whole leaflet, which was not possible in our previous approach [134] due to availability of only a single seed information and the discrete nature of the AML in ultrasound. However, there is still a limitation of over segmentation in the proposed algorithm resulting into low precision (58%).

The post-processing step with shape constraints can significantly minimize the problem of over and under segmentation and will be the focus in our future work.

Chapter 7

Conclusion

In this thesis, we have reviewed and evaluated the existing state of the art methods in AML segmentation and tracking, in echocardiography. The clinical background was also presented to better understand the disease and its consequences on the heart valves.

To further improve the tracking capabilities of the existing algorithms, we have proposed several modifications in the classical snake model [24]. The open-ended contours with the Harris cornerness energy was used to improve the tracking performance. The algorithm had successfully tracked the AML with the average MHD error of 4.9 pixels and the standard deviation of 2.1 pixels. However, the method was unable to handle the large frame to frame displacement of the AML and was unable to recover from the failure. To address this difficulty, optical flow was integrated in the classical snake model, solving various situations associated with large AML motion. There was no significant difference in the overall performance of both methods, but later showed superior performance in situations when the AML exhibited large motion. The computed average MHD error was 4.5 pixels and the standard deviation was 2 pixels.

We have also proposed a near real-time tracking method using a mathematical morphological operators and an active contours framework. The method showed better tracking performance than previous alternatives with E-MHD error of 3.7 pixels, with less failures and was computationally efficient.

It is very challenging and unclear how we can overcome all these limitations, more specifically the problem of tracking failure and extensive user interaction, simply by using an active contours framework. This challenge motivated us to try a different

approach, coming up with the novel approach of converting the image space into a more adequate space called the VM-mode. In a first work, we have successfully identified the AML throughout the cardiac cycle in the VM-mode space, without any failure and with minimum user interaction (single point). The average MHD error of the proposed method was 2.3 mm, with recall of 0.94. The limitation of this work was the low robustness against the problem of under-segmentation that leads to the missing tip of the AML. The tip of the AML is the key location to identify early variations in thickness due to RHD. Therefore, we extended our previous approach [134] by proposing a two step method: the initial boundary estimation of the whole AML in the VM-mode space, later refined by active contours. The average DSC error was 0.63 with an average precision and recall of 58 % and 73 %, respectively.

It can be concluded from our successive contributions that we have successfully addressed most of the limitations present in the literature. We have significantly minimized the rate of failure, minimized the user interaction, minimized the problem of under segmentation, improved computational efficiency and achieve high robustness. As future work, we are integrating shape constraints (adding principal component analysis model) in the classical snake model to minimize the problem of over segmentation, further improving our ability to robustly segment the AML in echocardiograhic videos.

7.1 Research Collaborations

During this PhD work, we had several successful research collaborations that outcome to scientific contributions. Start with the work that is part of this project "CAD system for the diagnosis of RHD" and is thus more relevant to this thesis. After having the robust and reliable AML segmentation, we focused on the next stage of the CAD system that is to measure, quantify and analyze the morphological features (section 1.2). We had proposed the method to automatically measure, quantify and analyze the thickness of AML and perform the comparative study between normal and pathological cases [1]. The study provides the statistics to better understand when and where to measure the thickness of AML that was previously unavailable. The study reveals that the thickness measurement of AML is most adequate at the tip of the AML and when the valve is open or straight. In other work, we proposed the method to segment the mitral valve regurgitation jet in Doppler echocardiography [2]. The color flow Doppler is a key to

early diagnosis and thus segmenting the regurgitation jets was the first step towards measuring and quantifying the severity of the disease.

Another project aims to develop a CAD system for the early detection of Rheumatoid Arthritis in musculoskeletal ultrasound. I was fully involved in this project during the pilot study and directly contributed to this project with two contributions (provided earlier in this thesis – section 1.6.4). Later, after having the dataset for my project. I had shifted my focus on the segmentation and the tracking of AML for the early diagnosis of RHD. However, i had continued collaborating with another researcher who had resumed the work on the rheumatoid arthritis project. The work focuses on the segmentation of the extensor tendon, joint capsule, metacarpus and phalangeal bones. Followed by the measuring, quantifying, analyzing relevant features and finally the classification [3, 4, 5, 6].

1. L. Pires, **M.S. Sultan**, N. Martins, E. Costa, D. Veiga, M.J. Ferreira, and M.T. Coimbra, "Extracting Thickness Profiles of Anterior Mitral Leaflets in Echocardiography Videos", in Proc. IEEE EMBC, Honolulu, Hawaii, Jul 2018.

2. E. Costa, N. Martins, **M.S. Sultan**, D. Veiga, M. Ferreira, S. Mattos, and M. Coimbra, "A Preliminary Approach for the Segmentation of Mitral Valve Regurgitation Jet in Doppler Ecocardiography Images", in Proc. Int. Joint Conf. on Biomedical Engineering Systems and Technologies, BIOSTEC, Porto, Portugal, Feb 2017, (DOI: 10.5220/0006248900470054)

3. N. Martins, **M.S. Sultan**, D. Veiga, M.J. Ferreira, F. Teixeira, M. Coimbra, "A New Active Contours Approach for Finger Extensor Tendon Segmentation in Ultrasound Images using Prior Knowledge and Phase Symmetry", (early access publication) in IEEE Journal of Biomedical and Health Informatics (DOI: 10.1109/JBHI.2017.2723819)

4. N. Martins, **M.S. Sultan**, D. Veiga, M. Ferreira, Miguel Coimbra, "Fully Automatic Finger Extensor Tendon Segmentation in Ultrasound Images of the Metacarpophalangeal Joint", in Proc. IEEE EMBC, Honolulu, Hawaii, Jul 2018.

5. N. Martins, **M.S. Sultan**, D. Veiga, M. Ferreira, Miguel Coimbra, "Joint Capsule Segmentation in Ultrasound Images of the Metacarpophalangeal Joint using a Split and Merge Approach", in Proc. IEEE BHI, Nevada, USA, March 2018.

6. N. Martins, **M.S. Sultan**, D. Veiga, M.J. Ferreira, and M. Coimbra, "Segmentation of the metacarpus and phalange in musculoskeletal ultrasound images using local active contours", in Proc. IEEE EMBC, Orlando, USA, Aug 2016, (DOI: 10.1109/EMBC.2016.7591627)

Bibliography

[1] S.Y. Tartof. Rheumatic heart disease and beta-hemolytic streptococci in salvador, brazil: A study of slum health. *UC Berkeley Electronic Theses and Dissertations*, 2010.

[2] R. Hajar. Rheumatic fever and rheumatic heart disease a historical perspective. heart views. *The Official Journal of the Gulf Heart Association*, 17(3):120–126, 2016.

[3] B.J. Currie J.R. Carapetis. Mortality due to acute rheumatic fever and rheumatic heart disease in the northern territory: A preventable cause of death in aboriginal people. *Australian and New Zealand Journal of Public Health*, 23:159–163, 1999.

[4] J.R. Carapetis et al. The global burden of group a streptococcal diseases. *Lancet Infectious Diseases*, 5:685–694, 2005.

[5] Global, regional, and national incidence, prevalence, and years lived with disability for 301 acute and chronic diseases and injuries in 188 countries, 1990–2013: A systematic analysis for the global burden of disease study 2013 global burden of disease study 2013 collaborators.

[6] S.M. Colquhoun et al. Rheumatic heart disease and its control in the pacific. *Expert Review of Cardiovascular Therapy*, 7(12):1517–1524, 2009.

[7] R. Lozano et al. Global and regional mortality from 235 causes of death for 20 age groups in 1990 and 2010: A systematic analysis for the global burden of disease study 2010. *Lancet*, 380:2095–2128, 2012.

[8] A. Bisno et al. Expert consultation on rheumatic fever and rheumatic heart disease. *WHO*, 2004.

[9] P. Collier et al. Mitral valve disease: Stenosis and regurgitation. *WHO*, 2014. URL http://www-cs-faculty.stanford.edu/~uno/abcde.html.

[10] B. Remenyi et al. World heart federation criteria for echocardiographic diagnosis of rheumatic heart disease-an evidence-based guideline. *Nature Reviews Cardiology*, 9(5):297–309, 2012.

[11] A.C. Steer et al. High prevalence of rheumatic heart disease by clinical and echocardiographic screening among children in fiji. *Journal of Heart Valve Disease*, 18(3): 327–335, 2009.

[12] E. Marijon et al. Prevalence of rheumatic heart disease detected by echocardiographic screening. *NEJM*, 357:470–476, 2007.

[13] M. Bhaya et al. High prevalence of rheumatic heart disease detected by echocardiography in school children. *Echocardiography*, 27(4):448–453, 2010.

[14] R.H. Webb et al. Optimising echocardiographic screening for rheumatic heart disease in new zealand: Not all valve disease is rheumatic. *Cardiology in the Young*, 21(4):21, 2011.

[15] A. Beaton et al. Echocardiography screening for rheumatic heart disease in ugandan schoolchildren. *Circulation*, 125(25):3127–3132, 2012.

[16] I. Mikic et al. Segmentation and tracking in echocardiographic sequences: Active contours guided by optical flow estimates. *in Proc. IEEE TMI*, 17(2), 1998.

[17] A. Singh. Optic flow computation: A unified perspective. *in Proc. IEEE Computer Society Press*, 1992.

[18] S. Martin et al. Tracking of the Mitral Valve Leaflet in Echocardiography Images. *in Proc. IEEE ISBI*, pages 181–184, 2006.

[19] S. Martin et al. Fast Segmentation of the Mitral Valve Leaflet in Echocardiography. *CVAMIA*, pages 225–235, 2006.

[20] A.B. Pearlmutter. Fast exact multiplication by the hessian. *Neural Computation*, 6(1):147–160, 2006.

[21] A.A. Amini et al. Using dynamic programming for solving variational problems in vision. *in Proc. IEEE TPAMI*, 12(9), 1990.

[22] C. Sheng et al. Segmentation in echocardiographic sequences using shape-based snake model combined with generalized hough transformation. *The International Journal of Cardiovascular Imaging*, 22, 2006.

[23] D.H. Ballard. Generalizing the hough transform to detect arbitrary shapes. *Pattern Recognition*, 13:111–122, 1981.

[24] M. Kass et al. Snakes: Active contour models. *IJCV*, 4(1):321–331, 1988.

[25] X. Zhou et al. Automatic mitral leaflet tracking in echocardiography by outlier detection in the low-rank representation. *in Proc. IEEE CVPR*, 2012.

[26] X. Liu et al. Automatic mitral valve leaflet tracking in echocardiography via constrained outlier pursuit and region-scalable active contours. *Neurocomputing*, 144:47–57, 2014.

[27] R. Mazumder et al. Spectral regularization algorithms for learning large incomplete matrices. *JMLR*, 11:2287–2322, 2010.

[28] Y. Shang et al. Region competition based active contour for medical object extraction. *CMIG*, 32:109–117, 2008.

[29] A. Yuille S.C. Zhu. Region competition: Unifying snakes, region grouping, and bayes/mdl for multiband image segmentation. *in Proc. IEEE TPAMI*, 18(9):884–900, 1996.

[30] V. Caselles et al. Geodesic active contours. *IJCV*, 1(22):61–79, 1997.

[31] L.A. Vese T.F. Chan. Active contours without edges. *in Proc. IEEE TIP*, 2(10): 266–277, 2001.

[32] P. Burlinaa et al. Patient-specific modeling and analysis of the mitral valve using 3d-tee. *Ultrasound in Medicine and Biology*, 39(5):769–783, 2013.

[33] P. Burlina et al. Patient-specific modeling and analysis of the mitral valve using 3d-tee. *IPCAI–LNCS*, pages 135–146, 2010.

[34] A. Huang et al. Thin structure segmentation and visualization in three-dimensional biomedical images: A shape-based approach. *in Proc. IEEE TVCG*, pages 93–102, 2006.

[35] R.J. Schneider et al. Modeling mitral valve leaflets from three-dimensional ultrasound. *LNCS*, pages 215–222, 2011.

[36] R.J. Schneider et al. Mitral annulus segmentation from four-dimensional ultrasound using a valve state predictor and constrained optical flow. *Medical Image Analysis*, 16(2):497–504, 2012.

[37] R.J. Schneider et al. Patient-specific mitral leaflet segmentation from 4d ultrasound. *MICCAI*, 14(3):520–527, 2011.

[38] T. Kanade B. Lucas. An iterative image registration technique with an application to stereo vision. *Proc. International Joint Conference on Artificial Intelligence*, pages 674–679, 1981.

[39] A.M. Pouch et al. Development of a semi-automated method for mitral valve modeling with medial axis representation using 3d ultrasound. *AAPM*, 2012.

[40] A.M. Pouch et al. Medially constrained deformable modeling for segmentation of branching medial structures: Application to aortic valve segmentation and morphometry. *Medical Image Analysis*, 26(1):217–231, 2015.

[41] A.M. Pouch et al. Fully automatic segmentation of the mitral leaflets in 3d transesophageal echocardiographic images using multiatlas joint label fusion and deformable medial modeling. *Medical Image Analysis*, 18:118–129, 2014.

[42] S. Smith M. Jenkinson. A global optimisation method for robust affine registration of brain images. *Medical Image Analysis*, 5:143–156, 2001.

[43] B.B. Avants et al. Symmetric diffeomorphic image registration with cross-correlation: Evaluating automated labeling of elderly and neurodegenerative brain. *Medical Image Analysis*, 12:26–41, 2008.

[44] S.M. Pizer et al. Deformable m-reps for 3d medical image segmentation. *IJCV*, 55:85–106, 2003.

[45] P.A. Yushkevich et al. Continuous medial representation for anatomical structures. *in Proc. IEEE TMI*, 25:1547–1564, 2006.

[46] M. Sotaquira et al. Semi-automated segmentation and quantification of mitral annulus and leaflets from transesophageal 3-d echocardiographic images. *in Proc. IEEE TMI*, 41(1):251–267, 2015.

[47] G.E. Trahey L.N. Bohs. A novel method for angle independent ultrasonic imaging of blood flow and tissue motion. *in Proc. IEEE TBE*, 38:280–286, 1991.

[48] E.W. Dijkstra. A note on two problems in connexion with graphs. *Numerische Mathematik*, 1:269–271, 1959.

[49] Henry Gray. Anatomy of the human body. *Thoroughly Revised and Re-edited by Warren H. Lewis*, 20, 2000.

[50] Mitral valve replacement. . URL https://simple.wikipedia.org/wiki/Heart.

[51] J.G. Betts et al. *Anatomy and Physiology*. 2013. URL https://books.google.pt/books?id=jD00ngEACAAJ.

[52] H. Potter. Anatomy and physiology ii lecture. 2003. URL http://faculty.ucc.edu/biology-potter/biology%20106%20lecture.htm.

[53] . URL https://en.wikipedia.org/wiki/Diastole.

[54] J.H. Lam et al. Morphology of the human mitral valve. i. chordae tendineae: A new classification. *Circulation*, 41:449–458, 1970.

[55] J.A. Ormiston et al. Size and motion of the mitral valve annulus in man. i. a two-dimensional echocardiographic method and findings in normal subjects. *Circulation*, 64:113–120, 1981.

[56] D. Glower M. Fontes. Mitral valve replacement. URL https://www.clinicalpainadvisor.com/anesthesiology/mitral-valve-replacement/article/580652/.

[57] J.D. Bronzino. *The Biomedical Engineering HandBook*. 2000.

[58] https://www.mitralvalverepair.org/leaflets. *last access April 25, 2018*.

[59] R.G. Pai et al. Effect of atrial fibrillation on the dynamics of mitral annular area. *JHVD*, 12(1):31–37, 2003.

[60] G.P. Armstrong. Overview of heart valve disorders. URL https://www.msdmanuals.com/home/heart-and-blood-vessel-disorders/heart-valve-disorders/overview-of-heart-valve-disorders.

[61] R.H. Webb et al. Acute rheumatic fever. *BMJ*, 351:3443, 2016.

[62] BM. Mayosi J. Manyemba. Intramuscular penicillin is more effective than oral penicillin in secondary prevention of rheumatic fever – a systematic review. *SAMJ*, 93(3):212–218, 2003.

[63] Rheumatic heart disease. URL https://medical-dictionary.thefreedictionary.com/rheumatic+heart+disease.

[64] A. Beaton J.R. Carapetis. Acute rheumatic fever and rheumatic heart disease. *Nature Reviews — Disease Primers*, (15084), 2016.

[65] D.A. Watkins et al. Global, regional, and national burden of rheumatic heart disease, 1990-2015. *NEJM*, 377(8):1990–2015, 2017.

[66] J.R. Carapetis M. Tubridy-Clark. Subclinical carditis in rheumatic fever: A systematic review. *International Journal of Cardiology*, 119:54–58, 2007.

[67] F.E. Figueroa et al. Prospective comparison of clinical and echocardiographic diagnosis of rheumatic carditis: Long term follow up of patients with subclinical disease. *Heart*, 85:407–410, 2001.

[68] J.R. Carapetis et al. The global burden of group a streptococcal diseases. *Lancet Infectious Diseases*, 5:685–694, 2005.

[69] S.C. Smith et al. Our time: A call to save preventable death from cardiovascular disease (heart disease and stroke). *Circulation*, 126:2769–2775, 2012.

[70] J. Ralston. New global target on non-communicable diseases: A call to action for the global cardiovascular disease community. *Cardiovascular Journal of Africa*, 23:241–242, 2012.

[71] G. Gunther et al. Death from rheumatic heart disease in rural areas. *Lancet*, 367 (9508):391, 2006.

[72] T. Jones E. Bland. Rheumatic fever and rheumatic heart disease. a twenty-year report on 1,000 patients followed since childhood. *Circulation*, 4:836–843, 1951.

[73] A. Chockalingam et al. Clinical spectrum of chronic rheumatic heart disease in india. *Journal of Heart Valve Disease*, 12(5):577–581, 2003.

[74] R.H. Marcus et al. The spectrum of severe rheumatic mitral valve disease in a developing country. correlations among clinical presentation, surgical pathologic

findings, and hemodynamic sequelae. *Annals of Internal Medicine*, 120(3):177–183, 1994.

[75] C. Yankah et al. Rheumatic mitral valve repair: 22-year clinical results. *Journal of Heart Valve Disease*, 20:257–264, 2011.

[76] J. Hewitson et al. The challenge of pediatric cardiac services in the developing world. *Seminars in Thoracic and Cardiovascular Surgery*, 14:340–345, 2002.

[77] M. Mirabel et al. Screening for rheumatic heart disease: Evaluation of a focused cardiac ultrasound approach. *Circulation: Cardiovascular Imaging*, 8(1), 2015.

[78] D.A. North et al. Analysis of costs of acute rheumatic fever and rheumatic heart disease in auckland. *New Zealand Medical Journal*, 106(964):400–403, 1993.

[79] R.J. Milne et al. A scuffham mortality and hospitalisation costs of rheumatic fever and rheumatic heart disease in new zealand. *Journal of paediatrics and child health*, 2012.

[80] B. Falase et al. The cost of open heart surgery in nigeria. *PAMJ*, 14(61), 2013.

[81] F. Bode-Thomas et al. Childhood acquired heart diseases in jos, north central nigeria. *Nigerian Medical Journal*, 54(1):51–58, 2013.

[82] F. Jaiyesimi. Acquired heart disease in nigerian children: An illustration of the influence of socioeconomic factors on disease pattern. *Journal of Tropical Pediatrics*, 28:223–229, 1982.

[83] M.U. Sani et al. Prevalence and pattern of rheumatic heart disease in the nigerian savannah: An echocardiographic study. *CVJA*, 2007.

[84] G. Cramp et al. Undetected rheumatic heart disease revealed using portable echocardiography in a population of school students in tairawhiti, new zealand. *New Zealand Medical Journal*, 125:53–64, 2012.

[85] E. Marijon et al. Time to use ultrasound and not stethoscopes for rheumatic heart disease screening. *Nature Clinical Practice. Cardiovascular Medicine*, 5:E1–3, 2008.

[86] L. Zuhlke et al. Congenital heart disease and rheumatic heart disease in africa: Recent advances and current priorities. *Heart*, 2013.

[87] B. Remenyi et al. World heart federation criteria for echocardiographic diagnosis of rheumatic heart disease—an evidence-based guideline. *Nature Reviews Cardiology*, 9(5):297–309, 2012.

[88] B.M. Mayosi L. Zuhlke. Echocardiographic screening for subclinical rheumatic heart disease remains a research tool pending studies of impact on prognosis. *Current Cardiology Reports*, 15(343), 2013.

[89] A.S. Omran et al. Echocardiography of the mitral valve. *Journal of the Saudi heart association*, 22(3):165–170, 2010.

[90] T. Mcinerney et al. Deformable models in medical image analysis: A survey. *Medical Image Analysis*, (1):91–108, 1996.

[91] B.V. Ginneken et al. Active shape model segmentation with optimal features. *In Proc. IEEE TMI*, 8(21):924–933, 2002.

[92] S.C. Mitchell et al. Multistage hybrid active appearance model matching: Segmentation of left and right ventricles in cardiac mr images. *In Proc. IEEE TMI*, 5(20):415–423, 2001.

[93] S. Masood et al. A survey on medical image segmentation. *Current Medical Imaging Reviews*, 1(11), 2015.

[94] L.D. Cohen. On active contour models and balloons. *CVGIP: Image Understanding*, 2(53):211–218, 1991.

[95] J.L. Prince X. Chenyang. Gradient vector flow: A new external force for snakes. *in Proc. IEEE CVPR*, pages 66–71, 1997.

[96] J.A. Sethian S. Osher. Fronts propagating with curvature-dependent speed: Algorithms based on hamilton-jacobi formulations. *Journal of Computational Physics*, 1(79):12–49, 1988.

[97] V. Caselles et al. A geometric model for active contours in image processing. *Numerische Mathematik*, 1(66):1–31, 1993.

[98] R. Malladi et al. Shape modeling with front propagation: A level set approach. *in Proc. IEEE TPAMI*, (17):158–175, 1995.

[99] M.A. Grayson. Shortening embedded curves. *Annals of Mathematics*, pages 71–111, 1989.

[100] L. Chunming et al. Distance regularized level set evolution and its application to image segmentation. *in Proc. IEEE TIP*, 12(19):3243–3254, 2010.

[101] S. Lankton et al. Hybrid geodesic region-based curve evolutions for image segmentation. *Proc. of SPIE*, 6510:266–277, 2007.

[102] S.L. Bridal et al. Milestones on the road to higher resolution, quantitative, and functional ultrasonic imaging. *Proceedings of the IEEE*, 91(10):1543–1561, 2003.

[103] A.F. Frangi et al. Three-dimensional modeling for functional analysis of cardiac images: A review. *in Proc. IEEE TMI*, 20(1):2–25, 2001.

[104] A. Mishra et al. A ga based approach for boundary detection of left ventricle with echocardiographic image sequences. *Image and Vision Computing*, 21:967–976, 2003.

[105] M. Mignotte et al. A multiscale optimization approach for the dynamic contour-based boundary detection issue. *Computerized Medical Imaging and Graphics*, 25 (3):265–275, 2001.

[106] F. Heitz et al. Multiscale minimization of global energy functions in some visual recovery problems. *CVGIP: Image Understanding*, 59(1):125–134, 1994.

[107] A. Skalski et al. Left ventricle usg image segmentation using active contour model. *ICCS*, 2010.

[108] P. Turcza A. Skalski. Heart segmentation in echo images. *Metrology and Measurement Systems*, XVIII(2):305–314, 2011.

[109] T. Dietenbeck et al. Detection of the whole myocardium in 2d-echocardiography for multiple orientations using a geometrically constrained levelset. *Medical Image Analysis*, 16:386–401, 2012.

[110] R. Juang et al. Automatic segmentation of the leftventricular cavity and atrium in 3d ultrasound using graph cuts and the radial symmetry transform. *in Proc. IEEE ISBI: From Nano to Macro*, pages 606–609, 2011.

[111] M.S. Sultan et al. Tracking of the anterior mitral leaflet in echocardiographic sequences using active contours. *in Proc. IEEE EMBC*, 2016.

[112] M.S. Sultan et al. Tracking large anterior mitral leaflet displacements by incorporating optical flow in an active contours framework. *in Proc. IEEE EMBC*, 2017.

[113] M. Abramowitz M.W. Davidson. Molecular expressions microscopy primer: Digital image processing – difference of gaussians edge enhancement algorithm. *Olympus America Inc., and Florida State University.*

[114] A. Rosenfeld L. Kitchen. Gray-level corner detection. *Pattern Recognition Letters*, 1:95–102, 1982.

[115] G. Giraudon R. Deriche. Intramuscular penicillin is more effective than oral penicillin in secondary prevention of rheumatic fever – a systematic review. *International Journal of Computer Vision*, 10(2):101–124, 1993.

[116] P.R. Beaudet. Rational invariant image operators. *ICPR*, pages 579–583, 1978.

[117] H.P. Moravec. Towards automatic visual obstacle avoidance. *IJCAI*, page 584, 1977.

[118] M. Stephens C. Harris. A combined corner and edge detector. *Alvey Vision Conference*, 1988.

[119] A.K. Jain M.P. Dubuisson. A modified hausdorff distance for object matching. *ICPR*, pages 566–568, 1994.

[120] T. Kanade B. Lucas. An iterative image registration technique with an application to stereo vision. *IJCAI*, pages 674–679, 1981.

[121] B.D. Lucas. Generalized image matching by the method of differences. *PhD Thesis, School of Computer Science, Carnegie–Mellon University, Pittsburgh, PA.*, 1984.

[122] B. Schunck B. Horn. Determining optical flow. *Artificial Intelligence*, 17:185–203, 1981.

[123] J.L. Barron et al. Systems and experiment performance of optical flow techniques. *IJCV*, 12(1):43–77, 1994.

[124] R. Brad N. Sharmin. Optimal filter estimation for lucas-kanade optical flow. *Sensors*, 12(9):12694–12709, 2012.

[125] M.S. Sultan et al. Real-time anterior mitral leaflet tracking using morphological operators and active contours. *in Proc. BIOSTEC*, 2017.

[126] M.S. Sultan et al. Tracking anterior mitral leaflet in echocardiographic videos using morphological operators and active contours. *Chap. 10, Biomedical Engineering Systems and Technologies, CCIS - Springer*, 2018.

[127] L. Yun gang et al. Myocardial iron loading assessment by automatic left ventricle segmentation with morphological operations and geodesic active contour on t2* images. *Scientific Reports*, 2015.

[128] D. Lascu M. Lascu. A new morphological image segmentation with application in 3d echographic images. *Transactions on Electronics*, 5(3), 2010.

[129] N. Otsu. A threshold selection method from gray-level histograms. *IEEE Transactions on Systems, Man, and Cybernetics*, 9(1):62–66, 1979.

[130] D. Boukerroui J.A. Noble. Ultrasound image segmentation: A survey. *in Proc. IEEE TMI*, 25(8), 2006.

[131] A. Tannenbaum S. Lankton. Localizing region-based active contours. *in Proc. IEEE TIP*, 17(11):2029–2039, 2008.

[132] C.Y. Suen T.Y. Zhang. A fast parallel algorithm for thinning digital patterns. *Communications of the ACM*, 27(3):236–239, 1984.

[133] H.R. Pourreza A.S. Masoud. A novel curvature-based algorithm for automatic grading of retinal blood vessel tortuosity. *in Proc. IEEE JBHI*, 20(2), 2016.

[134] M.S. Sultan et al. Virtual m-mode for echocardiography: A new approach for the segmentation of the anterior mitral leaflet. *in Proc. IEEE JBHI*, 2018.

[135] M.S. Sultan et al. A new method for the anterior mitral leaflet segmentation in echocardiography videos using the virtual m-mode space. *in Proc. IEEE EMBC*, 2018.

[136] H. Feigenbaum. Role of m-mode technique in today's echocardiography. *Journal of the American Society of Echocardiography*, 23(3):240–257, 2010.

[137] L.P. Badano R.M. Lang. Guidelines and standards: Recommendations for cardiac chamber quantification by echocardiography in adults: An update from the american society of echocardiography and the european association of cardiovascular imaging. *Journal of the American Society of Echocardiography*, 28(1), 2015.

[138] O. Ben-Shahar M. Shemesh. Free boundary conditions active contours with applications for vision. *ISVC: Advances in Visual Computing*, 6938:180–191, 2011.

[139] L.R. Dice. Measures of the amount of ecologic association between species. *Ecology*, 26(3):297–302, 1945.